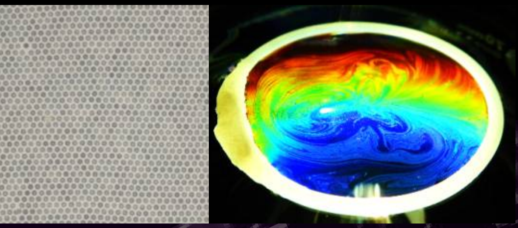

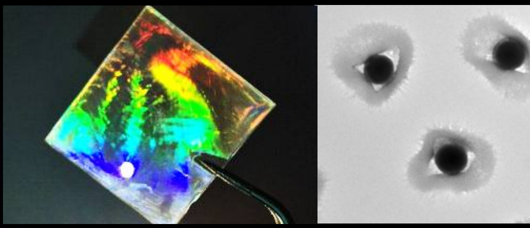

Hard Core-Soft Shell Microgels at Interfaces

Institut für Physikalische Chemie I, Heinrich-Heine-Universität Düsseldorf
Keumkyung Kuk

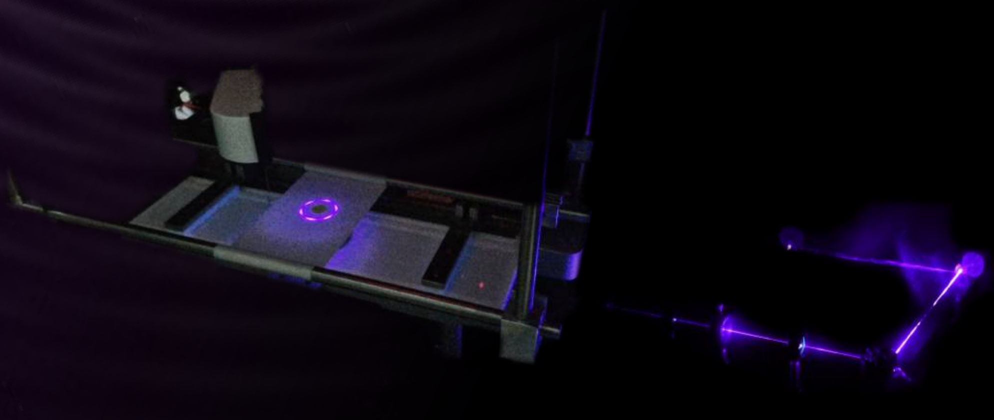

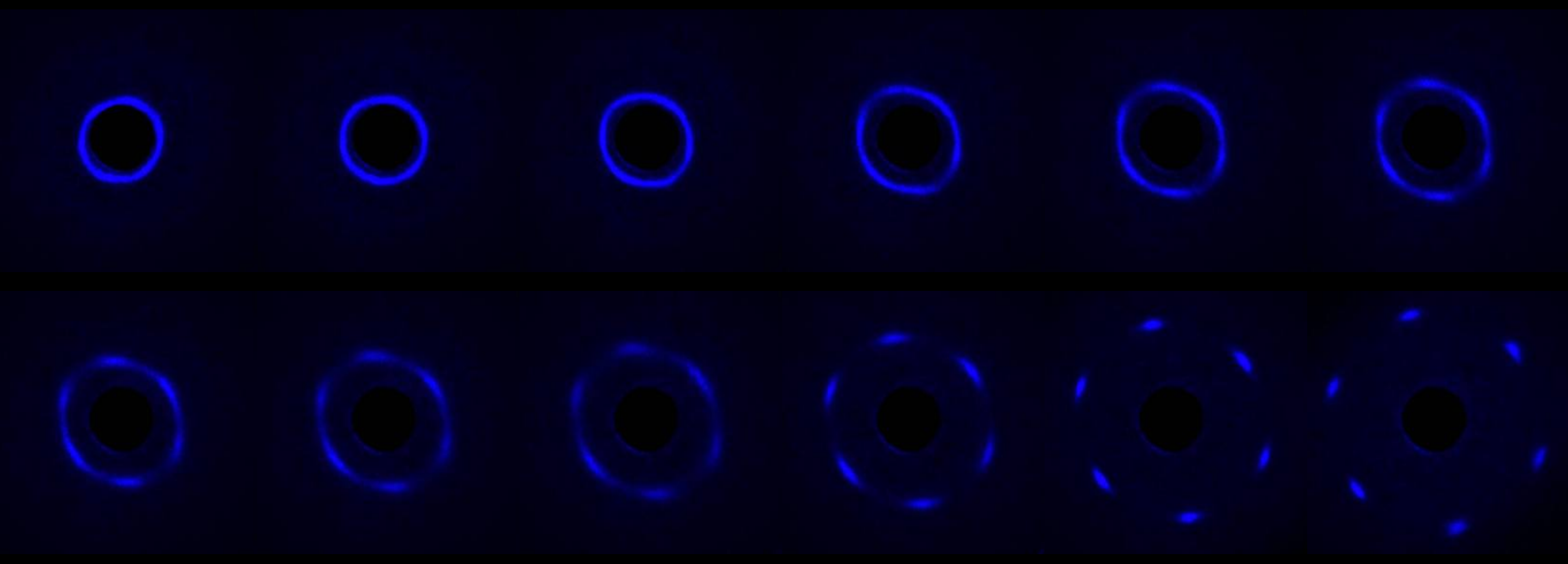

Hard Core-Soft Shell Microgels at Interfaces

Keumkyung Kuk
국금경

Institut für Physikalische Chemie
Heinrich-Heine-Universität Düsseldorf

This dissertation is submitted for the degree of
Doctor of Natural Sciences

December 2023

Cover by Keumkyung Kuk

Institute of Physical Chemistry I: Colloids and Nanooptics
Department of Chemistry
Heinrich Heine University Düsseldorf

Defence date:

Thesis Supervisor: Prof. Dr. Matthias Karg
Second Supervisor: Jun.-Prof. Dr. Ivo Buttinoni

ISBN

Printed in Germany by Uni-Kopiercenter-Duesseldorf

사랑하는 우리 엄마, 아빠 그리고 하나뿐인 내 동생 은경이에게 이 논문을 바칩니다.

To my loving parents, my sister,
and to Dory, my best friend and my wife,

without whom I might not have come this far, and to whom I am forever indebted.

Declaration

I hereby declare under oath that I have produced my thesis independently and without any undue assistance by third parties under consideration of the ‘Principles for the Safeguarding of Good Scientific Practice at Heinrich Heine University Düsseldorf’ and that this work has not been submitted for any other degree or professional qualification. This dissertation is my own work and contains nothing which is the outcome of work done in collaboration with others, except where work which has formed part of jointly-authored publications has been included. My contribution and those of the other authors to this work have been explicitly indicated in the Acknowledgements as well as in the List of Publications. I confirm that appropriate credit has been given within this thesis where reference has been made to the work of others.

Kuk

Keumkyung Kuk
국금경
December 2023

Acknowledgements

It is with gratitude that I express my appreciation to my two cherished friends, Jessica González and Michael Kuhn, and to my adorable feline friends, Fely and Kyomi, whose support has been indispensable in achieving my goals in Germany. Their presence in my life has been my strength and motivation, especially during the unprecedented times of the COVID-19 pandemic. **Danke dass ihr immer für mich da seid!**

I am deeply grateful for the support from my supervisor, Prof. Matthias Karg. His trust in my dedication and ability has been invaluable throughout my research journey. I must also extend a heartfelt thanks to my beloved working partner, Vahan Abgarjan, whose assistance has been essential to numerous projects. Without his presence, this work would have undoubtedly taken much longer. I would be remiss not to acknowledge my mentor, Jun.-Prof. Ivo Buttinoni, who has been a constant source of inspiration, not only for our joint projects but also for shaping my future career since the beginning of my study. I also would like to express my deepest gratitude to Dr. Virginia Carrasco Fadanelli, who has been there for me through scientific and personal difficulties during our time at the university.

Furthermore, I would like to thank those who have participated in small and large-scale collaborative projects, enriching my knowledge and understanding of their respective research domains: Dr. Sebastian Hänsch (HHU) for the introduction to confocal laser scanning microscopy and fruitful imaging sessions, Dr. Debasish Saha (HHU) for the optical tweezer experiments, Marius Otten (HHU) for transmission electron microscopy, Yichu Zhou (HHU) and Jonathan Garthe (HHU) for some of the Langmuir-Blodgett experiments and atomic force microscopy, Sude Alici (HHU) for sharing her interfacial rheology results, Johannes Harrer (FAU) and Maret Ickler (FAU) for the insight into the hairy particle synthesis and the interesting discussions aiming future joint studies, Dr. Steffen Bochenek (RWTH) for interfacial shear rheology experiments and the nice Korean lunch in Aachen, Alexander Petrunin (RWTH) for the static light scattering measurements, Timon Kratzenberg (RWTH) for the radial trough experiments and his visit to Düsseldorf, Kevin Gräff (TUD) and Prof. Regine von Klitzing (TUD) for the thin film pressure balance experiments and the delightful hosting in Darmstadt, and Dr. Andrey Rudov (DWI) and Prof. Igor Potemkin (DWI) for interesting discussions and fascinating simulation results.

I also would like to acknowledge my colleagues who proofread the theoretical parts of this thesis: Vahan Abgarjan, Julian Ringling, and Marcel Krüsmann, and the students who have contributed to my project and helped me to deepen my knowledge in the related fields: Lukas Gregel, Felix Wieser, Jordi Borsdorf, Gérard Peeters, Tillmann Wigger, Julian Ringling, Jan Heise, and Julian Kippenberger. Many thanks to the head of the Fine Mechanics department, Ms. Sonja Schiller, and Mr. Corell Spöringer who have realised many of our self-designed setups, and the members of our group: Andrea Lotzwick, Philipp Hammers, Déborah Feller, Marco Hildebrandt.

Lastly, I would like to thank Dr. Marcel Rey for the encouragement in pursuing my future academic career, and my former engineering colleague and a good friend, Mike Burrows for proofreading all my theses written in English.

Abstract

Poly(N-isopropylacrylamide) or PNIPAM microgels, are now well-known due to their stimuli-responsive nature, which has offered exciting opportunities to tune interactions, packing fractions, and drug release on demand. Such microgels—soft and deformable crosslinked polymer networks—have demonstrated their suitability as a model system, a highly tailorable soft counterpart of the already established hard sphere model systems. They are also readily adsorbed at fluid/liquid interfaces and have been shown to effectively stabilise emulsions and foams. Unlike hard spheres or similar systems, however, microgels exhibit elastic deformation at the interface in response to interfacial tension, resulting in complex morphologies with combined properties of the polymer, colloid, and solvent. This thesis focuses on interactions among such microgels at fluid/liquid interfaces. It encompasses the synthesis and fluid interface-assisted assembly of these microgels, as well as their interaction with various solid surfaces during the deposition onto substrates.

Micron-sized silica-PNIPAM core-shell (CS) microgels were synthesised as model systems using seeded precipitation polymerisation. The proposed batch synthesis protocol allows control over the shell-to-core size ratio in a wide range of dimensions. These core-shell microgels are specifically designed to have high optical contrast as well as a suitable interparticle distance for small-angle light scattering and various microscopic techniques, enabling *in situ* monitoring of the interfacial behaviour of such microgels in both reciprocal and real spaces. Through our model systems, we aim to bridge the research gap stemming from the difficulty of visualizing at the individual microgel level.

The synthesised CS microgels with various dimensions were assembled at the air/water interface using the Langmuir trough combined with the small-angle light scattering setup (LT-SALS). The assembly behaviour of the microgels was also investigated by means of microscopy. The *in situ* measurement results from the reciprocal and real spaces were compared. The comparison between these two complementary methods showed a strong agreement. However, when compared with *ex situ* results—after the deposition onto a solid substrate—we found significant differences in the microstructure of the microgels.

Video microscopy of drying microgel films (soft colloidal monolayer) on different substrates unveiled a complex drying scenario influenced by the wettability of the substrate,

the elasticity of individual microgels, and the surface pressure of the microgel-laden interface. By considering CS microgels with three different crosslinker densities, we identified two key elements, which govern the drying process of such microgel films on a substrate: the microgel-to-substrate adhesion and the immersion capillary force. Our argument finds support in various complementary measurements, including thin film pressure balance, film thickness analysis coupled with particle tracking, as well as molecular dynamics simulations. In future work, we hope that our results can facilitate the development of a more comprehensive theoretical framework for elucidating the interfacial behaviour of soft matter.

List of Publications

1. **Kuk, K.**, Gregel, L., Abgarjan, V., Croonenbrock, C., Hänsch, S., & Karg, M. (2022). Micron-sized silica-PNIPAM core-shell microgels with tunable shell-to-core ratio. Gels, 8(8), 516.

   The conceptualisation was outlined and accompanied by M.K. Synthetic studies were performed by K.K. and L.G. TEM images were recorded by C.C. Confocal microscopy was performed by S.H. under the guidance of K.K. The SALS setup was built by V.A. and modified by K.K. SALS measurements were performed by K.K. Writing of the original draft was done by K.K. and review and editing by all coauthors. Project administration and funding acquisition was done by M.K.

2. **Kuk, K.**, Abgarjan, V., Gregel, L., Zhou, Y., Carrasco-Fadanelli, V., Buttinoni, I., & Karg, M. (2023). Compression of colloidal monolayers at liquid interfaces: in situ vs. ex situ investigation. Soft Matter, 19(2), 175-188.
   Highlighted papers of 2022 – selected by the Soft Matter Editorial Board

   Syntheses were done by K.K., L.G., V.A., Y.Z., and a former member of the group, Dr. Kiran Jathavedan. The idea of in situ SALS analysis of monolayer under compression was conceived by K.K. and accompanied by M.K. The setup was designed by K.K. under the guidance of V.A. Components were manufactured by the department of Fine Mechanics. Alignment/calibration of the SALS setup and calculation protocol were done and set by V.A. Ex situ analysis of the core-shell monolayer by light microscopy was done by K.K. and that of microgel and silica monolayers were done by V.A. AFM imaging was done by Y.Z. In situ analysis of the monolayer by fluorescence microscopy was done by K.K. and V.CF. In situ diffraction analysis of core-shell microgel monolayer was done by K.K. and that of microgel and silica monolayers were done by V.A. Writing of the original draft was done by K.K. and V.A., edited by M.K. and I.B., and reviewed by all coauthors. M.K. and I.B. supervised the work.

3. **Kuk, K.**, Ringling, J., Gräff, K., Hänsch, S., Carrasco-Fadanelli, V., Rudov, A.A., Potemkin, I.I., von Klitzing, R., Buttinoni, I., & Karg, M. "Drying of soft colloidal film."

   Manuscript in preparation for submission

The idea of in situ monolayer drying observation was conceived by K.K. Syntheses were done by K.K. and J.R. The drying of the monolayers was recorded by J.R. as a part of his Master's project, which was supervised by K.K. The idea of conducting the thin film pressure balance measurement was conceived by M.K. and R.K., realised by K.G. and K.K. Confocal microscopy was performed by S.H. and K.K. Interparticle distance measurements were done by K.K. Colour analysis of microgel monolayer thin film that provides height information was performed by K.G. Particle tracking was done by V.CF, I.B. and K.K. The simulations were done by A.A.R., supervised by I.I.P. Summary of the data, figures, and writing of the original draft was done by K.K., edited by M.K., I.B., R.K., and I.I.P. and reviewed by all coauthors. M.K. and I.B. supervised the work.

4. Abgarjan, V., **Kuk, K.**, Garthe, J.L.S., Wigger, T.L., & Karg, M. "Influence of uniaxial compression on soft colloidal monolayers at the air/water interface."

   Manuscript in preparation for submission

5. **Kuk, K.**, Abgarjan, V., & Karg, M.. "Structural evolution of microgel monolayer confined at air/water interface under uniaxial compression."

   Manuscript in preparation for submission

List of Conference Contributions

1. 35th European Colloid & Interface Society Conference, Athens, Greece (Online)
   5-10 September 2021
   Poster contribution

2. Bayreuth Polymer Symposium 2021 (online)
   20 September 2021
   Attendance

3. 3rd International Summer School on Microgels, Monschau, Germany
   19-22 September 2022
   Poster contribution

4. 51st Conference of the German Colloid Society, Berlin, Germany
   28-30 September 2022
   Poster contribution

5. Particle-Based Materials Symposium 2022, Erlangen, Germany
   6-7 October 2022
   Oral contribution
6. 37th European Colloid & Interface Society Conference, Naples, Italy
   3-8 September 2023
   Oral contribution

List of Student Projects

1. Master's thesis, Lukas Gregel, "2D-Assembly Behaviour of Hard Core-Soft Shell Type Particles under Compression: Effect of Overall Particle Size" 2021
2. Master's thesis, Felix Wieser, "Core-shell microgels at water-air interfaces: Influence of the functionalization of the silica-core", 2021
3. Bachelor's thesis, Jordi Borsdorf, "Präparation und Charakterisierung von 3D kolloidalen Kristallen mithilfe der Kleinwinkellichtstreuung", 2021
4. Bachelor's thesis, Gérard Peeters, "Analyse von kolloidalen Dispersionen mit Rheo-SALS", 2022
5. Master's thesis, Julian Ringling, "In-Situ Monitoring of Micron-Sized Silica-Core PNIPAM-Shell Microgels During Monolayer Drying", 2022
6. Co-supervision of Bachelor's thesis, Jan Schmidt, "Synthese und Photostabilität von fluoreszenzmarkierten Silika-Nanopartikeln", 2022
7. Co-supervision of image analysis project, Tillmann Wigger, "Radial and Azimuthal averaging with MATLAB for small-angle light scattering", 2022
8. Supervision of student assistance, Jan Heise, "Strategies to increase the monodispersity of a microgel system", 2023
9. Supervision of student assistance, Julian Kippenberger, "Self-made Langmuir trough for light microscopy: Minitrough", 2023

Table of contents

List of Abbreviations

Roman Symbols

D_h	hydrodynamic diameter
k_B	Boltzmann’s constant
k_D	Debye screening wave vector
C	concentration
D	diameter
d	distance
E	energy
f	frequency
H	Hamaker constant
k	spring constant
n	refractive index
$P(q)$	form factor
$\overrightarrow{q}$	scattering vector
R	radius
S	entropy
$S(q)$	structure factor
T	temperature

V	volume

Other Symbols

η	dynamic viscosity
γ	interfacial tension
λ	wavelength
λ_D	Debye length
Φ	volume fraction
Π	surface pressure
σ	surface charge density
θ	scattering angle
ε	permittivity

Acronyms / Abbreviations

2D	two dimensions
3D	three dimensions
AFM	atomic force microscopy
APD	avalanche photodiode
BIS	*N*,*N*'-methylenebisacrylamide
CLSM	confocal laser scanning microscopy
CS	core-shell
DLS	dynamic light scattering
DLVO	Derjaguin-Landau-Verwey-Overbeek
FFT	fast Fourier transform
HCSS	hard core-soft shell
LCST	lower critical solution temperature

LT-SALS	Langmuir trough combined with small-angle light scattering
PMMA	polymethyl methacrylate
PMT	photon multiplier tube
PNIPAM	poly(*N*-isopropylacrylamide)
SALS	small-angle light scattering
SEM	scanning electron microscopy
SLS	static light scattering
TEM	transmission electron microscopy
TFPB	thin film pressure balance
TSC	total solid content
VPTT	volume phase transition temperature
VPT	volume phase transition

Chapter 1

Introduction

1.1 Why the hard core-soft shell microgels?

> "There are no such things as quasicrystals, there are only quasi-scientists."
> Nobel laureate Linus Pauling (1901 - 1994)

The formation of natural crystals, such as minerals and gemstone opals, has fascinated mankind long before recorded history. The history of classical crystallography began with J. Kepler in 1611, who discussed for the first time that crystal shapes and internal structures resulted from, in modern terminology, the order of atomic units. [1, 2] In 1984, a new term "quasicrystal" was coined by P. Steinhardt and D. Levine to describe the discovery of D. Shechtman, [3, 4] a single crystal with an icosahedral symmetry in an aluminium alloy—a long forbidden symmetry in classical crystallography—as stereographically illustrated in Figure 1.1. The discovery led to the re-examination and expansion of the conventional definition of crystal. Today, the term crystal is defined as "any material which exhibits essentially a sharp diffraction pattern". [2] Less than two decades ago, yet another concept "soft quasicrystal" was introduced in the field by V. Percec. [5] Since then, a number of materials such as liquid quasicrystals, self-assembled colloids, macromolecules, and block-copolymers, have joined the family. [6–8]

In 1998, E.A. Jagla demonstrated, via numerical simulations, that hard core-soft shell (HCSS) type particles with purely repulsive pair-potentials can be compressed into intriguing quasicrystals with various symmetries in two dimensions (2D, i.e., disks). [9, 10] Formation of such symmetries can occur upon concentration (i.e., an increase in particle number density per unit area) when the energy difference between partially and fully overlapped shells is small enough to allow energy minimisation through shell overlapping in specific directions, albeit at the expense of adjacent shells. This results in the creation of anisotropic

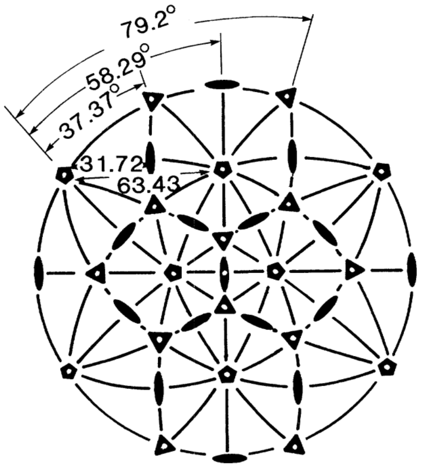

Fig. 1.1 Stereographic projection of the icosahedral symmetry. Adapted with permission from [3]. Copyright (1984) American Physical Society.

building blocks from isotropic HCSS particles, which are essential for the aforementioned symmetries. Among other factors, the ratio between the hard core and the overall soft shell dimensions (i.e., the shell-to-core size ratio) and the interaction potential between two particles govern the symmetries observed at various concentrations. [11–13] These discoveries have initiated a range of engrossing interdisciplinary research among fields of soft colloid physics, mathematics, physical and colloidal chemistry, material science, engineering, etc. [14–18] The self-assembled colloids can be structurally as complex as their atomic counterparts, and besides the fascinating structures and resulting properties [19, 20], they are interesting for various other reasons [20–22]: **1)** They have shown us 18-fold diffraction pattern [7] previously unknown in any intermetallic system, which led to the advent of new point and space groups thus further developing the pre-existing symmetry and group theory. **2)** They are known to present a quite different mechanism compared to their atomic counterpart and are stable under certain conditions, promoting a theoretical understanding of the soft matter assembly. **3)** Their larger sizes facilitate the studying of crystallisation kinetics and search for unifying principles that may govern the (quasi)crystal formation of any scale, not to mention their tailorable size, [23] composition, [24] structure, [25, 26] and morphologies [27] enabling the tuning of interparticle potential.

In this thesis, I take a deeper look into the mesmerising colloidal assembly behaviour at various interfaces (2D) using inorganic hard core-polymeric soft shell type model systems, as illustrated in Figure 1.2A—silica core-poly(*N*-isopropylacrylamide) (PNIPAM) shell microgels. The interaction potentials between these microgels can be varied by engineering the morphology of the polymeric shell, as schematically depicted by the red dashed line. Such microgels can thus potentially be assembled into anisotropic building blocks (in contrast to the isotropic ones shown in Figure 1.2B), as depicted in Figure 1.2C.

Despite their complex internal structures, [28] HCSS microgels offer valuable experimental advantages as soft colloidal model systems, [29, 30] such as high optical contrast due to the existence of the core, engineerability of the structure (e.g., the shell-to-core size ratio), and access to length scales that have not yet been explored. Additionally, the physical properties of the assembled 2D structures can be modified by replacing the core material (e.g., gold-plasmonic). In this work, silica was chosen as the core material as it can be easily synthesised via the well-established Stöber process, [31, 32] with facile control over its overall and pore size, [33] and surface chemistry via silanization. [34] PNIPAM was chosen as the shell material for it is one of the well-studied polymers, [35] which has fascinating properties as will be discussed in section 2.1 in detail. The scope of this study covers a broad range of topics, starting from the synthesis of such microgel systems to their characterisation as individual building blocks as well as that of the assembled microstructures at the interfaces.

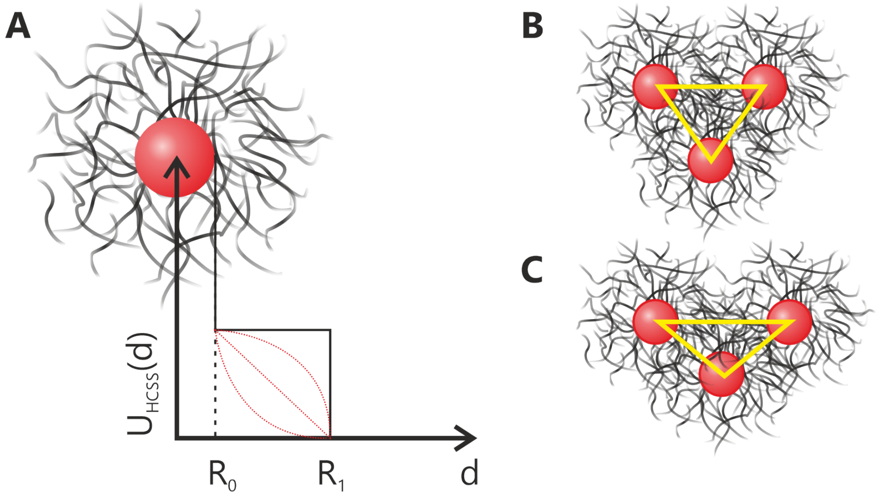

Fig. 1.2 **A**) Schematic representation of an HCSS microgel with the soft interaction potential U_{HCSS} as a function of distance, d. R_0 denotes the radius of the hard core and R_1 the radius of the overall microgel. **B**) Three HCSS microgels assembled into an equilateral triangle, an isotropic building block and **C**) an isosceles triangle, an anisotropic building block.

1.2 Interface-mediated colloidal assembly

Reducing dimensionality from 3D materials to 2D surfaces can offer transformative benefits in complexity, cost, attenuation loss, and computational efficiency. Nano and microstructured surfaces thus hold significant potential for advancing technology, opening new possibilities in applications such as electronics, optics, and photonics. [21, 36–38] The interface-mediated colloidal assembly is one of the promising routes for scalable fabrications, where surfaces ranging from cm^2 to m^2 scales are modified typically via drop-casting, [39] spin coating, [40] and Langmuir-Blodgett deposition. [41, 42] Categorised as a bottom-up method, as opposed to a top-down method, the colloidal assembly offers a distinct edge over other routes especially in terms of cost and time efficiency due to its inherently parallel nature. [36]

Beyond its practical potential, colloidal assembly at interfaces using, e.g., lateral barriers on Langmuir troughs, also offers a unique experimental platform to gain deeper insights into the fundamentals of the crystallisation process that occurs at interfaces. Under compression, the colloidal systems undergo gas/liquid/solid-like phase transitions [30, 43, 44] akin to those found in 3D self-assembly experiments. [45–49] It is noteworthy, however, that the confinement of colloids at interfaces gives rise to unique surface properties and behaviours. For instance, while in 3D assembly, the particle concentration (volume fraction) is the primary factor governing phase transitions, in 2D assembly, the onset of crystallization is independent of the particle concentration (area fraction). [50] In other words, many particle systems that are colloidally stable in bulk would form clusters even at low area fractions when placed at fluid/liquid interfaces. Figure 1.3 schematically illustrates such a phenomenon for HCSS microgels during a Langmuir trough compression. The importance of this aspect becomes more significant when dealing with colloids that are soft and deformable. Therefore, the discussion of the different interactions occurring at colloid-laden interfaces requires to consider how the confinement at the interface affects the colloid (e.g. morphologies, apparent roughness, shape anisotropy) and reciprocally, how the colloid deforms the interface. Studying such phenomena is challenging as it is dependent on various parameters such as size, composition, elasticity, and roughness of the colloid. [51] Much of the knowledge in 2D assembly thus has been simply derived from 3D studies to date. [52]

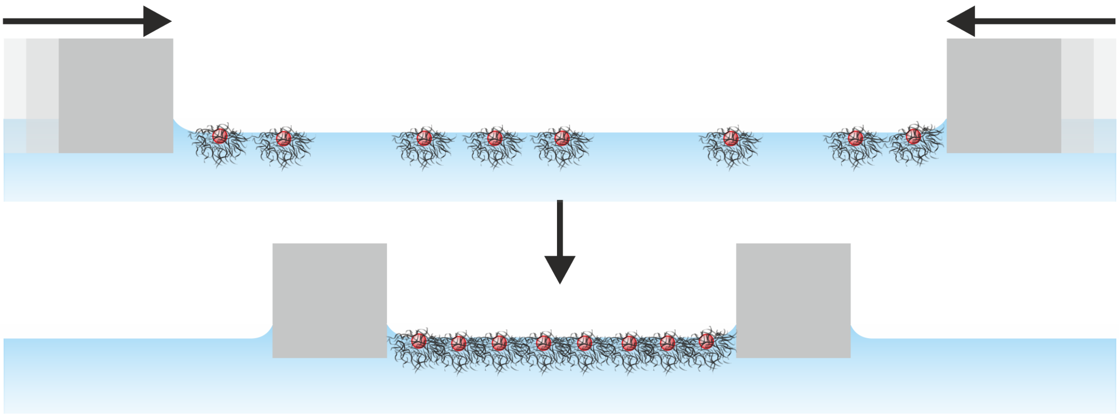

Fig. 1.3 HCSS microgel compression using a Langmuir trough.

In this thesis, I emphasise the *in situ* observation of the interface-mediated colloidal assembly process, achieved through the synthesis of micron-sized HCSS microgel model systems for *in situ* light and fluorescence microscopy. Their gas/liquid/solid-like phase transitions during compression were mapped out in both real and reciprocal spaces by combining microscopy and small-angle light scattering (SALS) with a Langmuir trough. The results of the *in situ* experiments were compared with the more commonly conducted *ex situ* experiments, which led to novel insights.

Chapter 2

Theoretical Background

2.1 “Smart” PNIPAM microgels as model systems

Microgels are solvent-swollen crosslinked polymer networks with dimensions in the submicron to micron range. [53] As mentioned in the previous section, PNIPAM is by far the most extensively explored polymer in the microgel community. It is often referred to as “smart” due to its stimuli-responsiveness in an aqueous environment, which allows “switching” its morphological structure and thus alters various properties including colloidal stability, [54] rheological characteristics [55] and interfacial properties. [56] External stimuli such as solute (e.g., salt, surfactant, protein) concentrations, pH or temperature influence its morphological structure. However, it is the response to temperature—the thermo-responsiveness—at near-physiological conditions that gave the PNIPAM its fame across the disciplines from polymer/physical chemistry to biotechnology. When exposed to a temperature above its lower critical solution temperature (LCST, approximately at 32°C), the amphiphilic PNIPAM polymer chain undergoes a reversible configurational transition—the coil-to-globule transition—leading to a phase separation. [35] This phase separation is attributed to changes in the local environment surrounding the hydrophobic domains, namely the isopropyl groups and the polymethylene backbones. [57]

In the cases of crosslinked microgels in an aqueous environment, this phase separation manifests as a volume phase transition (VPT), which enables on-demand control of the volume fraction that dictates interparticle interaction and thus their 3D assembly behaviour. [29] Even above the volume phase transition temperature (VPTT), however, the de-swollen microgels remain highly hydrated with water content above 20 wt.% [58] due to its oxygen and nitrogen rich domains. A recent study on scattering properties of small HCSS microgels (gold-PNIPAM, overall hydrodynamic diameter, D_h, around 200-300 nm) reported water contents of approximately 40-50 wt.% at temperatures above VPTT. [59] This amphiphilic nature of PNIPAM is also responsible for its surface activity, which is often essential for 2D assembly investigations of microgels.

PNIPAM microgels, most commonly synthesised via precipitation polymerisation using *N*,*N*'-methylenebisacrylamide (BIS) as a crosslinker, can be prepared with great control over the size distribution, charge per volume, chemical composition, and morphology. [60, 61] In precipitation polymerisation, all ingredients typically start as a homogeneous mixture (batch synthesis), where the monomer (and comonomer), crosslinker, and initiator are dissolved in water. At the polymerisation temperature (above VPTT), the initiator decomposes and produces free radicals, which leads to radical propagation and chain growth. [61] Alongside adjusting the concentrations of each ingredient, the architecture of the microgels can be further tailored by introducing surfactants, [62, 63] the polymerisation temperature (constant [64] or ramping [65]), monomer and crosslinker feeding method (semi-batch synthesis), [66–69] as illustrated in Figure 2.1A. Such synthesis parameters can greatly influence the distribution of the crosslinker density of the microgels and thus their characteristic, e.g., swelling property, as depicted in the middle of the figure.

The precipitation polymerisation can also be done with the presence of cores, often referred to as "seeded" precipitation polymerisation. As the polymerisation proceeds, the oligomers/polymers precipitate on the surface of the core, eventually encapsulating the core as illustrated in Figure 2.1B. The presence of the core, however, alters the colloidal stability of the mixture during the synthesis, potentially leading to flocculation. Hence, in literature, the HCSS-type microgels are often synthesised with small cores (diameter below 200 nm), and grown via stepwise feeding of the monomer. [70–73] A possible cause for such flocculation is the attractive interaction between the cores and the growing polymers. A theoretical study on factors affecting the stability of colloidal systems [74] suggested that the colloidal stability is a function of polymer concentration, C. Figure 2.1C illustrates various events that can take place in a colloidal system as the polymer concentration increases, e.g., during a HCSS microgel synthesis. Bridging flocculation can occur when a low concentration of oligomer/polymer chains are formed in the colloidally stable core dispersion (not enough to cover the surface of the cores). The system is colloidally stable, when a higher concentration of polymer is formed and saturate all core surfaces, C_{Sat}, faster than flocculation can occur. However, if the concentration of the polymer chains is too high, C_{Dep}, it may lead to depletion flocculation. [75]

Receiving a lot of attention as a subject of investigation entails its characterisation through a plethora of methods including various scattering techniques, [7, 76] super-resolution microscopy, [77] rheology, [78, 79] and modelling. [80, 81] However, despite the numerous works published on PNIPAM microgels, there are still many open questions regarding internal

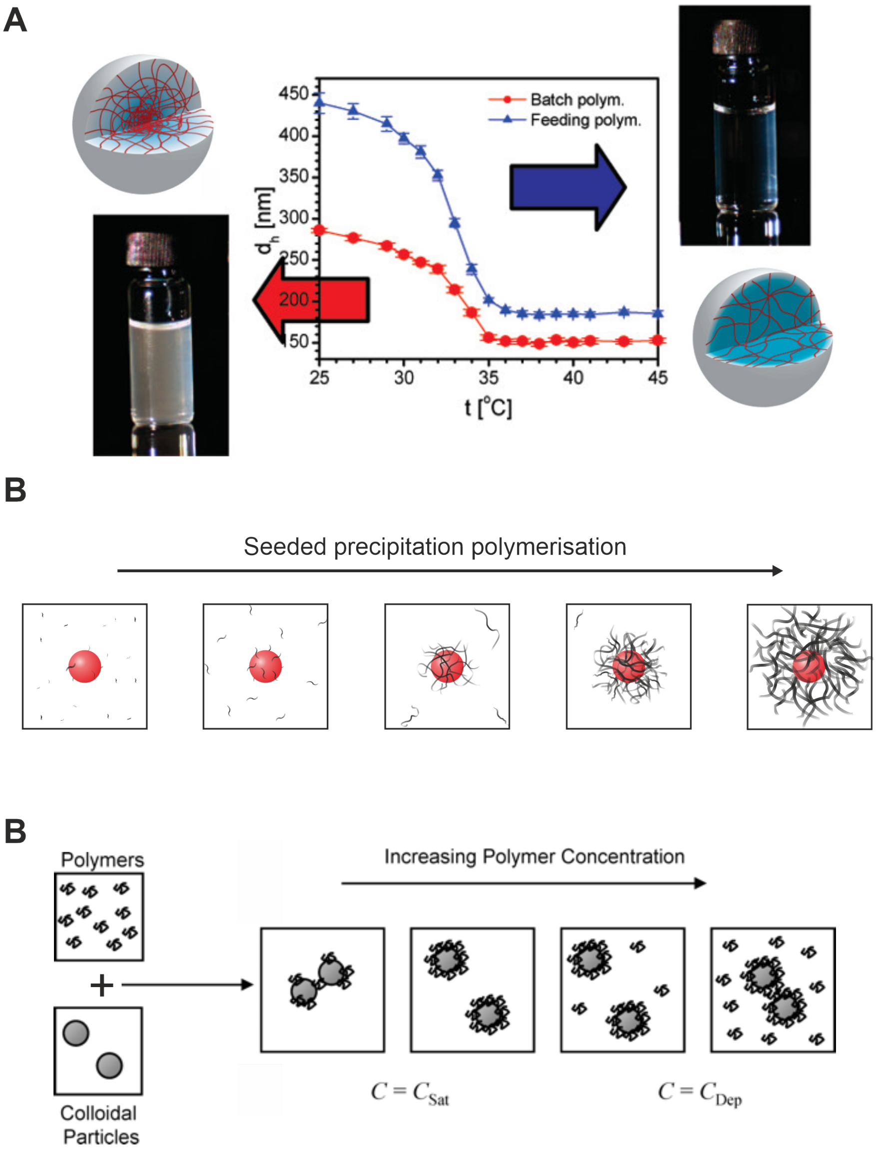

Fig. 2.1 **A**) Coreless PNIPAM microgels synthesised via two different precipitation polymerisation approaches: batch (red) and continuous feeding of monomer (blue). d_h denotes the hydrodynamic diameter and t is temperature. Adapted with permission from [64]. Copyright (2011) American Chemical Society. **B**) Schematic illustration of seeded precipitation polymerisation. **C**) Schematic diagram of the different events that can occur when adsorbing polymers are added to a colloidal dispersion. Adapted with permission from [74]. Copyright (2005) American Chemical Society.

structure, phase behaviour, and surface properties. [28] The following subsections provide the basics of characterisation methods employed in this thesis.

2.1.1 Light scattering methods

Light scattering is a ubiquitous tool for the characterisation of colloidal systems. The colloidal systems in a medium interact with the light and scatter a portion of the light from its original path, i.e., scattered light. Depending on how the intensity of this measured light is analysed, the measurement can be classified as static or dynamic light scattering. [82] Modern light scattering instruments are typically equipped with a laser (light source), a temperature-controlled sample chamber, an avalanche photodiode (APD, detector), a digital correlator, and a computer along with software for the analysis, as illustrated in Figure 2.2. The sample is usually prepared in a dilute concentration, where multiple scattering and interparticle interactions are negligible.

A fully developed theory of light scattering that takes into account all possible variables, including the size and shape of the colloidal systems, is complex. Therefore, one resorts to approximations that apply only to a specific range of such variables. [82] For example, Rayleigh approximation is restricted to small objects, such as atomic and molecular particles, whose diameter is not larger than $\lambda/20$ of the incident light and have a refractive index not too high or too low relative to the medium. Consequently, Rayleigh scattering primarily refers to the elastic scattering of light from such small objects. In contrast, Mie scattering refers to scattering from larger counterparts, approximately the size of the wavelength of the incident light. [83]

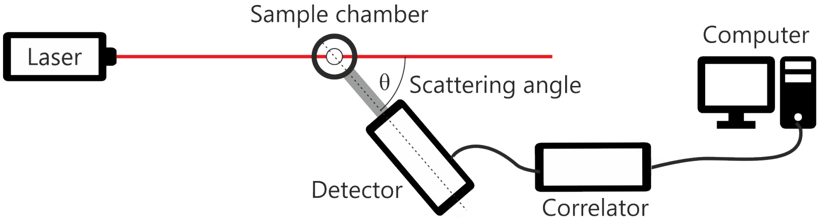

Fig. 2.2 Schematic of a typical light scattering setup.

Static light scattering (SLS) [84, 85] In SLS experiments, the time-averaged total intensity of the scattered light is measured as a function of scattering angle θ, or scattering vector $\overrightarrow{q}$.

$$|\overrightarrow{q}| = \frac{4\pi n}{\lambda_0} sin\left(\frac{\theta}{2}\right) \tag{2.1}$$

where n is the refractive index of the medium, λ_0 is the wavelength of the laser in vacuum. In general, the scattering intensity $I(q)$ can be described as [86]:

$$I(q) = N\Delta\rho^2 V^2 P(q) S(q) \tag{2.2}$$

where N is the particle number density, $\Delta\rho$ is the scattering contrast (in light scattering, it is given by the difference in refractive indices between the particle and the solvent), V is the scattering volume, $P(q)$ is the form factor, and $S(q)$ is the structure factor.

The solution for dilute dispersion ($S(q) \approx 1$) of homogeneous spheres with a low $\Delta\rho$ is given by [87]

$$I_{HS}(q,R) = N\Delta\rho^2 V^2(R) P(q,R) \tag{2.3}$$

with

$$P(q,R) = K^2(q,R) = \left(\frac{3(sin(qR) - qRcos(qR))}{(qR)^3}\right)^2 \tag{2.4}$$

where $K(q,R)$ is the form factor oscillations as a function of q and the radius of the particle, R. [86] Note that $P(q,R)$ approaches 1 for the forward scattering ($\lim_{q\to 0}$). The simulated scattering intensity profiles of spheres with various radii is illustrated in Figure 2.3.

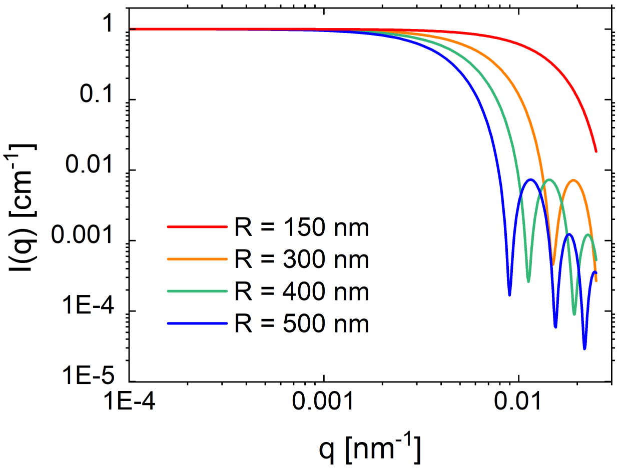

Fig. 2.3 The scattering intensity, $I(q)$, of homogeneous spheres with radii R = 150, 300, 400, 500 nm plotted using the hard sphere model.

Real microgel systems, however, exhibit certain degrees of size distribution, i.e., polydispersity, as well as various inner structures depending on the synthesis conditions, as discussed in Section 2.1. The submicron-sized microgels ($D_h \lesssim 300$ nm) are unique in that they are large yet extensively swollen with the medium (i.e., low scattering contrast), making it unnecessary to consider Mie scattering effects. The average intensity of the scattered light thus can be approximated according to the Rayleigh-Debye-Gans theory. [85]

$$I(q) = N\Delta\rho^2 \int_0^\infty D(R)V(R)^2 P(q,R)\,dR \tag{2.5}$$

where $D(R)$ is the distribution function of the particle radii (polydispersity), R. The subject of interest in this work is HCSS-type microgels, characterised by inorganic cores at the centre with parabolic “fuzzy” shells. The radial profile of such microgels is given by [88–90]:

$$\rho(r,R,\sigma) = \begin{cases} 1 & \text{for } r \leq R-\sigma \\ 1-\frac{1}{2}\frac{((r-R)+\sigma)^2}{\sigma^2} & \text{for } R-\sigma < r \leq R \\ \frac{1}{2}\frac{((R-r)+\sigma)^2}{\sigma^2} & \text{for } R < r \leq R+\sigma \\ 0 & \text{for } r > R+\sigma \end{cases} \tag{2.6}$$

where r is the radial coordinate and $R = W + \sigma$, as also illustrated in Figure 2.4. The Fourier transformation for such radial profile can be calculated as [88–90]:

$$\begin{gathered} F(q,R,\sigma) = f[\rho(q,R,\sigma)] = \\ 4\pi\Bigg(\left(\frac{R}{\sigma^2}+\frac{1}{\sigma}\right)\frac{\cos(q(R+\sigma))}{q^4}+\left(\frac{R}{\sigma^2}-\frac{1}{\sigma}\right)\frac{\cos(q(R-\sigma))}{q^4} \\ -3\frac{\sin(q(R+\sigma))}{q^5\sigma^2}-3\frac{\sin(q(R-\sigma))}{q^5\sigma^2}-6\frac{\sin(qR)}{q^5\sigma^2}-2R\frac{\cos(qR)}{q^4\sigma^2}\Bigg) \end{gathered} \tag{2.7}$$

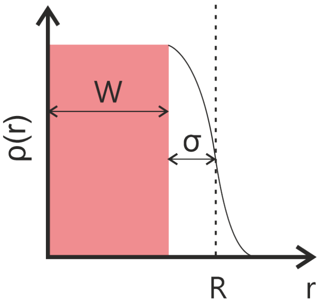

Fig. 2.4 Radial profile of HCSS-type microgels with a parabolic interface.

Various other profiles can be used for the shell, e.g., exponential decay as detailed in [86]. In experiments, the obtained form factor from the SLS measurements is fitted using a suitable model. A MATLAB program called FitIt! [85] is customisable software that is well-suited for the structural analysis of colloids by SLS. The Figure 2.5 shows example results of SLS measurements using two different laser wavelengths (λ = 407 and 819 nm) for a HCSS microgel system used in this study with a silica core sized 340 nm in diameter and an overall D_h of around 1 μm at 20°C. The fitting was done using the fuzzy_core_shell model in FitIt!. The measured data is depicted with empty scatter points, and the fitted data is represented by lines.

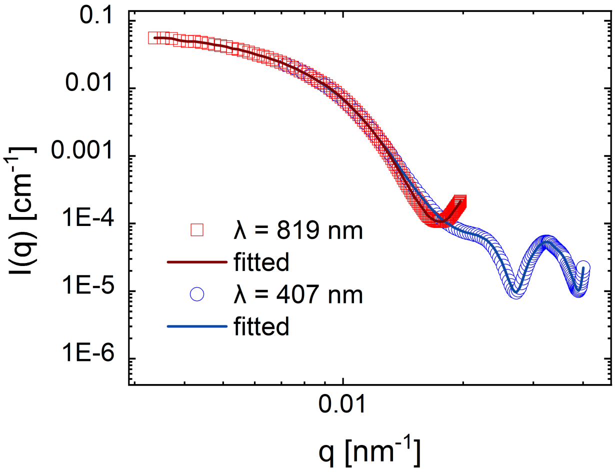

Fig. 2.5 The scattering intensity, $I(q)$, of a dilute HCSS microgel system with a core sized 340 nm in diameter and an overall hydrodynamic diameter of around 1 μm at 20°C, fitted by FitIt! [85].

While SLS serves as a valuable method for characterising microgels, the primary emphasis of this study lies in investigating the assembly behaviour of HCSS microgels and analysing the structure factor of the microstructures of the assembled microgel monolayers, as briefly explained in the upcoming Section 2.1.1.

Dynamic light scattering (DLS) [82, 91, 92] In DLS experiments, the measured intensity fluctuation of the scattered light $g^{(2)}(q,\tau)$ is converted into the intensity-intensity time autocorrelation function at a certain scattering vector q for a given delay time τ.

$$g^{(2)}(q,\tau) = \frac{\langle I(q,t)I(q,t+\tau)\rangle}{\langle I(q,t)\rangle^2} \tag{2.8}$$

$I(q,t)$ is the intensity of the scattered light at time t and $I(q,t+\tau)$ at time $t+\tau$, averaged over time t. For data analysis, the intensity-intensity time autocorrelation function can also be expressed as a field-field time autocorrelation $g^{(1)}(q,\tau)$.

$$g^{(2)}(q,\tau) = B + \beta[g^{(1)}(q,\tau)]^2 \tag{2.9}$$

with $g^{(1)}(q,\tau)$ defined as

$$g^{(1)}(q,\tau) = \frac{\langle E(q,t)E^*(q,t+\tau)\rangle}{\langle E(q,t)E^*(q,t)\rangle} \tag{2.10}$$

where $E(q,t)$ is the scattered electric field at time t and $E(q,t+\tau)$ at time $t+\tau$. β is related to the signal-to-noise ratio, which depends on the experimental geometry. When $\beta = 1$, the equation 2.9 is referred to as the Siegert relation. The equation is used to transform $g^{(2)}(q,\tau)$ to $g^{(1)}(q,\tau)$. B is the averaged value of $g^{(2)}(q,\tau)$ over a long time, also known as the baseline. For a strictly monodispersed spherical colloidal system, the field-field correlation function decays exponentially with a decay rate Γ.

$$g^{(1)}(q,\tau) = exp(-\Gamma\tau) \tag{2.11}$$

For translational diffusion, the decay rate Γ is equal to Dq^2, where D is the diffusion coefficient of the colloidal system. The Stokes-Einstein equation. The Stokes-Einstein equation relates the diffusion coefficient of the colloidal system to its hydrodynamic radius.

$$D = \frac{k_B T}{6\pi\eta R_h} \tag{2.12}$$

where k_B is Boltzmann's constant, T is temperature, η is the dynamic viscosity of the medium, and R_h is the hydrodynamic radius of the colloids.

In reality, however, colloidal systems display a certain degree of polydispersity, implying that $g^{(1)}(q,\tau)$ can no longer be accurately represented as a single exponential function but as an integral over the decay rate $G(\Gamma)$. For colloidal systems in the Rayleigh scattering regime, $g^{(1)}(\tau)$ can be expressed as

$$g^{(1)}(q,\tau) = \int_0^\infty G(\Gamma)exp(-\Gamma\tau)\,d\Gamma \tag{2.13}$$

and for the colloidal systems in the Rayleigh-Debye-Gans or Mie scattering regimes as

$$g^{(1)}(q,\tau) = \frac{\int_0^\infty G(\Gamma)B^2(q,R_h)exp(-\Gamma\tau)\,d\Gamma}{\int_0^\infty G(\Gamma)B^2(q,R_h)\,d\Gamma} \tag{2.14}$$

where $B(q,R_h)$ is the angle-dependent scattering amplitude. The analysis of the DLS data is typically carried out using the cumulant method [91] or the CONTIN algorithm. [92] The cumulant method involves applying a Taylor series expansion to the $g^{(1)}(q,\tau)$. The first cumulant coefficient provides the mean value of decay rate Γ, the second cumulant information about the polydispersity. The CONTIN algorithm, on the other hand, utilises inverse Laplace transformations to deduce the distribution of the decay rate $G(\Gamma)$. In summary, both methods are used to derive the decay rate Γ, thus determining the diffusion coefficient D

of the investigated colloidal systems. Note that, however, the measurement analysis on large and/or heavy colloidal systems under sedimentation is likely to lead to errors in measurements as well as an overestimation of polydispersity. The commonly quoted upper size limit for DLS (around 10 μm) is often only achievable by increasing the viscosity of the medium or suppressing the convective motion of the sample in a capillary cuvette. [93, 94] In this study, the primary emphasis is placed on the synthesis and 2D assembly of micron-sized microgels, consequently minimising the significance of bulk size analysis through scattering techniques.

Small-angle light scattering (SALS) SALS measurements are typically done in the angular range of 0.5°- 25°and performed primarily for studies of larger-scale structures and/or shapes. Using various lasers and sample-to-detector distance, the measurements can give a q-range between roughly 0.25 – 15.74 μm^{-1}. In experiments, where micron-sized HCSS microgels are assembled into a compact monolayer, $S(q) \approx 1$ is no longer valid in contrast to the dilute dispersions, as discussed in Section 2.1.1. In fact, $S(q)$ dominates the scattering pattern due to the large interparticle distances (a small q-range) and the relatively small size of the core. In this small q-range, the measured $I(q)$ is directly related to the structure factor $S(q)$. The lattice spacing D_{hk} can thus be calculated through Bragg’s Law, which is given by [30]

$$int\lambda = 2D_{\mathrm{hk}}sin(\theta) \tag{2.15}$$

where *int* is an integer (the order of the diffraction peak). Combining the equation 2.1 and 2.15 yields:

$$D_{\mathrm{hk}} = \frac{2\pi}{|q_{\mathrm{max}}|} \tag{2.16}$$

Setups for SLS and SALS share common elements as illustrated in Figure 2.6. The SALS setup employs a 2D detector, allowing the simultaneous collection of the scattering pattern at multiple angles, while the SLS setup is equipped with a device that changes the angle of the incident light or the detected scattered light for measuring the scattered intensity over a range of angles (often referred to as a goniometer). As for SLS data, the small-angle scattering data can be analysed by fitting models using a software tool [88, 95, 96], regardless of whether light, x-ray, or neutron is used as the scattering source.

2.1.2 Langmuir trough combined with small angle light scattering

The SALS setup illustrated in the previous section (Figure 2.6) can be coupled with other measurement instruments, such as a Langmuir trough (discussed in Section 1.2). This combination could provide valuable insights into the behaviour of colloidal assembly and

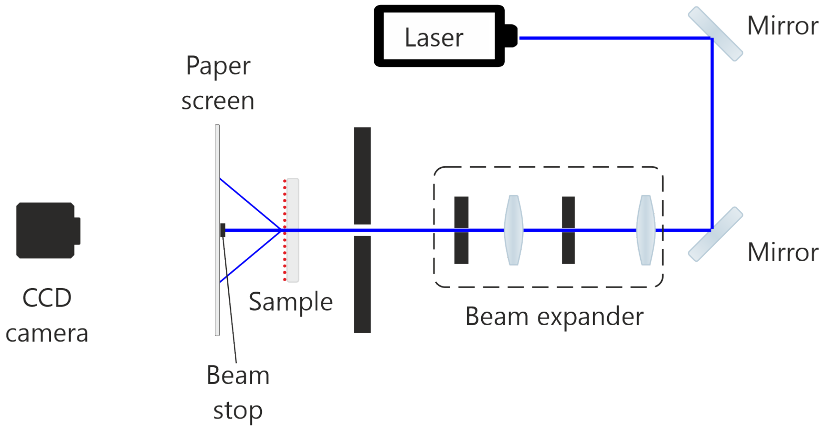

Fig. 2.6 Schematic of a small-angle light scattering setup.

phase transitions *in situ* during lateral compression. The configuration of the setup involves the use of a microscopy trough (commercially available, featuring a central window) and a detector positioned above the trough (in our case, a paper screen and a CCD camera), as depicted in Figure 2.7A. The laser is directed from beneath the trough, transmitted through the glass window, subphase (water), and the colloidal monolayer, as schematically illustrated in Figure 2.7B. The resulting diffraction patterns can then be captured and utilised for real-time structural analysis during compression. This process can also be facilitated by software, allowing for the targeting of specific interparticle distances. The detailed analysis procedures are outlined in Section 5.

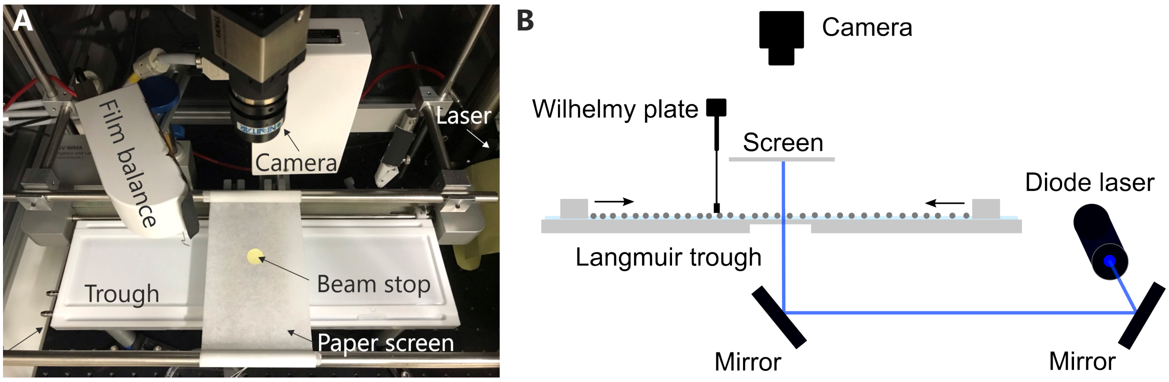

Fig. 2.7 **A**) Picture of the LT-SALS setup. **B**) Schematic illustration of the LT-SALS setup. [30]

This approach, unlike Langmuir-Blodgett deposition, allows for:

1. The complete elimination of potential effects of transfer and drying, such as immersion capillary forces, drying dynamics, and the influence of the substrate.

2. The non-invasive *in situ* observation of the relaxation and reversibility of the microgel monolayer throughout the compression in real-time. This is challenging to achieve with *in situ* microscopy due to the rapid movement of microgels during relaxation (especially early seconds) and difficulties in imaging at high compression states.
3. Investigations over a relatively larger area exceeding 1 mm^2 with great frame rates (up to 30-250 frames per second).

2.1.3 Microscopy

“A picture is worth a thousand words” is a well-known English saying that also exists in different languages. The saying emphasises that the graphically presented information (e.g., images and videos) conveys its essence more intuitively and thus more effectively than any text can. With the technological breakthroughs of the last decade, many scientific imaging techniques have transformed from qualitative to quantitative analysis methods in various fields. Recent advancements in imaging techniques, for example, have provided us with insights into the shear-induced [97] and self-assembled [98] dense 3D colloidal structures, their phase diagrams, [99] and the shape of microgels at various interfaces using cryo-scanning electron microscopy, [80, 100] *in situ* atomic force microscopy (AFM), [101] and confocal laser scanning microscopy (CLSM). [102]

For colloidal systems confined at an interface, in particular, simple light microscopy can also offer much information, such as pair potential, [103] mechanical properties, [104] and rheological properties of the colloid-laden interfaces. [105, 106] However, this is only applicable above the Abbe diffraction limit. Due to the small sizes of microgels investigated in the literature to date, the imaging on microgel samples is most commonly conducted using markers (larger or differently labelled particles), or at low concentrations, and *ex situ* via AFM and/or CLSM.

Atomic force microscopy (AFM) [107–109] Classified as one of the scanning probe microscopies, AFM allows high-resolution topographical imaging (as high as 0.1 nm in vertical resolution, and 1 nm for the lateral resolution [107]) and measurement of forces and elasticity of the sample using a microfabricated cantilever with a sharp tip, typically made of silicon. A schematic illustration of AFM is depicted in Figure 2.8. AFM has advantages, as virtually any solid surface can be probed in the xyz direction without any surface preparation, including the surface of swollen microgels in water. [110, 111] Its drawbacks are a relatively slow scanning speed and a smaller imaging area compared to other microscopic techniques.

The operation mode of AFM can also be divided into two categories: static and dynamic. In the static operation mode, a soft cantilever (low spring constant, k) is used to probe the z map of the sample surface. The deformation of the tip and sample should be significantly weaker than the deflection $q' = F_{ts}/k$. F_{ts} denotes tip-sample force $F_{ts} = -\delta V_{ts}/\delta z$, where V_{ts} is the potential energy between the tip and sample. In AFM measurements, F_{ts} includes short and long-range contributions such as van der Waals, electrostatic, magnetic, and dipole-dipole interactions. The deflection of the cantilever is detected through the laser reflected on the back of the cantilever to the position-sensitive photodiode, as illustrated in Figure 2.8. Interatomic force constants in solid samples commonly range from 10 to 100 N/m, and they can be as small as 0.1 N/m in biological samples. Thus, typical values for k in the static mode lie between 0.01 – 5 N/m. [108]

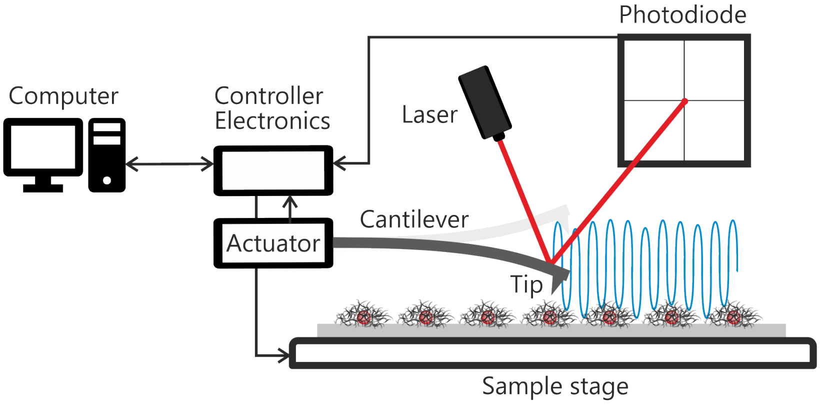

Fig. 2.8 Schematic illustration of an AFM scanning a sample in a dynamic operating mode.

In the dynamic operation modes, the cantilever is vibrated by an actuator. When the tip approaches the sample, F_{ts} causes a change in both the amplitude and the phase of the cantilever. This change is then used as the feedback signal for the surface topographic information. When the cantilever oscillates near its resonant frequency (approximately 300 kHz), the tip is made to “tap” the surface, hence referred to as “tapping mode”. The oscillation amplitude typically ranges from 20 - 100 nm. For samples that are susceptible to damage, a non-contact mode can be used where the cantilever oscillates at a smaller amplitude (< 5 nm). [107]

Confocal laser scanning microscopy (CLSM) [112–115]

The resolution of CLSM is lower than that in the transmission electron microscope (0.1 nm) and a little better than that in a conventional light microscope, which is achieved by spatial filtering: elimination of out-of-focus rays. In other words, the illumination and detection in the CLSM are confined to a single point (focused beam) in the sample. Built around a conventional light microscope, CLSM uses a laser instead of a lamp as a light source, a detector (e.g., PMT—photomultiplier, APD), and a computer to control the scanning mirrors as well as to process the collected images, as illustrated in Figure 2.9.

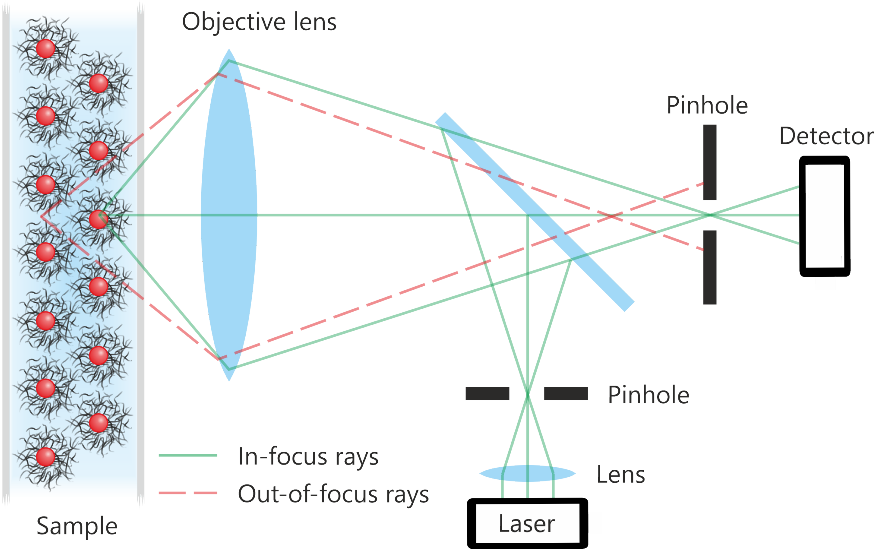

Fig. 2.9 Schematic illustration of a CLSM and its typical light path.

The image collection can be performed at different levels from the sample (i.e., deep within the sample). This imaging mode is commonly referred to as z-series, where the stepping motor of the sample stage is precisely coordinated with the movement of the focus of the microscope by pre-set distances. The collected images are then further processed into a 3D representation of the sample using volume visualisation techniques. This 3D imaging technique holds great interest within the colloid community as it offers local structural information, which light scattering (average over a large ensemble) cannot deliver. The same technique can be employed in a time-lapse manner, effectively utilising time as the “z-axis”. This enables time-dependent observation of the local structural development in the sample.

While CLSM can offer a broader range of imaging modes and better resolution compared to conventional light microscopy, it is not without its limitations, some of which do not apply to light microscopy. One such drawback is the requirement for the sample to be fluorescently labelled. Furthermore, photobleaching of the fluorophores is potentially a serious problem in CLSM, which occurs while the scanning point is in motion and during the data collection process, affecting the quality of the data. [114]

2.2 Interparticle interaction

The description of the crystallisation process in a system typically commences with the nucleation mechanism and growth from the metastable critical point irrespective of the dimension of the building block. [99] These early stages of crystallisation play a critical role in the properties of the resulting crystal structure, its distribution and morphology. [116] And the interactions among the building blocks and their environment dictate the outcome of these processes. The classical nucleation theory predicts the cost of nucleation formation, ΔG, is the sum of the change in free energy for the phase transformation, ΔG_v and the change in free energy for the surface formation, ΔG_s.

$$\Delta G = \Delta G_s + \Delta G_v = 4\pi R^2 \gamma + \frac{4}{3}\pi R^3 \Delta\mu \tag{2.17}$$

where R is the radius of the spherical nucleus, γ is the interfacial free energy, and $\Delta\mu$ is the chemical potential difference per unit volume. For large enough R, the volume contribution begins to dominate the surface term, where the nucleus becomes stable. This critical point for the liquid-crystal phase transition can be defined as where $d\Delta G/dr = 0$. [99, 116] A simple hard sphere model system can serve as a useful abstraction to study such phase transitions. In this model, we consider an isolated system in a volume V at an energy E, where the highly monodispersed spheres interact via a steep repulsive potential without overlapping with one another. Consequently, the phase transition of the system is solely driven by configurational entropy. The thermodynamic behaviour of such systems can thus be understood through the entropy term. [16, 117]

$$S = k_B \ln \Omega \tag{2.18}$$

where Ω is the total number of accessible configurational states of a system. According to the entropic calculation, the system undergoes crystallisation when the volume fraction of hard spheres increases, as illustrated in Figure 2.10a. Beyond the volume fraction 0.494, commonly referred to as the "freezing point, Φ_f", some spheres start to crystallise because it is entropically more favourable. And above the volume fraction 0.545, the "melting point, Φ_m", all spheres are in a crystal. [45, 118] These transitions were experimentally realised using sub-micron-sized polymethyl methacrylate (PMMA) particles dispersed in an index-matched and non-polar continuous phase aboard the Space Shuttles Columbia and Discovery (microgravity environment). [45] When long-ranged attraction is introduced into the equation, the system exhibits three-phase equilibria, as found in atomic systems. In the presence of shorter-ranged attractions, the liquid-liquid equilibrium becomes metastable, as observed in many protein systems. [99]

2.2.1 DLVO theory

Colloids dispersed in a continuous phase, i.e., colloids separated by the continuous phase that also interacts with the colloids can be described by Derjaguin-Landau-Verwey-Overbeek (DLVO) theory. This theoretical framework is attributed to the scientific contributions of

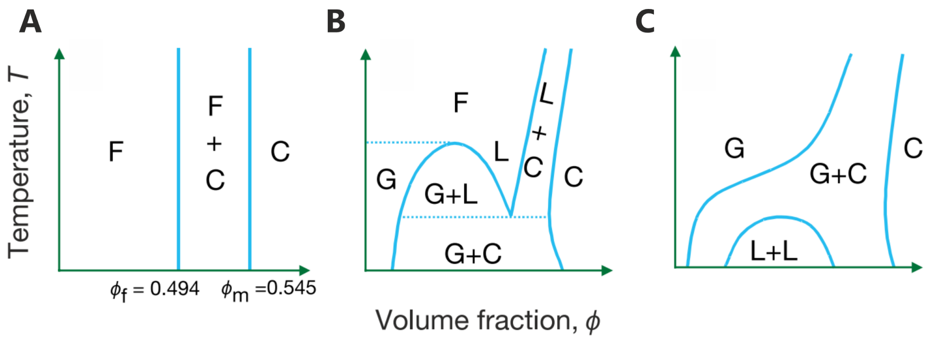

Fig. 2.10 Phase diagrams of hard sphere systems with various interactions. **A**) For a simple hard sphere system with a steep repulsive potential. The phase diagram shows the fluid (F) phase and crystal (C) phase with the fluid/crystal coexistence region between the freezing point Φ_f and the melting point Φ_m. **B**) The long-ranged attraction among hard spheres leads to three-phase equilibria among gas (G), liquid (L), and crystal. **C**) When the attraction becomes short-ranged, the system exhibits equilibrium between gas and crystal. Adapted with permission from [99]. Copyright (2002) Springer Nature.

Derjaguin and Landau, [119] Verwey and Overbeek, [120] and it bears great importance in liquid-state physics and colloid science, arguably comparable to Darwin's theory or origin of species in Biology. [121, 122] With the attractive van der Waals and repulsive electric double-layer interactions at its core, the DLVO theory provides a conceptually simple description of the physics of lyophobic colloid stability.

Van der Waals forces are weak attractive forces that are ubiquitous among all atoms, molecules and colloids due to fluctuations in electron distribution. The interaction potential calculation is typically done as a function of distance and by volume integration approach. [123] Consequently, the strength of the interaction is dependent on the geometry and the distance between the interacting bodies, d, as depicted in Figure 2.11A. Figure 2.11B illustrates how the shape of the interacting bodies influences van der Waals interaction, $W_{VDW}(d)$. For the evaluation of the interaction strength between two spherical bodies, the Derjaguin approximation is frequently used, which states that the interaction energy between the two curved surfaces scales with that between planar surfaces if d is smaller than the radius of the spheres, R, where $W_{VDW}(d)$ is given by [122]

$$W_{VDW}(d) = -\frac{H_{121}R}{12d} \tag{2.19}$$

The Hamaker constant, H_{121}, quantifies the strength of the van der Waals forces between two materials under the assumption that the surrounding liquid has bulk properties (ignoring any surface-induced phenomena). [121, 124]

The other major force that exists in almost all interactions in colloid science is the repulsive electric double-layer interaction, stemming from surface charges. It is noteworthy that the force acting between charged surfaces within a continuous phase containing counterions is, counterintuitively, attractive if purely through electrostatic interaction. The net interaction is negative because the entropy contribution always dominates, as predicted by the Poisson-Boltzmann equation [51]:

$$\frac{d^2\Psi(x)}{dx^2} = -\frac{e}{\varepsilon\varepsilon_0}\sum z_i n_{i(\Psi=0)} e^{-\frac{z_i e\Psi(x)}{k_B T}} \tag{2.20}$$

where $\Psi(x)$ is the electrical potential at position x, e is the elementary charge, ε is the relative permittivity of the continuous phase, and ε_0 is the permittivity of vacuum, z is the valence of the ion, $n(x)$ is the ion concentration at position x, k_B is the Boltzmann constant, and T is the temperature. Using the Derjaguin approximation for spherical particles, the electric double-layer interaction can be expressed as [51]:

$$W_{DL}(d) = \frac{2\pi R\sigma^2}{k_D^2\varepsilon\varepsilon_0} e^{-k_D d} \tag{2.21}$$

where σ is surface charge density, and k_D is the Debye screening wave vector that depends on the composition and temperature of the electrolyte. The equation is valid for all kinds of electrolytes as long as the surface potential is low, i.e., the Debye approximation holds and the inverse of the Debye screening wave vector, so-called the Debye length, λ_D, is determined precisely. The total DLVO interaction energy then can be obtained by summing these two major interactions [51]:

$$W_{DLVO}(d) = W_{VDW}(d) + W_{DL}(d) = -\frac{H_{121}R}{12d} + \frac{2\pi R\sigma^2}{k_D^2\varepsilon\varepsilon_0} e^{-k_D d} \tag{2.22}$$

The net interaction energy is influenced by the size and shape of the interacting bodies, as seen in Figure 2.11C, among other factors, for instance, ionic strength (Figure 2.11D), pH, charge density and distribution.

Although the DLVO theory accurately predicts the long-ranged interactions that are determinants for colloidal stability, there are clear deviations when the distance between the surfaces is short-ranged. [121, 122] When present, other forces such as the hydrogen bonding, hydrophobic, and capillary forces often dominate the interaction. [51, 122, 125] Therefore, one must be well aware of the assumptions of DLVO theory and its limitations. These aspects are extensively discussed in reference [121]. Summarised below are the key assumptions of the theory, adapted from the reference:

1. The surfaces are solid and exhibit molecular-level smoothness.

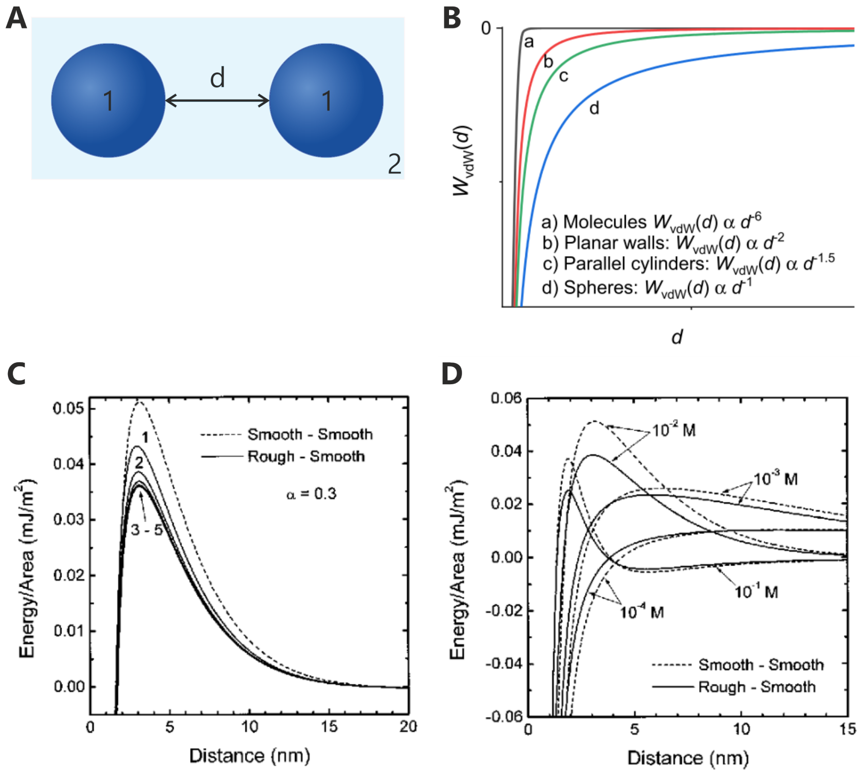

Fig. 2.11 **A**) Two smooth and solid spheres (1) interacting in a continuous phase (2) at a separation distance, d. **B**) $W_{VDW}(d)$ for various geometries of the interacting bodies. [122] Copyright (2023) Springer Nature. **C**) DLVO interaction energy per unit area between a smooth and a rough planar surface as a function of d for different roughness parameters (denoted as σ in the graph) and **D**) for different ionic concentrations. **C**-**D**) are adapted with permission from [123]. Copyright (1998) American Chemical Society.

2. The water retains bulk properties up to the interface.
3. The van der Waals interaction between the plates is computed based on the assumption of uniform water density and orientation.
4. The double-layer interaction is calculated using the non-linear Poisson-Boltzmann equation for point charges, with constant charge boundary conditions.
5. The two major forces are treated as independent and assumed additive.
6. Contact angles are not considered.

2.2.2 Hard spheres at fluid/liquid interfaces

The topic "colloids at interfaces", both planar and curved, witnessed a remarkable surge in interest over the past decade, propelled by the advances in nanotechnology for the production of new materials and the utilisation of Pickering emulsions [126] and foams in food, cosmetic, pharmaceutical industries, refinery and purification applications, especially where the presence of surfactants are undesirable due to the associated adverse effects. [127–130] The behaviour of particle-laden interfaces is however not as straightforward as the surfactant-laden counterpart. Many experimental studies and reviews on the topic have indeed shown a multifaceted phenomenology, which led to a substantial volume of research dedicated to theoretical frameworks to comprehend the phenomena. [51, 129, 131] In this section, I focus on the hard (solid and smooth) spherical particles at a planar air/water interface, as depicted in Figure 2.12A. This focus aims to provide a concise explanation of the essential aspects required for understanding its interfacial behaviour, which is distinct from its behaviour within the continuous phase (bulk behaviour).

When adsorbed at air (a)/water (w) interfaces, particles are considered to be effectively irreversibly trapped, unlike surfactant molecules that can desorb and re-adsorb relatively quickly. This distinction arises from the significantly higher detachment energy E_{det} of the particles compared to the thermal energy k_BT [127]:

$$E_{det} = \pi R^2 \gamma_{a/w} (1 \pm \cos\theta)^2 \tag{2.23}$$

where $\gamma_{a/w}$ is the interfacial tension of the air/water interface, and θ is the contact angle (the line tension acting at the three-phase contact line is ignored). Figure 2.12B shows the detachment energy E_{det} normalised by k_BT as a function of θ and R. This energetically favourable confinement of the particles at the interfaces can also be understood in terms of interfacial tension and energy cost from creating the contact area. For small particles with negligible interactions among them, i.e. the system allows free desorption and re-adsorption and has low interfacial excess concentration, Γ_i, the effective interfacial tension of the particle-laden interface, γ, can be given by [51]:

$$\gamma = \gamma_{a/w} - \Pi(\Gamma_i) = \left(\frac{\partial G_\gamma}{\partial A}\right)_{\Gamma_i} \tag{2.24}$$

with $\Pi(\Gamma_i) = \Gamma_i \left|E_{det}\right|$, where Π is the surface pressure and G_γ is the energy cost for creating contact area, A. These simple models not only provide a lucid illustration of how particle size and wettability play a crucial role in their adsorption at interfaces but also offer a reasonably accurate depiction of nano- and micro-sized particles at the interfaces. [132] It is noteworthy, however, that there are regions where the number of particles at the interfaces does not lead to appreciable changes in interfacial tension. [51, 128] Hence, the measured interfacial tension, often expressed in terms of surface pressure, Π, should be only interpreted from a macroscopic point of view.

Van der Waals and electric double-layer interactions at interfaces. The van der Waals interaction between particles becomes more intricate at the air/water interface compared to bulk interactions due to the need to account for the fractional volume immersed in both the water and the air phases. The effective Hamaker constant of the particles at the interface, H_{int}, can be estimated by introducing a fractional immersion parameter, $m = (1 - \cos\theta)/2$, and the Hamaker constants for each phase [51, 129], allowing the calculation of averaged van der Waals interaction at the interface:

$$H_{int} = H_{vac} + m^2(3 - 2m)(H_w - H_{vac}) \tag{2.25}$$

$$W_{VDW,int}(d) = -\frac{H_{int}R}{6d} \tag{2.26}$$

where H_{vac} is the Hamaker constant of the particles in vacuum and H_w in water. This approach demonstrates that the van der Waals interaction between two particles at the interface is likely to be stronger compared to their interaction in bulk. However, it is essential to note that this simplified approach ignores the thickness of the interface and the interactions may be very sensitive to changes in m as well as solvent conditions. [51, 129]

The electric double-layer interaction between two charged particles at the air (nonpolar)/water (polar) interface exhibits asymmetry (asymmetric double-layer) owing to the uneven distribution of ion clouds, which gives rise to an electric dipole moment, μ, as depicted in Figure 2.12C. Consequently, the particles confined at the interface interact through repulsive dipole-dipole interaction at a long range (where the potential is smaller than k_BT and the point charge assumption charge holds). At shorter distances, the repulsive electric double-layer interaction is expected to be a more substantial contributor. [129] The overall electric double-layer interaction between two charged particles at the interface can thus be expressed as [51]:

$$W_{DL,int}(d) = \frac{a_1 k_B T}{3d} e^{-k_D d} + \frac{a_2 k_B T}{d^3} \tag{2.27}$$

where a_1 is a pre-factor that accounts for the importance of the screened Coulomb potential and a_2 for the dipole-dipole interaction. Here, d equals the centre-to-centre distance as the particles are regarded as point charges. A recent theoretical study [133] indicates that the electric double-layer interaction between two charged particles at the interface is mostly repulsive also at a shorter range where the radius of the particles can no longer be ignored.

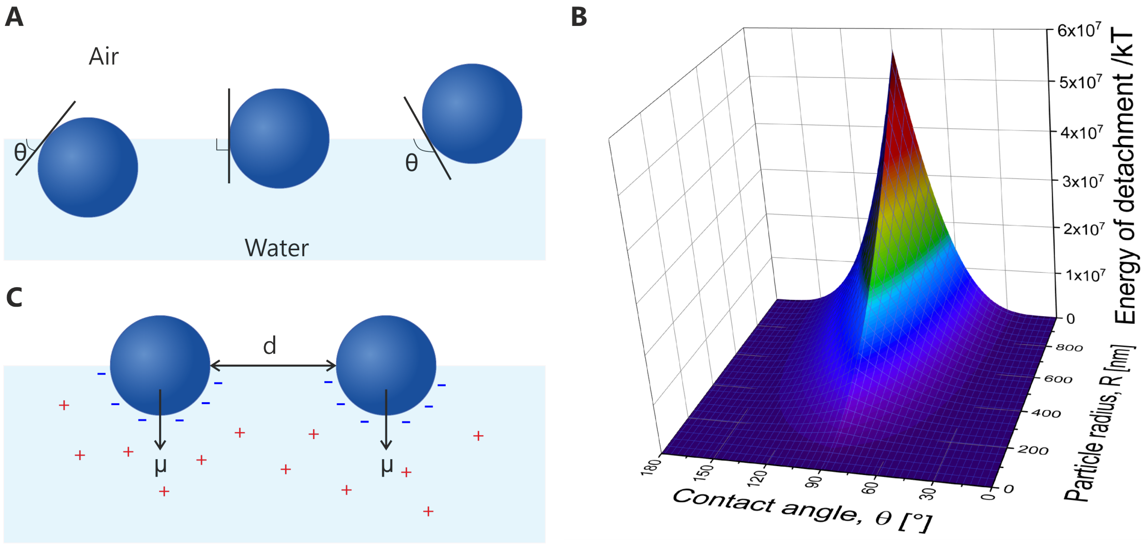

Fig. 2.12 **A**) Spherical particles resting at a planar air/water interface at contact angles, θ, less than 90°(left), equal to 90°(centre), and greater than 90°. **B**) The energy required to detach a single spherical particle with radius R from a planar air/water interface (interfacial tension 73 mN/m) resting at a contact angle of θ at temperature 298 K. **C**) The asymmetric distribution of ion clouds near the interfaces leads to an electric dipole moment, μ.

Capillary interactions. Particle adsorption at the interfaces often accompanies the deformation of the interface, which will give rise to capillary forces. This subsection is dedicated to providing qualitative descriptions of these forces. The extensive and pioneering work of Kralchevsky et al. has identified four different origins of capillary interactions. [131, 134–137]

1) The size and weight of the particle: Typically, particles larger than 5-10 μm in diameter are subject to gravitational effects, which deform the interface as illustrated in Figures 2.13A and C. This gravity-induced lateral capillary force is commonly known as “flotation force” and can be either attractive or repulsive depending on the signs of the meniscus slope angles Ψ_1 and Ψ_2. In general, the interaction is attractive among similar particles, i.e., the menisci are both concave or convex. [131]

2) The wettability of the particles in liquid thin films (free-standing or on substrates, as depicted in Figures 2.13B, D and F): Often referred to as “immersion force”, the force can be responsible for experimentally observed particle aggregation and ordering across a wide range of length scales, as shown in Figure 2.13G. Unlike the flotation force, the immersion force increases with the increasing interfacial tension. [129]

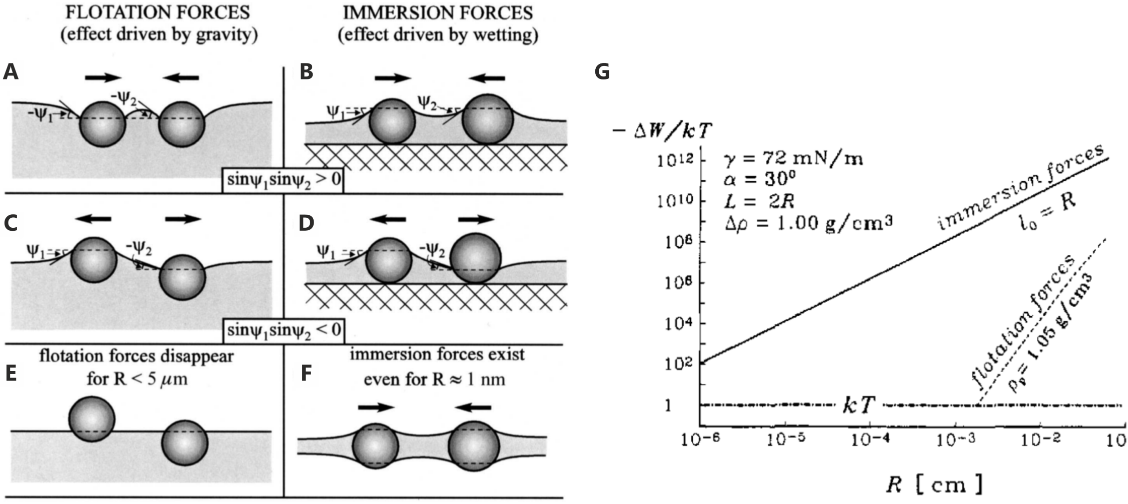

Fig. 2.13 Two types of capillary interactions: **A**,**C**,**E**) flotation and **B**,**D**,**F**) immersion capillary forces between two particles. **A**) Attractive flotation forces between similar particles with their meniscus slope angles denoted as Ψ_1 and Ψ_2 in the figure. **B**) Attractive immersion forces between similar particles in a liquid thin film on a substrate. **C**) Repulsive floatation forces between a light and a heavy particle. **D**) Repulsive immersion forces between a hydrophilic and a hydrophobic particle. **E**) The flotation capillary interactions are only operative if the particles are large and/or heavy ($R > 5\mu m$). **F**) Even the small particles experience the immersion capillary interaction in a liquid thin film due to the stronger deformation of the interface. Adapted with permission from [134]. Copyright (2000) Elsevier. **G**) Comparison between floatation and immersion capillary forces as a function of particle radius R. In the figure, Δ W denotes the capillary interaction energy, α is the contact angle, L is the distance between the particles, and $\Delta\rho$ is the difference between the mass densities of the gas (air) and liquid (water) phase. Adapted with permission from [50]. Copyright (1992) American Chemical Society.

3) Surface charge of the particles: The charge carried by particles can also induce the deformation of the interface. This electric-field-induced so-called “electrocapillary force” can also be relevant for the nano- and micro-particles that are not affected by gravity. [129]

Charged particles experience a pulling force toward the phase with a higher dielectric constant (water). While this force coexists with electrostatic repulsion, it can significantly influence the self-assembly of the particles at the interface. [131]

4) The undulated three-phase contact line: The undulation (or irregularity) of a contact line can result from various factors, including chemical inhomogeneity, surface roughness, and shape anisotropy. The capillary interactions arising from such contact lines are often referred to as "multipole interactions" due to the mathematical framework employed to describe these interactions, known as multipole expansion, [131] which is frequently used in the study of electromagnetic fields. In analogy with the Coulombic interaction, a particle with a planar contact line can be viewed as a capillary “charge” (Figure 2.14A) and the interaction between two particles with undulating particles as “dipole-dipole”, “quadrupole-quadrupole” (Figure 2.14B), “hexapole-hexapole” (Figure 2.14C) interactions, etc. [138] These forces are expected to be nonmonotonic, i.e., attractive at a long range and repulsive at a short range. [131]

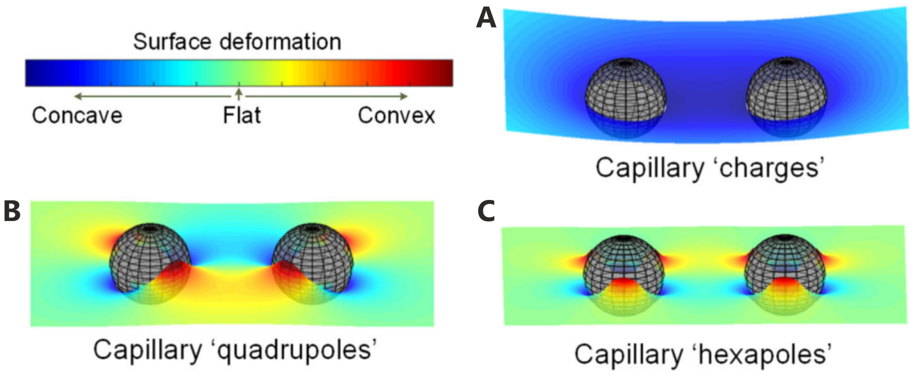

Fig. 2.14 3D surface illustrations of **A**) the capillary charges, **B**) quadrupole-quadrupole, and **C**) hexapole-hexapole interactions between two particles. Adapted with permission from [138]. Copyright (2022) Springer Nature.

It is well-established that particles adsorbed at interfaces can serve as valuable model systems for exploring fundamental questions in condensed matter physics, such as the behaviour of 2D crystals and interface-assisted self-assembly. Nonetheless, there are still many aspects, which require new theoretical approaches and experimental systematic studies. [51] For instance, one recent study on micron-sized ellipsoids of similar size, shape, and chemistry—varying between smooth, rough, and porous surfaces—has intriguingly revealed that the nanoscale porosity leads to a reduction in capillary interaction by an order of magnitude and the disappearance of the quadrupolar deformation. [139] Another experimental study on millimetre-scale particles demonstrated that the force required to extract the particle from the clean and empty air/water interface is higher than it is from the interface laden with the same particle which calls for a theoretical description for the effective interfacial properties of particle-laden interfaces. [140] Furthermore, the difficulties in obtaining interfacial structure surrounding nano- and micro-particles still present a significant challenge. Therefore, it is crucial to have a close collaboration between experimental and theoretical approaches to attain a comprehensive understanding of the interactions among the particles at interfaces. [129]

2.2.3 Microgels at fluid/liquid interfaces

The amphiphilic PNIPAM microgels are also readily adsorbed at interfaces and self-assembled. Unlike monolayers assembled from hard spheres and similar systems, which have a single characteristic length scale, microgel systems offer a broader range of interparticle distances due to their deformable nature. However, this deformable nature of microgels also adds an extra layer of complexity to the comprehension of the interparticle interactions among microgels at the interface.

Microgels synthesised through batch precipitation polymerisation typically obtain a "core-shell" structure, i.e., more densely crosslinked inner "core" region and relatively loosely crosslinked outer "shell" region. [64, 28, 110] When these microgels adsorb at the fluid/liquid interfaces, they undergo deformation due to the interfacial tension. The extent of deformation is a result of the competition between the bulk elasticity of the microgels and interfacial tension. [80, 141] The interactions between two microgels at a fluid/liquid interface, as schematically depicted in Figure 2.15, can be described as interactions between anisotropic and highly hydrated deformable bodies with nano-scale porosity as well as charge gradients. The interactions encompass a spectrum of forces including long-ranged ones such as capillary, electric double-layer, hydrophobic, van der Waals, and hydrophobic interactions, which will depend on the crosslinker density, overall hydrodynamic size and core size of the microgels [71] as well as the properties of the fluid/liquid interface. [80] As the microgels approach each other, they experience steric interactions through the dangling ends of the polymer chains, and potentially solvation, fluctuation forces, and others. [129, 142] Further compression of the two will eventually lead to further deformation and thus a change in the effective contact angle as well as the adsorption energy of the microgels. [80, 143] It is these interactions among microgels that govern their self-assembly behaviour at interfaces. It is worth noting, however, that a more comprehensive theoretical framework is necessary to describe such complex physical interactions.

In an experimental setting, the assembly of microgel-type model systems are often investigated using, e.g., Langmuir-Blodgett deposition, as illustrated in Figure 2.16A. Microgels dispersed in a "spreading agent"—a solvent or a solvent mixture that assists in the spreading

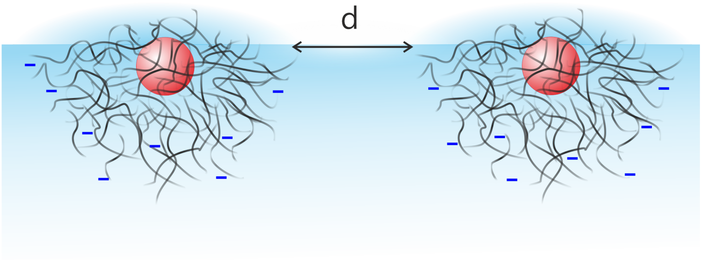

Fig. 2.15 Schematic illustration of two HCSS-type microgels at the air/water interface.

of the microgels—are floated at the fluid/liquid interface and compressed by the lateral barriers. The compression state is commonly recorded in terms of surface pressure, Π. During the compression, the microgel monolayer is simultaneously transferred to a substrate (cleaned or plasma-treated silicon wafers or glass substrates are commonly used) and dried as the substrate is pulled out. This technique allows the tracking of the link between the substrate position to the corresponding Π, under the assumption that the number of microgels deposited on the substrate per time is negligible and does not influence the measured Π. Figure 2.16B shows schematic illustrations of such microgel monolayers with an increasing number of microgels per unit area. Imaging of such microgel monolayers is commonly conducted in *ex situ* often by AFM featuring their characteristic structures resembling "fried eggs", [144–146] as depicted in Figure 2.16C, due to the small sizes and low optical contrast (the hydrodynamic diameter is typically below 1 micrometre and synthesised without inorganic cores that have higher refractive indices). By incorporating dye components into the microgel network, one could utilise *in situ* fluorescence microscopies. In this approach, however, there is an upper limit in the degree of compression before the monolayer becomes a plane of emission and a lower limit in the size of the microgel (Abbe limit). Shock freezing the microgel-laden oil/water interface can also give access to the microstructure of the monolayers as shown in Figure 2.16D. This method, Freeze-fracture shadow-casting cryo-scanning electron microscopy (FreSCa cryo-SEM), is a recently developed sample preparation method, which enables an inspection of colloids adsorbed at the millimetre-sized planar oil/water interface using SEM. [147–149]

As an be seen in Figures 2.16C and D, many microgel monolayers go through a distinctive phase, where two different lattice constants are observed. [150–154] The longer lattice constant is often described as the length scale corresponding to the distance between two microgels in “shell-shell” contact, while the shorter one represents the distance in “core-core” distance. This phenomenon is commonly referred to as an “isostructural solid-solid phase transition” because both microstructures with these two lattice constants exhibit hexagonal symmetry. [150] The underlying causes of this phenomenon are believed to be mechanical failure within the microgel network and/or capillary attractive forces. [17, 150]

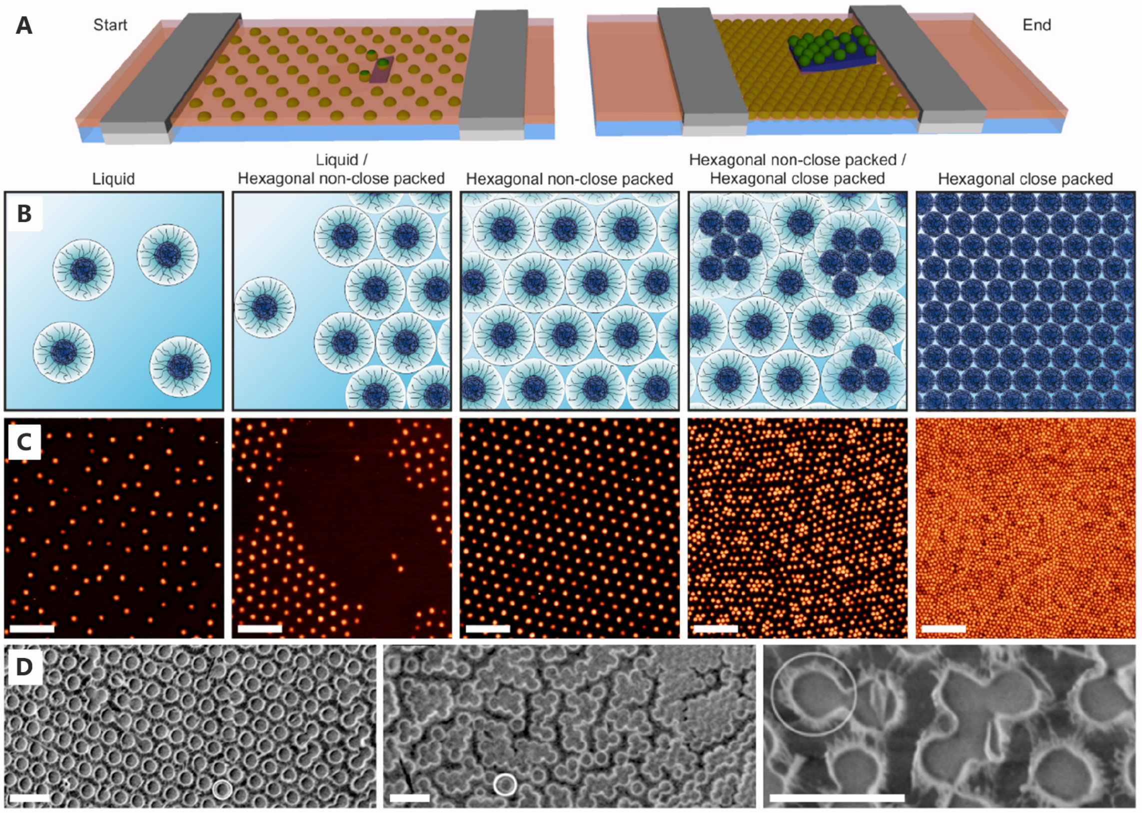

Fig. 2.16 Interface-assisted microgel assembly. **A**) Schematic illustration of microgel monolayer transfer on a solid substrate via Langmuir-Blodgett deposition during the compression. **B**) Schematic representation of the microgel monolayer with increasing number density and **C**) the corresponding AFM images. Adapted with permission from [145] Copyright (2020) American Chemical Society, original source [150] Copyright (2016) Royal Society of Chemistry. **D**) FreSCa cryo-SEM images of similarly structured microgels at an oil/water interface. Adapted with permission from [155] Copyright (2011). American Chemical Society. All scale bars correspond to 2 μm.

2.3 Simulation and experimental studies

Jagla potential-like models assume the interactions between such core-shell structured systems as (Figure 2.17A):

$$U(R) = \begin{cases} \infty, & \text{for } D_{\text{c-c}} < 2R_0 \\ v, & \text{for } 2R_0 < D_{\text{c-c}} < 2R_1 \\ 0, & \text{for } D_{\text{c-c}} > 2R_1 \end{cases} \tag{2.28}$$

where $U(R)$ is the pair-potential, $D_{\text{c-c}}$ is the centre-to-centre distance, and v is the energy profile of the shell, which can be described as a constant (shoulder potential) [11, 156] or by a function. [13, 157, 12] The shells are fully inter-penetrable and interact through a purely repulsive potential. The interactions experienced by the pair thus can be characterised by three different regimes. In the first regime, at low particle concentrations, the particles maintain a separation such that $D_{\text{c-c}}$ exceeds the diameter of the individual particles. Transitioning to the second regime, an increase in particle concentration or further compression results in the contact between the shells (shell-shell contact). In the final regime, the shells fully overlap and the cores touch, leading to core-core contact. If the energy difference between partially and fully overlapped shells is small enough, energy minimisation can be achieved by shell overlap in some directions at the cost of other neighbouring shells. This competition between these two length scales—shell-shell contact and core-core contact—gives rise to various building blocks of three HCSS particles such as collapsed equilateral (C), short isosceles (S), long isosceles (L), and expanded equilateral (E) triangles (Figure 2.17B) for non-hexagonal structures (Figures 2.17C-H), as detailed in the reference. [11]

Numerous experimental efforts have been made to realise such fascinating structures using microgels with varying hydrodynamic sizes, shell-to-core size ratios, and crosslinker densities. For example, Fernandez-Rodriguez et al. [158] have demonstrated complex tessellations via double deposition using PNIPAM microgels (hydrodynamic diameter, D_h = 600 - 900 *nm*) assembled at the hexane/water interface. They also demonstrated the rectangular ordering of the microgels at near-zero surface pressure via Langmuir-Blodgett deposition. [159] The team reported that the deposition process appears to promote the rectangular arrangement of the microgels as *in situ* monitoring of the monolayers exhibits Brownian motion and is generally more disordered. Rey et al. have shown square and chain ordering of a binary system consisting of polystyrene microspheres (diameter, D = 1500 *nm*) and PNIPAM microgels (D_h = 150 *nm*) at the air/water interface. Menath et al. [160] have reported the chain ordering of hairy particles along with various cluster formations. However, the predicted anisotropic collapses (Figure 2.17B, short isosceles (S) and long isosceles (L) triangles) of the microgels are seldom observed. [17, 56, 72, 150–152, 161–163] The discrepancies between the experimental studies and the simulations are not yet well understood. [164]

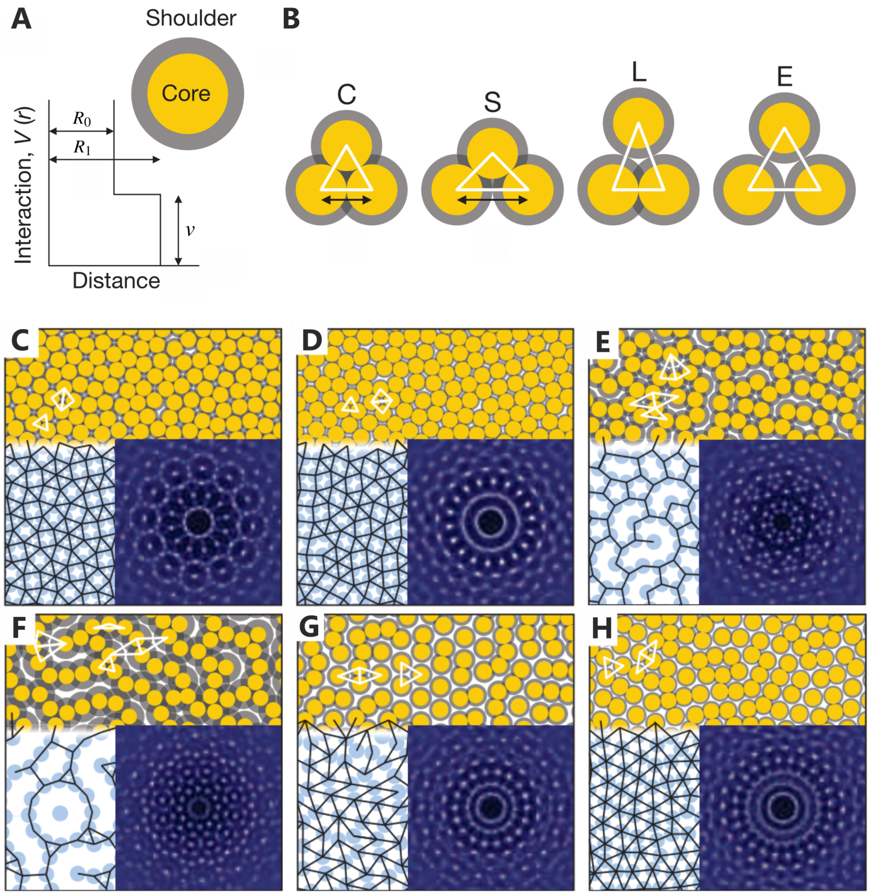

Fig. 2.17 **A**) Hard-core/square-shoulder pair interaction. **B**) Local ordering of three HCSS particles: collapsed equilateral (C), short isosceles (S), long isosceles (L), and expanded equilateral triangle (E). **C-H**) Snapshots showing the mosaic nature of two-length scale 2D quasicrystals. The bottom-left parts of the panels are core-only representations and the bottom-right parts of the panels illustrate the rotational symmetries of the quasicrystals. The simulations were done with various parameters such as shoulder-to-core ratio δ, reduced temperature $T_r = kT/v$, and packing fraction η. More details can be found in [11]. **C**) δ = 1.40, T_r = 0.278, η = 0.770, **D**) δ = 1.27, T_r = 0.208, η = 0.780, **E**) δ = 1.60, T_r = 0.133, η = 0.550, **F**) δ = 1.95, T_r = 0.154, η = 0.430, **G**) δ = 1.43, T_r = 0.0885, η = 0.490, **H**) δ = 1.29, T_r = 0.098, η = 0.595. Adapted with permission from [11] Copyright (2014). Springer Nature.

Chapter 3

Synopsis

As explored in previous chapters, the interfacial behaviours of microgels involve very complex physical phenomena and are not yet well comprehended. This lack of understanding, coupled with the vast potential of soft matter across disciplines, has sparked exciting interdisciplinary collaborations. There has been a recent trend towards an *in situ* approach in the field. [29, 101, 146, 165] This chapter aims to provide a concise summary of the main contributions of this thesis to this fascinating, albeit occasionally controversial field. The first section summarises the findings on the synthesis of micron-sized HCSS microgels via precipitation polymerisation, designed for the use of SALS and various microscopic techniques. The second section delves into the outcomes from the LT-SALS measurements using the HCSS microgel as well as a silica particle and a similarly sized conventional microgel without the hard inorganic core. The results of the LT-SALS measurements were compared with the results of both *in* and *ex situ* microscopic imaging of the corresponding monolayers. The *in* and *ex situ* comparison revealed a notable difference in the microstructures of the microgel monolayers. The third section expands on the interfacial behaviour of microgel monolayers in the presence of solid substrates during the transfer and drying process. We investigated the drying process of microgel monolayers with three different degrees of "softness" on substrates with distinct surface modifications using various microscopic techniques, such as light and fluorescence microscopy, as well as CLSM. Additionally, through the application of particle tracking and height analysis on the microgel monolayers (microgel thin films), we determined the stage at which the aforementioned structural differences become apparent. This experimental discovery finds support in the results obtained from molecular dynamics simulations.

3.1 Synthesis of micron-sized core-shell microgels and their characterisation

The following section is a revised version of the paper Chapter 4.

HCSS microgels with dimensions reaching the micron regime could serve as a convenient model system for studies of crystallisation kinetics and phase behaviour because their larger sizes can allow for optical investigations using, e.g., simple light microscopy as well as small-angle light scattering (SALS), which are extensively customisable and cost/time efficient in-house methods. Real-time investigations even at highly compressed states, where the microgel shells are deformed, overlap and potentially can interpenetrate, will be facilitated by their slower diffusion as well as by their separately labelable cores with higher refractive index, which enhances the contrast in comparison to classical microgels.

In this work, we present an optimised synthesis protocol that uses one-pot seeded precipitation polymerisation for the preparation of micron-sized HCSS microgels with a controllable shell-to-core size ratio. Others have also reached microgel dimensions on the order of 1 μm via step-wise or continuous feeding of the monomers in the absence of surfactant. [72, 73, 166] A precise control over the shell-to-core size ratio targeting overall dimensions reaching the micrometre regime, however, still seems to be challenging, especially with large cores. [70] The difficulties likely arise from several factors. Firstly, silica cores are typically surface-modified with vinyl groups for covalent bonding with polymer chains. This functionalization impacts their colloidal stability. Secondly, the larger and heavier cores are more affected by gravity. Additionally, as polymerisation progresses, higher oligomer/polymer concentrations may result in depletion-induced flocculation. [167] The proposed protocol facilitates surfactant-free precipitation polymerisation in the low total solid content regime, using an overhead stirrer (under efficient stirring). As shown in Figure 3.1A, compared to the protocol frequently used to prepare smaller HCSS microgels with a surfactant (often sodium dodecyl sulfate) in relatively high total solid contents (green line), the proposed protocol demonstrated visibly efficient shell growth (blue line). Note that the microgels are labelled using the notation C_xS_y-z, where x represents the silica core diameter as determined by TEM and y corresponds to the shell-to-core size ratio (defined as D_h measured at 20 °C divided by the diameter of the silica core measured by TEM) and z is the crosslinker density. For example, a microgel system with a 245 nm core with a shell-to-core size ratio of 2.9 with a crosslinker density of 5 mol.% is labelled as $C_{245}S_{2.9}$-5. The shell growth of all microgels can be described by exponential growth as a function of monomer concentration per number of cores (fitted with Gompertz fit, see Figure 3.1B), which enables the prediction of the total microgel sizes for any given feed concentration in the range of core diameter roughly between 200 – 500 *nm*. The blue spheres represent the shell growth as a function of NIPAM concentration per core C_{245}, the black spheres C_{388}, and the red sphere C_{455}.

As proof-of-concept experiments, microgels were subjected to structural investigations using visible wavelength light. Figures 3.1C-E depict a substrate-supported 2D crystal (microgel monolayer) of $C_{455}S_{2.3}$-5 analysed by optical microscopy (Figure 3.1D) and by SALS (Figure 3.1E). Figure 3.1C is a fast Fourier Transform, FFT, of the microscopic image. Figures 3.1F-H show a 3D crystal sample of $C_{340}S_{3.0}$-5 assembled in *N*-methyl-2-pyrrolidone in a rectangular capillary tube. Figure 3.1F is the FFT of the plane of the $C_{340}S_{3.0}$-5 crystal captured by CLSM (Figure 3.1G) and Figure 3.1G shows the diffraction pattern recorded using SALS.

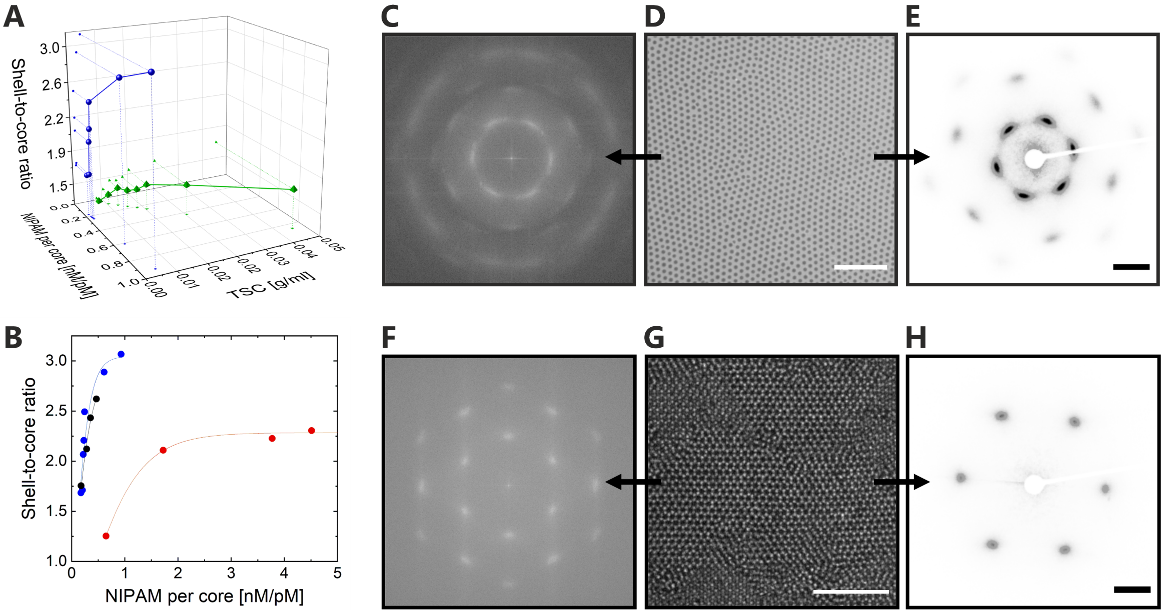

Fig. 3.1 **A**) 3D plot of shell growth on C_{245} depicted as shell-to-core size ratio as a function of the NIPAM concentration per number of cores in nM/pM and total solid content in g/ml. The blue spheres are encapsulation of the shell done via the proposed protocol and the green spheres are according to [17]. **B**) The shell-to-core ratio increases with increasing NIPAM concentration per number of cores in nM/pM. Blue: C_{245}, black: C_{388}, red: C_{455}. **C-E**) $C_{455}S_{2.3}$-5 monolayer analysis by optical light microscopy and SALS. FFT generated (**C**) from the microscopy image (**D**) and the corresponding diffraction pattern recorded by SALS (**E**). The scale bars correspond to 10 μm and 20 *mm*, respectively. **F-H**) 3D crystal assembled from $C_{340}S_{3.0}$-5 in a capillary tube, structural analysis by CLSM and SALS. FFT (**F**) generated from the CLSM image of a crystal plane (**G**), approx. 50 μm from the capillary wall) and the corresponding diffraction pattern recorded by SALS (**H**). The scale bars correspond to 10 μm and 20 *mm*, respectively.

3.2 *In situ* vs. *ex situ* investigation

The following section is a revised version of the paper Chapter 5.

As mentioned in the previous chapter, the assemblies of microgel-type systems have been mainly characterised *ex situ*—after the transfer and deposition onto a solid substrate—with atomic force or electron microscopes under the assumption that the microstructures of the monolayers are unaltered during Langmuir-Blodgett deposition. In this work, we highlight the importance of *in situ* approach to characterise the assembly behaviour of microgels at fluid interfaces during the compression. $C_{340}S_{3.0}$-5 was assembled at the air/water interface (*in situ* monolayer) and the monolayer deposition was carried out via Langmuir-Blodgett deposition on a thoroughly cleaned hydrophilic glass substrate (*ex situ* monolayer). The *ex situ* results were compared to the *in situ* results using LT-SALS as well as microscopy.

The summary of these results is illustrated in Figure 3.2.The images in the first row of Figure 3.2 are snapshots of diffraction patterns captured from *in situ* $C_{340}S_{3.0}$-5 monolayer during the compression with increasing surface pressure as indicated by the blue arrow in the middle. The diffraction pattern shifts to higher angles with increasing surface pressure and eventually becomes distinct Bragg peaks, indicating a 6-fold symmetry of the *in situ* monolayer. The images in the second row are the real space microscopic images of the *in situ* monolayer captured by fluorescence microscopy, depicting the long-range order of the microstructure. The ones in the third row are the microstructures of the *ex situ* monolayer captured by light microscopy (the first one in a bright-field and the rest in a dark-field mode for better visibility), which exhibit the isostructural phase transition. And finally, the images in the last row are diffraction patterns captured from the *ex situ* monolayer. The interparticle distances measured from the real-space images and those calculated from the diffraction patterns reveal that the "core-core" distance varies between *in* and *ex situ* monolayers at the same surface pressure. It is important to note that in an experimental context, the term "core-core" contact refers to the centre-to-centre distance between the silica cores plus the incompressible shell length between them. While the interparticle distances obtained from the *in situ* measurements showed a continuous evolution (decrease with increasing surface pressure) until the monolayers buckled, with no clear differentiation between the "shell-shell" and "core-core" distances, the results from the *ex situ* measurements showed the two distinct characteristic length scales within a critical surface pressure range. These clear differences between the *in* and *ex situ* results are in stark contrast with the widely accepted assumption that the microstructure of the monolayer is retained during Langmuir-Blodgett deposition. Additionally, the observation of *in situ* monolayers indicates that there is an influence of the uniaxial compression on the microstructure, while *ex situ* monolayers did not show any preferred order directions. These findings point towards a pronounced drying and/or substrate effect.

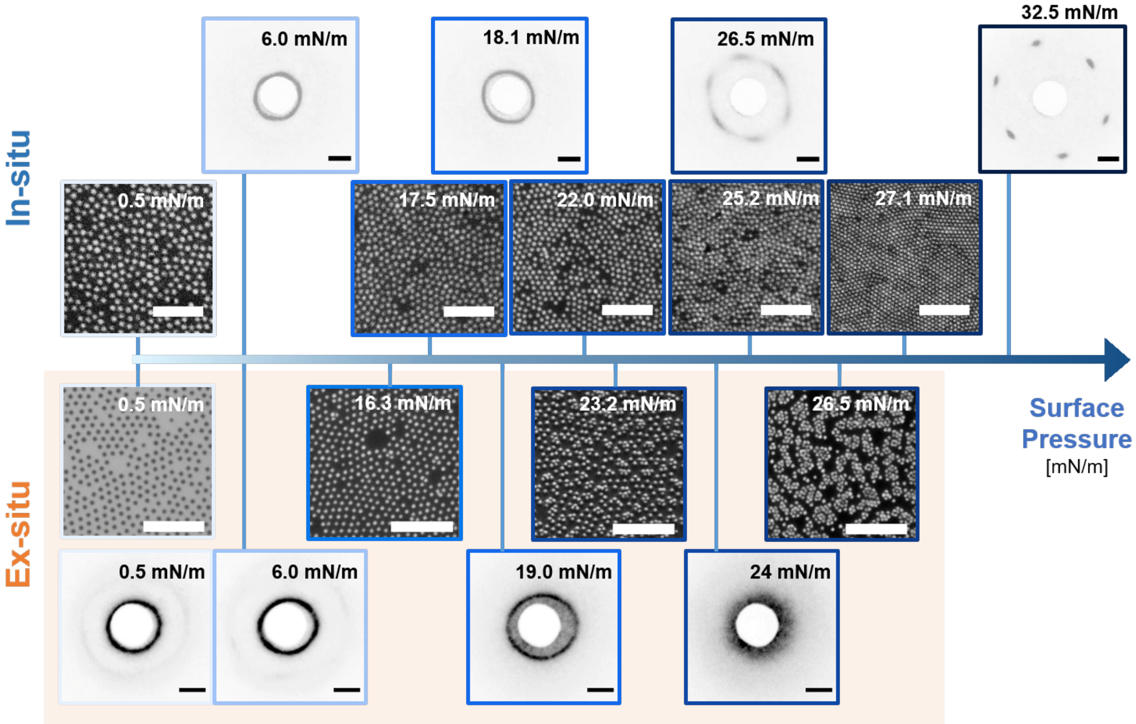

Fig. 3.2 Summary of the *in situ* vs. *ex situ* investigation of the microgel monolayer by SALS and microscopy. The white scale bars correspond to 10 μm and the black bars to 10 mm, respectively.

The potential effect of the drying process and/or the presence of the substrate were briefly verified by subjecting various microgel monolayers to two different drying conditions: “slow” drying at ambient conditions in the open air and “fast” drying using a heat gun, as illustrated in Figure 3.3. Figure 3.3 shows that the “isostructural phase transition” appears only after slow evaporation (blue panels) and not when the drying of the monolayer is done rapidly (red panels), which implies that the microgels have enough time to rearrange when the monolayer is dried slowly under ambient conditions. The results also indicate that the drying effect can be more pronounced when the surface pressure is higher and the core is larger, which could be due to the acting immersion capillary force (see Figures 2.13B and G) during the drying of the microgel monolayers. Note however that there are other parameters that could influence how microgels behave at the interfaces during the transfer and the drying process such as the presence of different types of fluid phases (e.g., oil/water interfaces), size and morphology of microgels, and surface properties of the substrates. One must therefore be cautious when interpreting *ex situ* microstructures of microgel or similar systems. Furthermore, the anisotropic collapse of the microgels was not observed for any of the microgels investigated in this work.

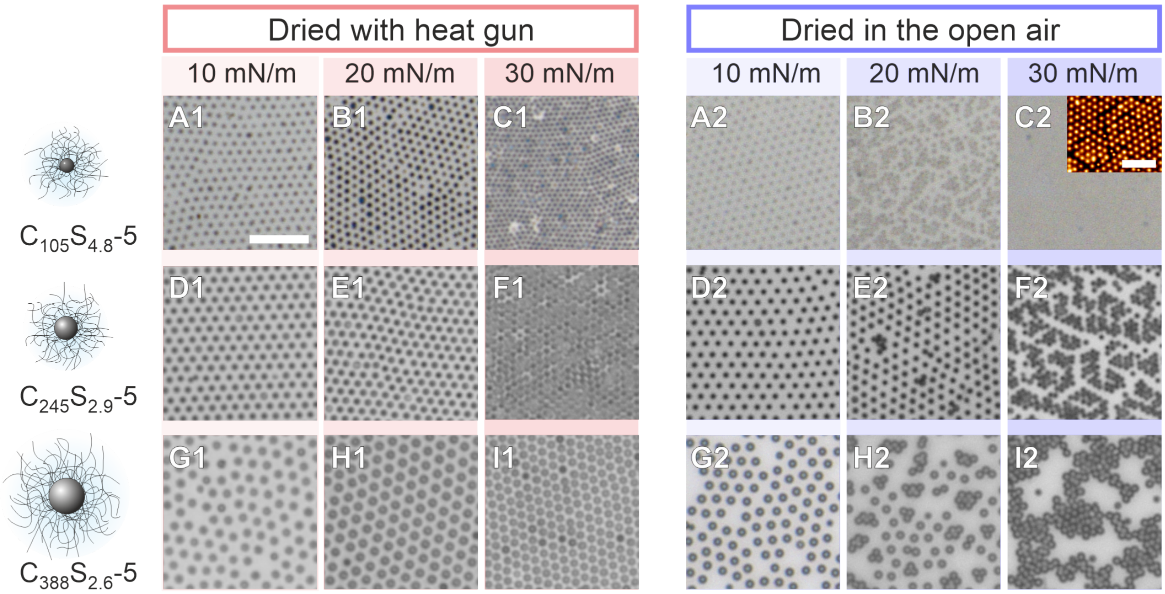

Fig. 3.3 Influence of drying conditions of HCSS microgel monolayers transferred to solid substrates at different surface pressures of 10 mN/m, 20 mN/m, and 30 mN/m. Left red panel: "Fast" drying using a heat gun. Right panel: "Slow" drying against air at ambient conditions for microgels $C_{105}S_{4.8}$-5, $C_{245}S_{2.9}$-5, and $C_{388}S_{2.6}$-5. The scale bar in (**A1**) corresponds to 5 μm. The inset in (**C2**) is an AFM image of the corresponding monolayer. The scale bar corresponds to 2 μm.

3.3 Drying of soft colloidal film

The following section is a revised version of the paper Chapter 6.

In this section, we confirm our findings in the previous section and delve into what really happens when the microgel monolayers dry using CS microgels of comparable size with different crosslinker densities. We hypothesised that the drying dynamics of such monolayers involve an intricate interplay among various factors, including microgel-to-substrate adhesion, immersion capillary forces, and the free energy associated with interface formation. We adjusted these parameters by functionalizing the solid surface, tuning the amount of crosslinker during microgel synthesis, and varying the compression degrees of microgel monolayers. *In situ* observation of the drying microgel monolayers was performed with various microscopic techniques such as light, fluorescence, and confocal microscopy by transferring the microgel monolayers at the air/water interface on to a solid substrate via rapid Langmuir-Blodgett deposition at constant surface pressure.

When such soft colloids are adsorbed at a fluid/liquid interface, they often deform the interface due to their wetting properties. Unlike their hard counterparts, however, soft colloids themselves also undergo structural changes due to their deformable and elastic nature, which competes against interfacial tension. Figure 3.4 depicts microscopic images of $C_{437}S_{2.6}$-1.0 (A), $C_{437}S_{2.3}$-2.5 (B), and $C_{437}S_{2.4}$-7.5 at the air/water interface (C) and their corresponding monolayers ($D_{\text{c-c}} \approx 840$ nm) drying on hydrophilic (A1-C1) and hydrophobic substrates (A2-C2). In general, CS microgels with lower elasticity exhibit enhanced preservation of the assembled structure, primarily due to the increased deformability of the polymer networks at the interfaces, both laterally and vertically. This deformability occurs because of interfacial tension (air/water interface) and thinning of the water film during drying, respectively. Consequently, this leads to larger contact area and thus stronger adhesion to the substrate and, in turn, reduced mobility throughout the drying process. Moreover, microgel-to-substrate adhesion is stronger on hydrophobic substrates, as the interaction between the amphiphilic PNIPAM and the hydrophobic surface is energetically more favourable compared to the interaction between water and the hydrophobic surface. The results are supported by the molecular dynamics simulation.

We quantified the phenomena by identifying the critical height, H^* – the onset of XY displacement of the microgels during the drying via particle tracking. The height profiles of the drying monolayers were traced by their apparent colours, which stem from thin film interference. The resulting height profiles of drying CS microgels shows that H^* values are higher on hydrophilic substrates compared to hydrophobic substrates for all CS microgels. This observation further supports stronger adhesion between microgels and hydrophobic substrates, resulting in more pronounced deformation at the liquid/solid interface and limited mobility during drying. Additionally, the difference in elasticity among CS microgels is also evident in the H^* values: CS microgel films with higher crosslinker density exhibit higher H^* values. The high elasticity of the polymer network appears to resist the thinning of the film, which could also result in a relatively smaller contact area with the substrate and, consequently, lower microgel-to-substrate adhesion and higher mobility during drying.

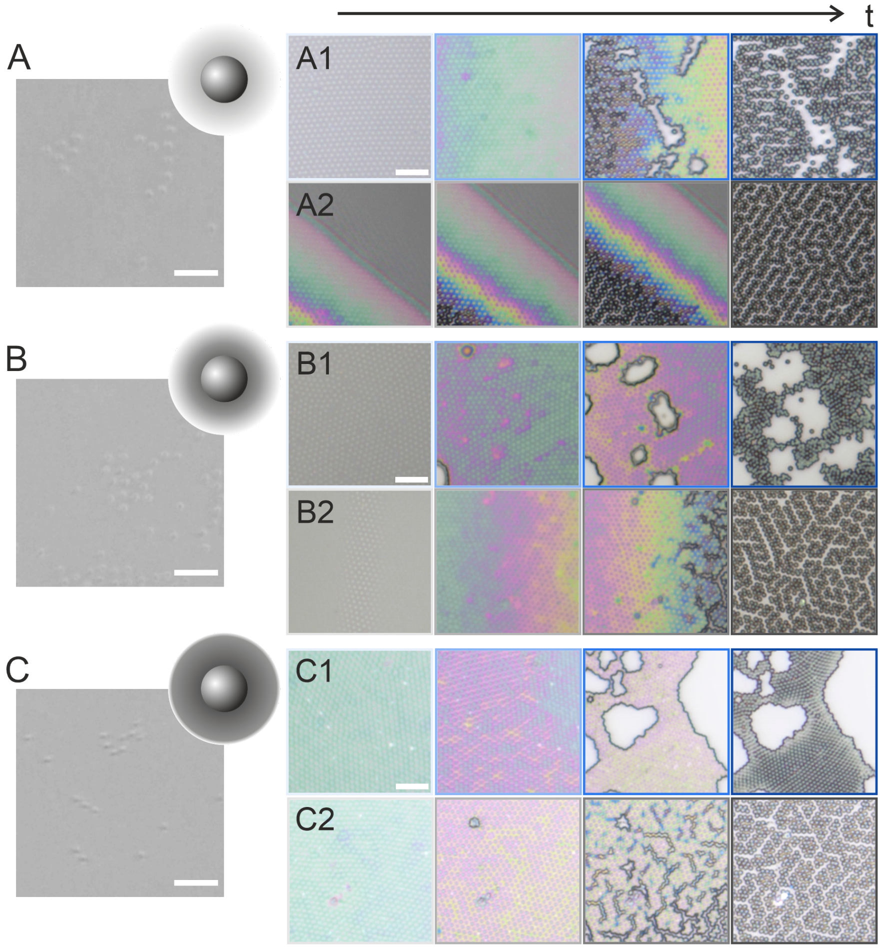

Fig. 3.4 $C_{437}S_{2.6}$-1.0 (A), $C_{437}S_{2.3}$-2.5 (B) and $C_{437}S_{2.4}$-7.5 (C) microgels at the air/water interface, showing different "softness" of the polymer networks due to the different crosslinker densities. Snapshots of video microscopy of $C_{437}S_{2.6}$-1.0 (A1-2), $C_{437}S_{2.3}$-2.5 (B1-2) and $C_{437}S_{2.4}$-7.5 microgel films (C1-2) at comparable $D_{\text{c-c}}$ ($\approx$ 840 nm) transferred onto hydrophilic (A1-C1) and hydrophobic substrates (A2-C2). t denotes the time. The scale bar corresponds to 5 μm.

Chapter 4

Micron-sized silica-PNIPAM core-shell microgels with tunable shell-to-core ratio

Keumkyung Kuk[a], Lukas Gregel[a], Vahan Abgarjan[a], Caspar Croonenbrock[a], Sebastian Hänsch[b], and Matthias Karg[a*]

[a]Institut für Physikalische Chemie I: Kolloide und Nanooptik, Heinrich-Heine-Universität Düsseldorf, Universitätsstr. 1, 40225 Düsseldorf, Germany
[b]Center for Advanced Imaging, Heinrich Heine University Düsseldorf, Universitätsstraße 1, 40225 Düsseldorf, Germany.

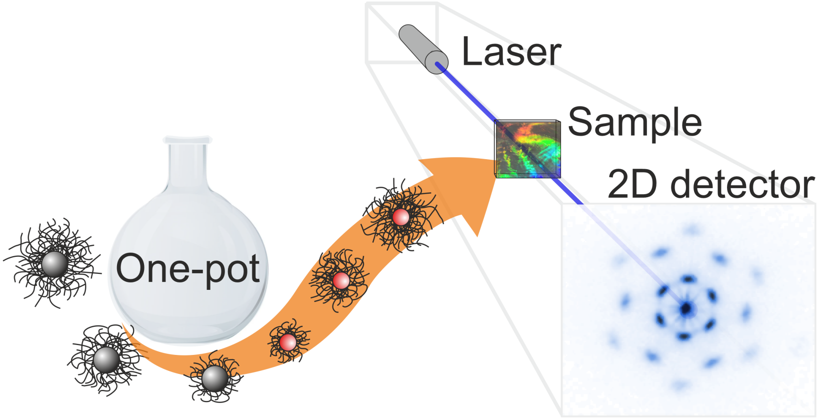

KEYWORDS: Micron-sized core-shell microgels; seeded precipitation polymerization; one-pot synthesis; small-angle light scattering; confocal laser scanning microscopy

Note that this section is written in American English.

4.1 Abstract

Micron-sized hard core-soft shell hybrid microgels are promising model systems for studies of soft matter as they enable in-situ optical investigations and their structures/morphologies can be engineered with a great variety. Yet, protocols that yield micron-sized core-shell microgels with a tailorable shell-to-core size ratio are rarely available. In this work, we report on the one-pot synthesis protocol for micron-sized silica-poly(*N*-isopropylacrylamide) core-shell microgels that has excellent control over the shell-to-core ratio. Small-angle light scattering and microscopy of 2- and 3-dimensional assemblies of the synthesized microgels confirm that the produced micro-gels are monodisperse and suitable for optical investigation even at high packing fractions.

4.2 Introduction

Microgels are colloid-like deformable soft objects that have interior structures resembling gel swollen by a solvent in which they are dispersed. [168, 169] They belong to a unique class of material because they exhibit both solid- and liquid-like behavior and have the capability to respond to external stimuli, e.g., temperature, [170] pH, and ionic strength. [171] These properties can be tuned by engineering the morphologies, [64] composition, [155] porosity, and elasticity of the microgels. [172] Due to their tailorable stimuli sensitivity, high colloidal stability, and a broad range of possibilities for various functionalization, the past decades have seen a steadily increasing interest in microgels in applications such as bio-medicine, photonic and process technology as well as in fundamental researches across disciplines. [168] Among others, inorganic core-polymeric shell microgels, also known as hard core-soft shell microgels, have received significant attention as a soft colloidal model system because of their hybrid properties, [173, 174] fine-tunable interparticle distance [175] and their potential to be assembled into surprisingly complex microstructures despite of their isotropic shape. [13, 160]

In general, there are two approaches to prepare such core-shell (CS) microgels: “graft from” and “graft to” approaches. [25, 26] In the “graft from” approach, the polymer chains grow from the core surface, allowing precise control over the shell thickness [160] with a certain limit. On the other hand, in the “graft to” approach, pre-formed polymer chains/gels are anchored/adsorbed to the core surface. A good example is the free radical precipitation polymerization, which is by far the most widely used synthesis technique that can offer a broader size range as well as various post-modification of polymeric shell morphologies and composition via semi-batch and/or seeded precipitation polymerization methods. [65, 176, 177] The post-modification could also be used for the overgrowth of the shell, increasing the overall dimension of the CS microgels thus the shell-to-core size ratio (δ). CS microgels with dimensions close to the micron regime were synthesized via multiple-step addition of monomer in the past. [72, 166] The micron-sized CS microgels could serve as a very convenient model system for their larger sizes—slower diffusion—can enable in-situ optical investigations using, e.g., optical tweezers, simple light microscopy as well as small-angle light scattering (SALS), which are extensively customizable and cost/time efficient in-house methods. However, one-step synthesis for micron-sized CS microgels with tailorable δ has not been reported yet.

In this study, we present a facile and robust one-pot synthesis protocol to prepare micron-sized, monodisperse CS microgels with controllable δ via a surfactant-free seeded precipitation polymerization. We chose silica as the core material because it is generally biocompatible and can be synthesized with great control over size with low polydispersities, not to mention its facile control over its pore sizes and surface properties via simple silanization chemistry. [33, 178] We chose poly(*N*-isopropylacrylamide) (PNIPAM) as the shell material not only because it is one of the most commonly used and well-studied polymers but also because of its thermoresponsive nature around ambient temperature, which could give rise to numerous applications. We have covered core sizes ranging from 245 to 455 nm in diameter with overall hydrodynamic diameter (D_h) of the CS microgels up to approximately 1.2 μm. The swelling capacity of the different samples was studied by temperature-dependent dynamic light scattering (DLS). All prepared colloids show thermoresponsive properties in water due to the lower critical solution temperature (LCST) behavior of PNIPAM. As a proof of concept, the synthesized microgels are assembled into 2D and 3D microstructures. These superstructures were successfully studied by SALS, light microscopy as well as confocal microscopy.

4.3 Results and Discussion

4.3.1 Synthesis and characterization

We used the seeded precipitation polymerization to synthesize CS microgels with differently sized silica cores and thermoresponsive PNIPAM shells of different thicknesses. For such synthesis, silica cores are commonly surface-functionalized with methacrylates to establish covalent bonds to the PNIPAM shell. Especially in the high total solids content (TSC, here defined as the mass of all the suspended and dissolved solids in the sample divided by the total volume of continuous phase—water) regime, this hydrophobic surface modification can hamper colloidal stability during the synthesis, which can lead to mixed species with double/triple cores, high polydispersity or macroscopic aggregates. Previously, Karg et al. reported significantly lower encapsulation rates with increasing size of the silica cores. [70] In that study, silica cores with sizes ranging from 68 nm to 170 nm in diameter were used. In more recent studies, silica cores with a size of 351 nm were successfully encapsulated in PNIPAM shells leading to micron-sized CS microgels ($D_\mathrm{h} \approx 1\ \mu$m) via seeded precipitation polymerization with multiple-step monomer addition for overgrowing of the shell in the presence of surfactant. [71, 166] Others have also reached microgel dimensions on the order of 1 μm via continuous feeding of the monomers in the absence of surfactant. [72] However, precise control over the δ targeting overall dimensions reaching the micrometer regime still seems to be challenging, in particular for one-pot reactions, also known as single batch polymerizations. In this study, we aim to tackle this challenge and propose a simple but robust synthesis route for micron-sized CS microgels that are sufficiently large to be suitable for investigations using light—either in optical microscopy or diffraction. For the preparation of micron-sized CS microgels, we have found that the shell growth is significantly more effective in the lower TSC regime in the absence of surfactant under efficient stirring. Figure 4.1 shows representative transmission electron microscopy (TEM) images for small (245 nm), medium (388 nm), and large (455 nm) silica cores and the corresponding CS microgels with different shell thicknesses synthesized via surfactant-free precipitation polymerization at low TSC (the proposed synthesis protocol, more details can be found in the **Methods** section). All CS microgels are labeled using CxSy, where x represents the silica core diameter as determined from TEM and y corresponds to the shell-to-core size ratio, δ. δ is defined as D_h measured by dynamic light scattering at 20 °C (swollen state) divided by the diameter of the silica core measured by TEM, for example, 245 nm core with δ of 2.9 ($C_{245}S_{2.9}$) and 455 nm core with δ of 2.3 ($C_{455}S_{2.3}$). All δ values were calculated with D_h as acquired and without error propagation, see **Supplementary information** (SI, section 4.6) for more details. The differently sized silica cores in A) - C) possess spherical shape and low dispersity in size. In images D) - I), the lower contrast area on the edge of the silica cores evidently shows that the PNIPAM encapsulation was successful. In particular, for the microgels with the thickest shells (H and I), the shells are clearly visible. Here each silica core is surrounded by a homogeneous PNIPAM shell. For the microgels with thinner shells, the boundary between the higher electron density—rigid cores, and the low electron density polymeric shell is less noticeable but clearly visible at higher magniication. The TEM images with higher magnifications can be found in SI, Figure 4.6. We want to note that the samples are imaged in the dried state and under high vacuum conditions in the TEM. Consequently, the shells are imaged in a collapsed state with a much smaller dimension than in bulk dispersion, when the shells are swollen with water.

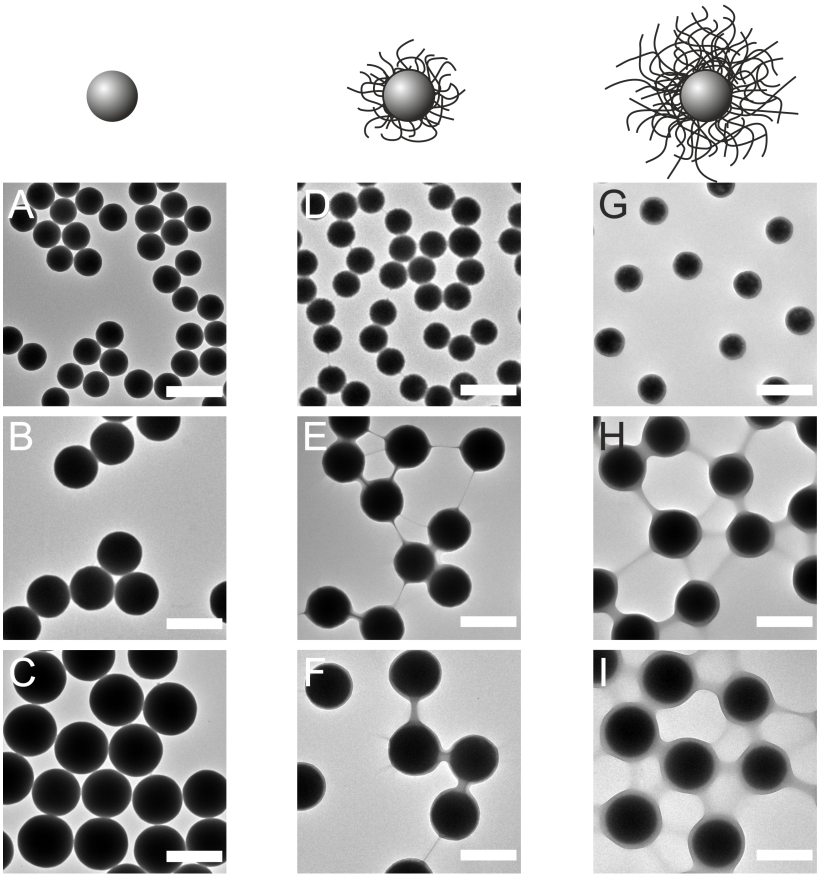

Fig. 4.1 TEM images of CS microgels with variously sized cores: C_{245} (A), C_{388} (B), and C_{455} (C), with thin shells: $C_{245}S_{1.7}$ (D), $C_{388}S_{2.1}$ (E), $C_{455}S_{2.1}$ (F) and with thicker shells: $C_{245}S_{2.9}$ (G), $C_{388}S_{2.6}$ (H), $C_{455}S_{2.3}$ (I). The scale bars correspond to 500 nm.

Figure 4.2A shows a 3D plot of shell growth on C_{245} in terms of δ as a function of NIPAM concentration per number of core and TSC. The blue spheres represent data for CS microgels synthesized without surfactant in the low TSC regime, using an overhead stirrer (the proposed synthesis protocol), while the green tetrahedrons correspond to results from synthesis with surfactant (sodium dodecyl sulfate - SDS, 2 mM) in the high TSC regime, using a magnetic bar for stirring (adapted from [17], labeled as C_xS_y-C_z for Core-Shell-Conventional). More details on the effects of the individual synthesis parameters such as SDS concentration, stirring method, and temperatures on the overall size of the CS microgels can be found in SI. Figure 4.2B shows the shell growth in terms of δ as a function of the NIPAM concentration per number of silica cores for the three different core sizes (see Figure 4.1) performed via the proposed synthesis protocol at low TSC in absence of SDS under more efficient stirring. The results show that the synthesis protocol can also be transferred to significantly larger cores. The shell growth of all CS microgels can be described by an exponential growth as a function of monomer concentration per number of cores (fitted with the Gompertz fit, solid lines). This enables us to predict the total microgel sizes for any given feed concentration, at least in the studied range. At the same time, desired values of δ can be specifically targeted. Figure 4.2C shows the swelling curves of the four selected CS microgels recorded by temperature-dependent DLS: CS microgels with the small core with thin shell $C_{245}S_{1.7}$ (filled blue) and thick shell $C_{245}S_{2.9}$ (empty blue) and the large core with thin shell $C_{455}S_{2.1}$ (filled red) and thick shell $C_{455}S_{2.3}$ (empty red). In all cases, we find the typical volume phase transition (VPT) behavior with a continuous decrease in hydrodynamic diameter with increasing temperature in the vicinity of the volume phase transition temperature (VPTT). Here, we want to note that our larger CS microgels seemed to be under the effect of gravitational settling during the DLS measurements, which could be the reason for their higher polydispersities (or overestimation of polydispersity) compared to the smaller microgels. Although the commonly quoted upper size limit for DLS is around 10 μm, it often is only achievable by increasing the viscosity of the continuous phase or by using capillary DLS. [93, 94] In this study, however, we do not further discuss the matter and report the D_h values as recorded and used for the calculation of δ. The calculated de-swelling ratios (α) of the corresponding CS microgels appear to overlap rather well as depicted in Figure 4.2D. The de-swelling ratios α were calculated as:

$$\alpha = \frac{V_{CS}(T) - V_C}{V_{CS}(10^\circ\mathrm{C}) - V_C} \tag{4.1}$$

where $V_{CS}(T)$ denotes the volume of the total CS microgel measured by DLS at temperature T, V_C the volume of the non-swellable and non-responsive silica cores measured by TEM.

4.3.2 Investigation of 2D assemblies using optical microscopy and SALS

To study 2D assemblies of the CS microgels, we prepared hexagonally ordered monolayers using interface-mediated self-assembly and subsequent transfer to glass substrates. The monolayer assembly is also an effective way to judge their collective behaviors as well as the monodispersity. The samples were transferred to the substrates at surface pressures of approximately 20 mN/m, i.e., at relatively high pressures, where the CS microgels are already in shell-shell contact and squeezed against each other. More information on the sample preparation can be found in the **Methods** section and in SI. We prepared monolayers from CS microgels with the smallest ($C_{245}S_{2.9}$) and largest cores ($C_{455}S_{2.3}$) investigated in this study. Figure 4.3B) and E) show optical light microscopy images of the samples

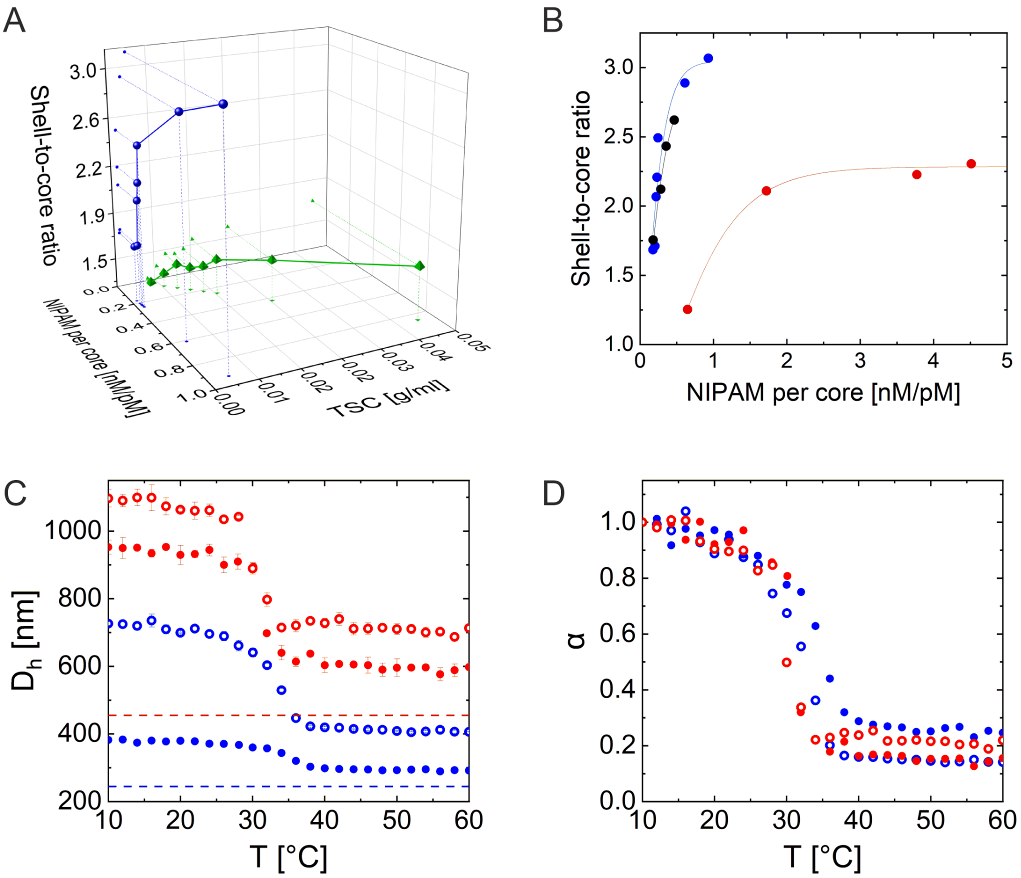

Fig. 4.2 A) 3D plot of shell growth on C_{245} measured by DLS (depicted as shell-to-core ratio) in depend-ence of the NIPAM concentration per number of cores in nM/pM and TSC in g/ml. Blue: C_{245} encapsulation via proposed protocol, green: according to [17] B) Shell growth on differently sized cores illustrated as the shell-to-core ratio in dependence of the NIPAM feed concentration per number of cores in nM/pM. Blue: C_{245}, black: C_{388}, red: C_{455}. The solid lines correspond to the Gompertz fit of the growth. C) Swelling curves of $C_{245}S_{1.7}$ (filled blue), $C_{245}S_{2.9}$ (empty blue), $C_{455}S_{2.1}$ (filled red) and $C_{455}S_{2.3}$ (empty red). The dotted lines represent the diameter of the core measured by TEM. D) Calculated deswelling ratio of corresponding CS microgels from (C).

at 100x magnification. For both samples, this magnification is clearly sufficient to resolve single particles. Furthermore, the hexagonal order becomes evident, which is also reflected by the six-fold symmetric fast Fourier transformations (FFTs) shown in A) and D). While the microscopic images cover areas on the order of 0.01 mm^2, we can probe significantly larger areas over 1 mm^2 when using SALS on the same samples. Figure 4.3C) and F) show the recorded diffraction patterns. In both cases, we again see six-fold symmetries, which are in very good agreement with the FFTs computed from the real space images. Thus, optical microscopy and SALS can deliver complementary information despite the different areas probed. We want to highlight that typically microgel and CS microgel assemblies were studied using scattering techniques based on neutrons and/or X-rays (mostly SANS and SAXS) in the past years and/or by rather high-resolution microscopies such as AFM and scanning electron microscopy (SEM). Being able to use light for the structural investigation offers great possibilities for investigation of micro-structures and phase transitions in real time being independent of large-scale facilities and expensive setups.

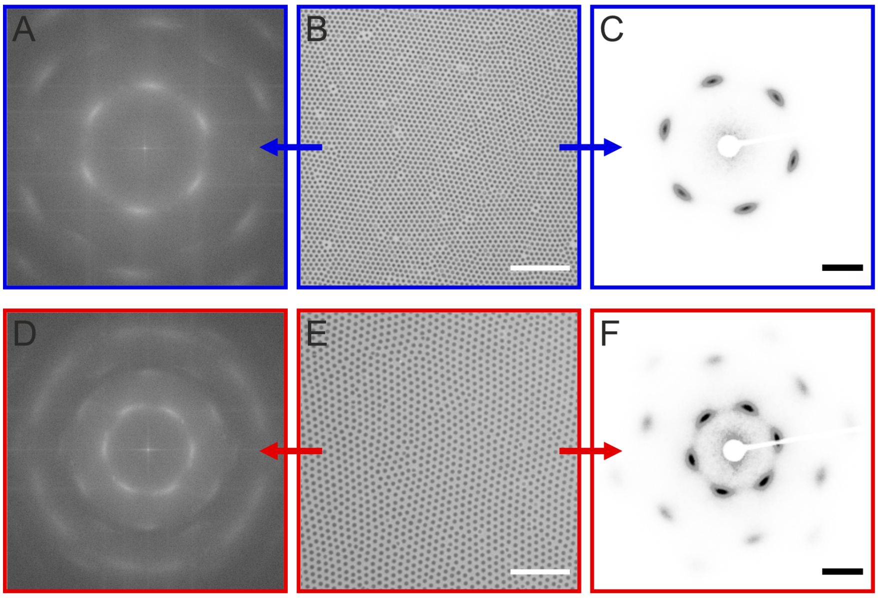

Fig. 4.3 Monolayer analysis by optical light microscopy and SALS. A) FFT generated form the real space microscopy image of a monolayer prepared from $C_{245}S_{2.9}$ taken at a surface pressure of 20 mN/m (B). C) Corresponding diffraction pattern recorded by SALS. D)-E) same set of data as in the top row for a monolayer prepared from $C_{455}S_{2.3}$. Scale bars in B) and E) correspond to 10 μm. Scale bars in C) and F) correspond to 20 mm.

Since the nearest neighbor center-to-center distance, i.e., interparticle distance ($D_{\text{c-c}}$) in 2D assemblies of CS microgels with soft and deformable shells depends on the number of microgels per area, we can cover a broad range of distances with the same batch of microgels simply through adjusting the surface pressure, for example, in a Langmuir trough. Figure

4.4A) shows swelling curves of the two selected CS microgels recorded by temperature-dependent DLS. From these data we can now estimate the possible range of $D_{\text{c-c}}$ and area fraction based on two assumptions: 1) The shell de-formation at the interface leads to a microgel diameter that is by a factor of 1.76 larger than the bulk hydrodynamic diameter [17] and the minimum theoretically possible interparticle distance, i.e., $D_{\text{c-c}}$ in effective core-core contact, corresponds to the D_{h} of collapsed CS microgels at 60°C. 2) The microgels remain perfectly circular and hexagonally arranged throughout the compression and the defects/empty spaces in the monolayer can simply be reflected by a lower area fraction as expressed in equations 4.2 and 4.3.

$$A_P = \pi \cdot \left(\frac{D_{\text{c-c}}}{2}\right)^2 \tag{4.2}$$

$$n_P = \frac{A_f \cdot A_{tot}}{A_P} \tag{4.3}$$

$$D_{\text{c-c}}{}^2 = \frac{4}{\pi} \cdot A_f \cdot \frac{A_{tot}}{n_P} = \frac{4}{\pi} \cdot A_f \cdot \left(\frac{n_P}{A_{tot}}\right)^{-1} \tag{4.4}$$

Here A_P denotes the area occupied by one particle, n_P is the number of particles, A_f is the area fraction, and A_{tot} is the total area. It is clear that $D_{\text{c-c}}{}^2$ scales linear with respect to the area per particle (A_{tot}/n_P), with a slope equal to $4/\pi$ multiplied by A_f. A_f thus can be estimated from the real images. More details on the A_f calculation can be found in SI. Based on these assumptions, we calculated the achievable range of $D_{\text{c-c}}$ as a function of the particle number per unit area (n_P/A) in Figure 4.4B) (solid lines) at maximum A_f (0.91) for the perfect hexagonal arrangement. The diagram also contains measured values of $D_{\text{c-c}}$ (symbols) from monolayers taken from the air/water interface at surface pressures of 10, 20, and 30 mN/m. Note that the measured $D_{\text{c-c}}$ lie slightly lower at the same n_P/A values compared to the calculated $D_{\text{c-c}}$, likely due to occasional non-ideal packing or defects of the monolayers. The estimated area fractions are 0.80 for $\text{C}_{245}\text{S}_{2.9}$ and 0.79 for $\text{C}_{455}\text{S}_{2.3}$, respectively.

4.3.3 Investigation of 3D assemblies using confocal microscopy and SALS

Having shown that our CS microgels are suitable for structural investigations of monolayer samples using light, we now want to turn to 3D assemblies. For this, we chose the sample $\text{C}_{340}\text{S}_{3.0}$ (silica core dyed with rhodamine B, see Table 4.1 and 4.2 in SI for more details)

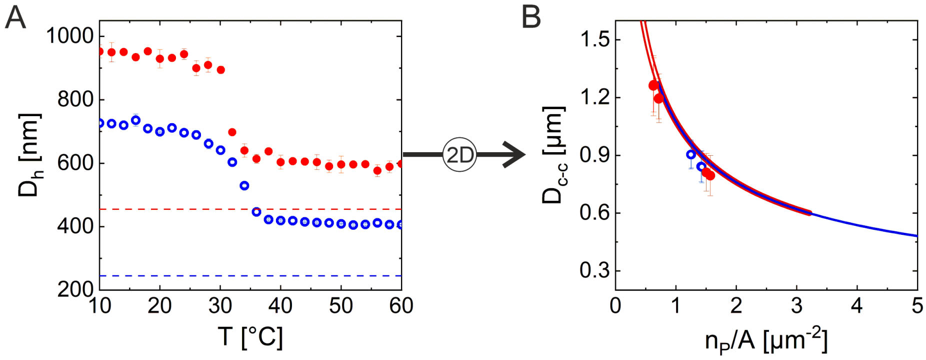

Fig. 4.4 A) Evolution of the hydrodynamic diameter (D_h) for $C_{245}S_{2.9}$ (blue) and $C_{455}S_{2.3}$ (red) as a function of temperature. The dashed, horizontal lines correspond to the respective core diameters measured by TEM. B) Calculated interparticle distance ($D_\text{c-c}$) against the number of particles per unit area (n_P/A) for 2D compression accounting for an area fraction of 0.91 (solid lines, blue: $C_{245}S_{2.9}$, red: $C_{455}S_{2.3}$). Dashed line: with area fraction of 1.6, scatter with error bar: measured data at three different surface pressure (10, 20, and 30 mN/m).

and prepared variously concentrated dispersions using *N*-methyl-2-pyrrolidone (NMP) as solvent. NMP was chosen to reduce the scattering contrast as NMP has a refractive index (1.47) higher than water (1.33) almost matching the index of PNIPAM (1.50) and silica particles (1.45). This way we could reduce multiple scattering which was necessary for the sample investigation by SALS. The samples were sealed in glass capillary tubes, more details can be found in the **Methods** section. Figure 4.5 shows confocal laser scanning microscopy (CLSM) images obtained from $C_{340}S_{3.0}$ NMP dispersions with two different concentrations. The imaging by CLSM revealed that the sample with the lower concentration had an interparticle distance close to the D_h of its building block with periodical spatial arrangements (B), whereas the more concentrated sample showed shorter interparticle distances with amorphous structures (E). Both images were taken in the middle of the glass tube and evidently show different spatial arrangements between the two samples. The FFT of image B) has a six-fold symmetry as shown in A), whereas the FFT of image E) shows a diffraction ring as depicted in D), reflecting the amorphous structure. Figure 4.5C) and D) show the diffraction patterns recorded from the SALS measurement. The recorded diffraction patterns are in very good agreement with the FFTs of the confocal images. Additionally, we have also acquired z-stacks from one glass wall through the sample to the other glass wall, revealing the spatial arrangement throughout the sample. See SI for the avi files. [23]

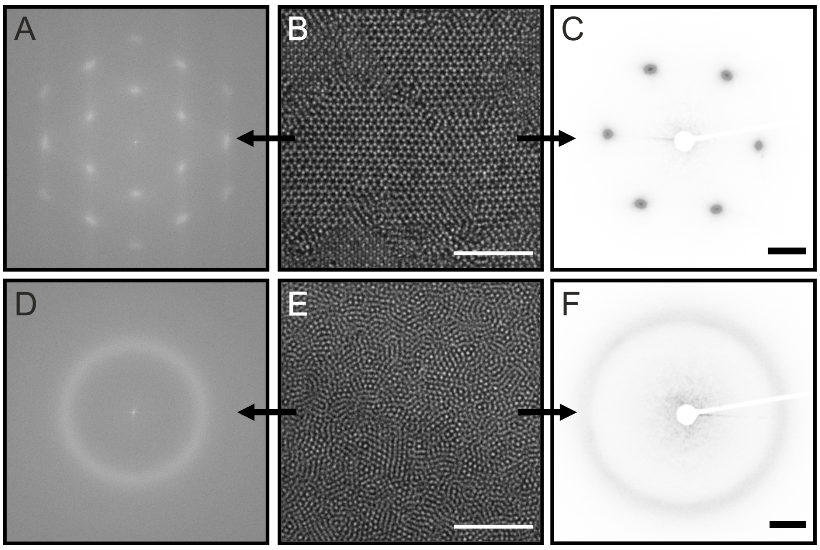

Fig. 4.5 3D colloidal microstructure analysis by CLSM and SALS A) FFT calculated from a CLSM image of $C_{340}S_{3.0}$ dispersed in NMP (naturally sedimented from a dilute sample) taken at approximately 58 μm distance from the glass tube wall (B). C) Corresponding diffraction pattern from SALS performed on the same sample as shown in B). D-F) the same set of data as in the top row for $C_{340}S_{3.0}$ dispersed in NMP at a higher concentration taken at approximately 50 μm distance from the glass tube wall (E). The scale bars correspond to 10 μm in B) and E) and to 20 mm in C) and F).

4.4 Conclusion

In this work, we presented an optimized synthesis protocol that uses the one-pot seeded precipitation polymerization for the preparation of micron-sized core-shell microgels. Silica particles of different sizes were used as rigid cores. The microgel shells were composed of chemically cross-linked poly-*N*-isopropylacrylamide—a thermoresponsive polymer. Due to the single batch nature, our procedure is time and cost-efficient and offers great control over the shell-to-core ratio. As proof-of-concept experiments to demonstrate the suitability of the microgels for structural investigations using visible wavelength light, we studied substrate-supported monolayers as well as 3D samples in capillaries by confocal laser scanning microscopy and small-angle light scattering. The presented core-shell microgels are not only interesting for photonic applications but also allow convenient microstructural analyses using light rather than X-ray/neutron scattering, enabling cost/time-efficient in-house investigations of large sample volumes. The presented systems are ideal model colloids to study, for example, interaction potentials of soft microgels with different morphologies under various conditions, their wetting/de-wetting behaviors, melting and crystallization processes as well as jamming transitions.

4.5 Materials and Methods

4.5.1 Materials

Ethanol (Sigma-Aldrich, 99.8%), ethanol (Heinrich-Heine-University, chemical store, p.a.), tetraethyl orthosilicate (TEOS, Sigma-Aldrich, 98%), ammonium hydroxide solution (NH_3 (aq.), PanReac AppliChem, 30%), ammonium hydroxide solution (NH_3 (aq.), VWR, 25%), hydrogen peroxide solution (H_2O_2, Fisher Chemical, 30 wt.%), *N*-methyl-2-pyrrolidone (NMP, Sigma-Aldrich, 99.5%), rhodamine B isothiocyanate (Sigma-Aldrich, mixed isomers), (3-aminopropyl)trimethoxysilane (Sigma-Aldrich, 97%), 3-(trimethoxysilyl)propyl methacrylate (MPS, Sigma-Aldrich, 98%), *N,N'*-methylenebisacrylamide (BIS, Sigma-Aldrich, 98%), and potassium peroxodisulfate (KPS, Sigma-Aldrich, 99%) were used as received. Water was purified by a Milli-Q system (18.2 $\text{M}\Omega \cdot \text{cm}$) and *N*-isopropylacrylamide (NIPAM, TCI, 97%) by recrystallization from cyclohexane (Fisher Scientific, 99.8%).

4.5.2 Synthesis

Synthesis and surface modification of colloidal silica cores. The silica cores were synthesized via the well-known Stöber procedure [31] and surface-modified with MPS. The details of the synthesis protocol have been reported elsewhere. [17] The synthesis conditions and chemicals used are listed in SI, Table S1. Purification of the synthesized silica particles was done by repeated centrifugation for 2 - 8 min at 5000 - 7000 rcf and re-dispersion in ethanol until the supernatant cleared and the smell of ammonia vanished. The concentrated dispersion was stored in ethanol on a 3D shaker. The TSC of the dispersion in g/ml—the amount of solids remaining after storing in the oven at 80°C for 4 hours—was measured three times and averaged. The particle density was assumed to be 2.1 g/ml for the estimation of particle number concentrations. [32] The size of the silica particles was measured by transmission electron microscopy (TEM). The particles had diameters ranging from 245 to 455 nm with polydispersi-ties on the order of 3.5-9.0%.

Synthesis of silica-PNIPAM CS microgels at fixed temperature. CS microgels were synthesized using seeded precipitation polymerizations with various feed concentrations of NIPAM as monomer and fixed ratios of the cross-linker BIS of 5 mol% (with respect to NIPAM). Eight different silica-PNIPAM CS microgel systems were synthesized following a previously published protocol using an oil bath (silicon oil) heated to 80°C. [17] Additional CS microgels were synthesized with modified protocols described in the following: The corresponding amounts of NIPAM and BIS were dissolved in water in three-neck round-bottom flasks equipped with a reflux condenser and an overhead stirrer (KPG). The mixtures were heated in an oil bath to oil temperatures of 60 - 80°C and purged with argon for one hour while stirring at the speed of 250 - 300 rpm. Then the respective volumes of silica core stock dispersions were added and the mixtures were further purged with nitrogen to remove oxygen. After the target temperature was reached and stabilized, the polymerizations were initiated by the rapid addition of aqueous 0.01 wt.% KPS solution. The polymerizations were allowed to proceed for at least three hours. The final dispersions were hot-filtered through glass wool in a funnel and purified by repeated centrifugation for 2 - 8 min at 5000 - 7000 rcf and re-dispersion in water until the supernatant cleared. The purified dispersions were either freeze-dried for 3D assembly experiments or solvent-exchanged against ethanol via repeated centrifugation and re-dispersion in ethanol for 2D assembly experiments. Further syntheses with variation in SDS and KPS concentrations were done on smaller scales (approx. 6 mL in total volume). All samples synthesized and a detailed list of synthesis con-ditions and amount of materials are provided in the SI, Table 4.2.

Synthesis of silica-PNIPAM CS microgels using a temperature ramp. A well-established temperature-ramp, surfactant-free precipitation polymerization synthesis protocol [65] was modified for the seeded polymerization with silica cores as seeds. The same setup was used as for the synthesis with the fixed temperatures described above. The reaction mixtures were equilibrated at 45°C and purged with argon for one hour while stirring at the speed of 300 rpm. After the initiation, as soon as the appearance of turbidity was visually detected, the temperature was ramped up to 65°C at the average rate of 12.6°C/h. The polymerization was allowed to proceed for three more hours after the final temperature was reached. The microgels were purified as for the protocols at fixed temperatures.

4.5.3 Methods

Monolayer preparation. Prior to the monolayer preparation, the glass substrates (Fisher Scientific, Premium microscope slides 12-544-4) were cut in six smaller pieces (width = 13 mm, length = 25 mm), rinsed with water and placed in a customized glass holder in a beaker for RCA-1 cleaning. The glass slides were treated in $H_2O/NH_4OH/H_2O_2$ solution with a volume ratio of 5:1:1 at 80 ± 5°C for 20 minutes. [179, 180] The monolayer was created by injecting microgel dispersions (in ethanol) directly to the air/water interface in a crystallizing dish filled with water. Three different surface pressures (approximately 10, 20 and 30 mN/m) were targeted to vary the interparticle distance of the transferred monolayer by injecting certain volumes of microgel dispersion. The monolayer was then transferred on to the glass substrate by pushing the glass substrate through the monolayer at the edge of the crystallizing dish and lifting up at the center at a steep angle (70 - 90°) and dried. Further details can be found in the SI.

Preparation of 3D assemblies. Rectangular hollow glass tubes (VitroCom, 5012, path length = 0.1 mm, width = 2 mm) were used to prepare 3D colloidal microstructures in various regimes. The concentrated dispersions were prepared from freeze-dried CS microgels re-dispersed in NMP by repeated overnight shaking (neoLab, 7-0045) and ultrasonication. The resulting viscous dispersion was sucked in to the glass tube by an aspirator. A combination of a 10 - 200 μm micropipette tip and a piece of thin parafilm was used as a flexible connector between the glass tube and the aspirator. When the dispersion occupied about two third of the tube, the open end was sealed by using an oxyhydrogen torch. The tube containing the dispersion was then flipped upside down, cleaned and centrifuged gently. After all dispersions migrated to the sealed bottom, the other end was also sealed by the torch. The prepared samples were vertically stored until no further sedimentation was observed. The dilute samples sedimented and formed strongly iridescent colloidal crystals, whereas concentrated samples did not show any visible changes.

Dynamic light scattering (DLS). The hydrodynamic diameter, D_h, of the CS microgels were determined using a Zetasizer Nano S (Malvern Panalytical). The device is equipped with a HeNe laser (4 mW, 633 nm) along with a temperature-controlled jacket. Measurements were performed at a scattering angle of 173° in the temperature range between 10 and 60°C in steps of 2°C. Three measurements (per temperature and sample) were performed using samples filled in semi-micro PMMA cuvettes (VWR, 634-0678) with 10 minutes of equilibration duration at each temperature. Values of D_h reported are z-average values as obtained from the measurement software. All samples had polydispersities (PDI, polydispersity index) on the order of 5-10% in average for small microgels and 10-30% for micron-sized microgels with standard deviations up to 7%.

Small-angle light scattering (SALS). Diffraction patterns were recorded by a self-built setup. A blue laser (MediaLas, LDM-20-405, 20 mW, 405 nm) was used as a light source and the images were captured in the dark with a CCD camera (Thorlabs, DCU223C-MVL6WA) and a paper screen as a detector. Acquired images were grey scaled and inverted with ImageJ (1.53k, National Insti-tutes of Health, USA) for better visibility. Further details can be found in the SI.

Transmission electron microscopy (TEM). TEM measurements were performed using a JEOL JEM-2100 Plus microscope operated in bright-field mode at 80 kV acceleration voltage. Samples of the silica cores were prepared by applying a drop of an ethanolic particle dispersion on a carbon-coated copper grid (200 mesh, Science Services) and drying at room temperature. Samples of the CS microgels were prepared by transferring the monolayer from the air/water interface onto the copper grids, as described for the monolayer preparation. All images were subsequently processed using ImageJ.

Optical light microscopy. A Nikon Eclipse LV150N equipped with a 100× objective was used to acquire images of the microgel monolayers on the glass substrates. At least two images at different positions were recorded per sample. ImageJ was used to perform fast Fourier transformations (FFT) on the acquired images as well as to find the radial distribution function from the detected particle centers (macro version: 2011-08-22 by Ajay Gopal).

Confocal laser scanning microscopy (CLSM). 3D samples in the glass tubes were imaged using a Zeiss LSM880 Airyscan microscope system (Zeiss Microscopy GmbH), equipped with a Plan-Apochromat 63×/1.4 oil immersion objective lens. The sample tubes were mounted on the stage on a glass slide supported 3D-printed adapter fitting in the object holder of the motorized stage. The silica cores were covalently labeled with Rhodamine B so the samples were imaged using a 561 nm excitation laser and a BP 570-620 + LP 645 emission filter. The acquisition was performed in airyscan super-resolution mode at 1.43 (3D) or 1.52 (2D) µsec pixel dwell time and 4× line averaging. Airyscan alignment of the system was regularly checked during the acquisition process and raw stacks of the full 100 µm range were finally processed by the Zeiss Airyscan processing in 3D standard mode. Additionally, single slice measurements were acquired at the indicated Z-depth in the middle of the glass tubes and processed in 2D standard airyscan mode.

Supporting Information available: Additional synthetic details, methods and instrumentations, more detailed description of monolayer preparation, schematics and other details on SALS setup, TEM images with a higher resolution, a brief discussion on the effect of SDS, KPS, temperature and stirring on CS microgels, fitting area fraction for monolayers (PDF), two videos of acquired z-stacks on 3D samples (AVI), and a 3D model of the multi-reactor holder for small scale synthesis (STL).

Notes: The authors declare no competing financial interest.

Acknowledgements: The authors acknowledge the DFG and the state of NRW for funding the cryo-TEM (INST 208/749-1 FUGG). M.K. acknowledges the German Research Founda-tion (DFG) for funding under grant KA3880/6-1. We also would like to acknowledge the Center for Advanced Imaging (CAi) at Heinrich-Heine-University Düsseldorf (HHU Dusseldorf) for providing access to the Zeiss LSM880 Airyscan system (Ref.No. DFG- INST 208/746-1 FUGG). The authors would like to thank Marco Hildebrandt (HHU Dusseldorf) for the transferred know-how for hollow glass tube handling, Marius Otten (HHU Dusseldorf) for the TEM imaging, and Dr. Virginia Carrasco Fadanelli (HHU Dusseldorf) for the kind introduction to MATLAB.

4.6 Supplementary information

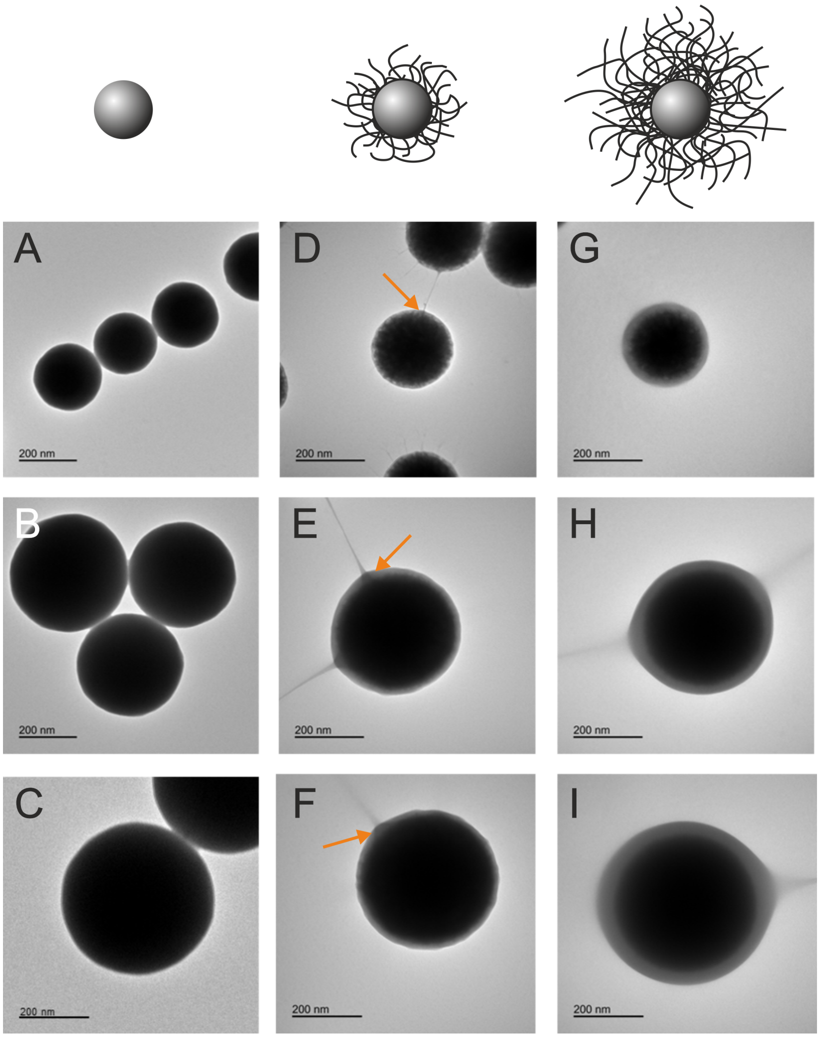

Fig. 4.6 Higher magnification TEM images of CS microgels with variously sized cores: C_{245} (A), C_{388} (B), and C_{455} (C), with thin shells: $C_{245}S_{1.7}$ (D), $C_{388}S_{2.1}$ (E), $C_{455}S_{2.1}$ (F) and with thicker shells: $C_{245}S_{2.9}$ (G), $C_{388}S_{2.6}$ (G), $C_{455}S_{2.3}$ (G).

Influencing parameters in CS microgel synthesis at low TSC. A surfactant, such as SDS, can be used in the synthesis to prevent the aggregation of the cores but it also influences the final size of the CS microgels. For classical microgels, the effect of surfactant is well known: It stabilises the forming primary microgels via charge repulsion thereby driving the systems closer to good-solvent conditions. The smaller the primary microgels are, the higher is the final number of microgels, which consequently leads to smaller final size of microgels for a given amount of monomer in the system and higher homogeneity. [62, 63, 181] For CS microgels synthesized via seeded precipitation polymerization, however, the number of seeds is predetermined by the added number of cores and thus the same mechanism cannot hold. We found that CS microgels nonetheless follow the same trend as the classical microgels. Figure 4.7A shows swelling curves of CS microgels synthesized with various concentrations of SDS: 0 mM ($C_{433}S_{2.0}$-0, light green), 0.2 mM ($C_{433}S_{1.8}$-SDS0.2, green), 2 mM ($C_{433}S_{1.6}$-SDS2, dark green). Apart from the influence of SDS, we also investigated the role of the initiator (KPS) concentration and polymerization temperature, which has a similar influence on the size of the CS microgels, as shown in Figure 4.7B. Light blue represents 0.01 wt.% KPS ($C_{433}S_{2.0}$-0), blue 0.03 wt.% ($C_{433}S_{1.7}$-KPS0.03), dark blue 0.05 wt.% ($C_{433}S_{1.6}$-KPS0.05), respectively.

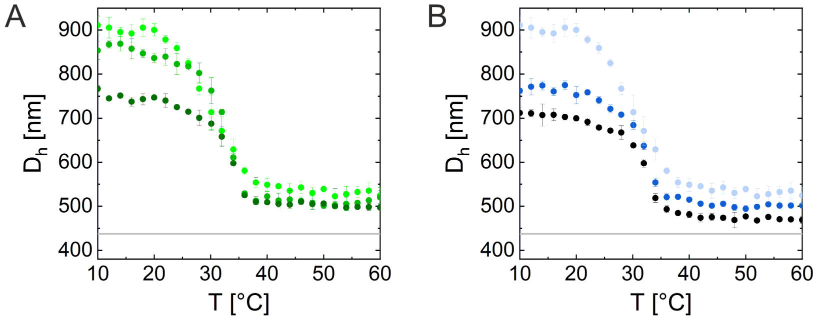

Fig. 4.7 A) Swelling curves of CS microgels synthesized with increasing SDS concentrations (light green: 0 mM, green: 0.2 mM, dark green: 2 mM, grey line: core diameter by TEM. B) with increasing KPS concentrations (light blue: 0.01 wt.%, blue: 0.03 wt.%, dark blue: 0.05 wt.%, grey line: core diameter by TEM.

The synthesis temperature is proven to exert even stronger influence on size of the microgels. For instance, over 2.5 μm sized classical microgels can be synthesized via precipitation polymerization with temperature ramp, usually at a lower temperature range. [65, 66] In contrast to the effect of surfactant or initiator, the lower temperature reduces the number of primary microgels and therefore leads to the larger microgels. Figure 4.8A shows the influence of the synthesis temperature on the size of the CS microgels. The empty pink stars, filled light red circles, red squares, and dark red triangles represent the CS microgels synthesized with a temperature ramp (45 - 65°C, $C_{340}S_{3.4}$-T45-65) and at fixed temperatures of 60°C ($C_{340}S_{3.0}$-T60), 70°C ($C_{340}S_{2.9}$-T70), and 80°C ($C_{340}S_{2.7}$-T80), respectively. As for the classical microgels, the size of CS microgels also increased with decreasing synthesis temperature. The CS microgel synthesized via temperature ramping, meanwhile, did not show a strong increase in size and exhibited considerably higher polydispersity when assembled in 2D. Additionally, more efficient stirring also seemed to improve the efficiency in PNIPAM shell growth. Figure 4.8B shows PNIPAM shell encapsulation at low TSC (0.005 g/ml) at three different synthesis temperatures: 60°C, 70°C, 80°C. The filled symbols represent the syntheses stirred with a KPG stirrer with a moon-shaped stirrer blade, and the empty symbols with the egg-shaped magnetic stirring bar. The synthesis at 60°C stirred with egg-shaped magnetic stirring bar stopped stirring an hour after the initiation due to macroscopic aggregates around the stirring bar.

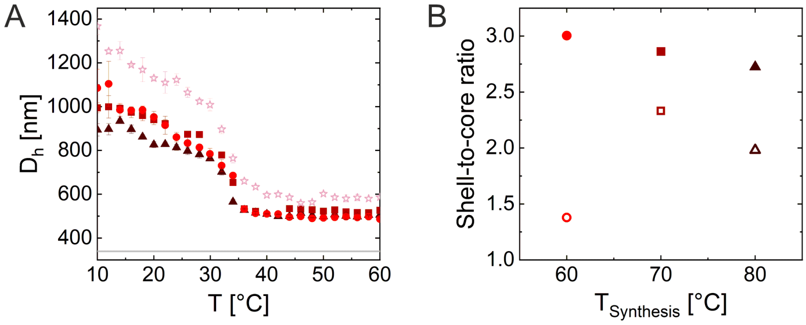

Fig. 4.8 A) Swelling curves of CS microgels synthesized with decreasing temperature (empty light pink stars: 45 - 65°C filled light red circles: 60°C, red squares: 70°C, dark red triangles: 80°C, grey line: core diameter by TEM. B) Comparison between stirring by egg-shaped magnetic stirring bar (empty scatters) and KPG stirrer with moon-shaped stirrer blades (filled scatters) at various temperature: 60°C (circles), 70°C (squares), 80°C (triangles).

Monolayer preparation. Monolayers of different CS microgels were prepared using interface-mediated self-assembly using a crystallizing dish filled with water. The air/water interface was cleaned by using an aspirator with a tip, as illustrated in Figure 4.9A. Surface pressures were measured using a Wilhelmy film balance. The CS microgels were deposited directly at the air/water interface by injection from ethanolic dispersion using a micropipette. Three different surface pressures (10, 20 and 30 mN/m) were targeted to vary the interparticle distance of the transferred monolayer. The injection was done slowly at a shallow angle while the tip was gently touching the interface until the target surface pressure was reached (Figure 4.9B). The prepared glass slide was pushed into the water bulk phase through the monolayer close to the edge of the crystallizing dish and moved to the centre. The monolayer was taken from the centre at a steep angle and immediately heat-treated by a heat gun from the bottom side while horizontally held until completely dried (Figure 4.9C). The bottom side was then carefully wiped with ethanol-soaked tissue.

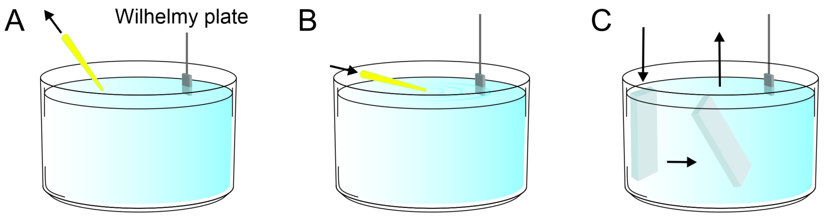

Fig. 4.9 A) Air/water interface cleaning by an aspirator. B) Monolayer deposition with a micropipette at the cleaned air/water interface. C) Monolayer transfer on to the RCA cleaned glass.

Estimation of Area fraction for 2D assembly. Approximately 60,000 particles were counted per sample for the image analysis. The positions of the microgels and number of particles in the probed area (microscopic images) were found using ImageJ and the $D_{\text{c-c}}$ was obtained from the Gaussian fitting of the first peak of the radial distribution function. Figure 4.10 shows the linear relation between $D_{\text{c-c}}{}^2$ and the area per particle (A/P). Note that the estimated A_f is likely to be underestimated due to the fact that the microgels at the edge of the probed area are often not considered in the image analysis.

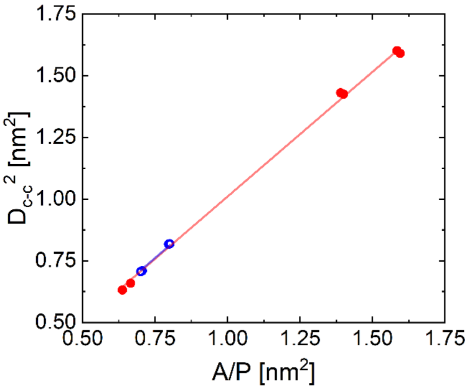

Fig. 4.10 The linear fit for the calculation of A_f from measured data: $C_{245}S_{2.9}$ (empty blue) and $C_{455}S_{2.3}$ (filled red).

Small scale synthesis. 3 - 6 batches were synthesized at a time in 12 ml round bottom glass centrifuge tubes. The tubes were held by a 3D printed holder at around 45°angle, as depicted in Figure 4.11. The reaction mixtures were prepared in stock, purged with argon for 1 hour and heated up to 80°C while stirring with a winged magnetic stirrer bar. The polymerization was allowed to proceed for at least 3 hours with a constant flow of argon. The dispersions were purified by repeated centrifugation and re-dispersion in water without filtration.

Small-angle light scattering (SALS). Laser diffraction patterns were recorded by a self-built setup, see Figure 2.6. A blue laser (MediaLas, LDM-20-405, 20 mW, 405 nm) was

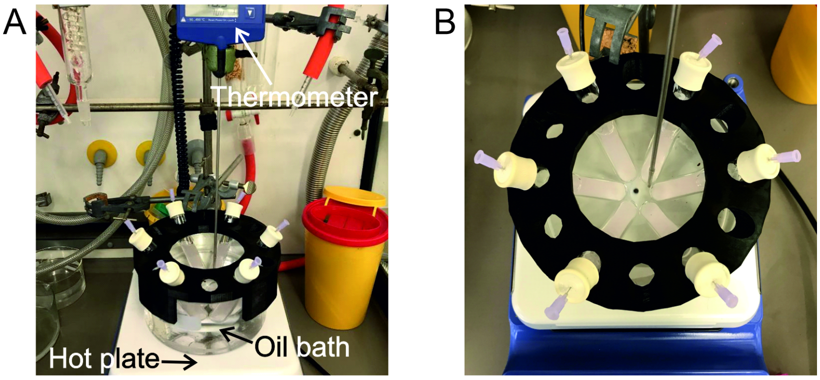

Fig. 4.11 Small scale synthesis setup. A) Side view of the setup. B) Top view.

used as a light source. The diameter of the laser was reduced to 1.19 mm by a beam expander, which consists of two lenses, a pinhole and an iris (Thorlabs). The sample was placed on 3D printed holders. A CCD camera (Thorlabs, DCU223C-MVL6WA) and a paper screen as a detector, the images were captured in dark. The primary beam blocked by a 3D printed beam stop during measurement. The pixel-to-mm ratio was calibrated by using millimetre paper on the paper screen.

Table 4.1 Chemicals used for the synthesis of silica cores presented in this paper.

	Temp. [°C]	Initial			Added		D_{TEM} [nm]	Dye
		Ethanol [ml]	Water [ml]	Ammonia aq. [ml]	TEOS [ml]	Ethanol [ml]		
C_{245}	40	100	0	10	5	0	245±18	-
C_{388}	50	57	0	19	15	30	388±35	-
C_{455}	60	90	0	20	30	10	455±27	-
C_{340}	60	80	5	25	10	30	340±20	Rhodamine B
C_{433}	50	56	16	28	10	40	433±15	Rhodamine B

The silica particles were synthesised via Stöber procedure. All particles were MPS modified according to the previously published protocol [17] and C_{340} and C_{433} were dyed with Rhodamine B.

Table 4.2 Chemicals and synthesis parameters used for the preparation of CS microgels presented in this work.

	Core				**Core - shell**						
Name	**D_{TEM} [nm]**	**TSC [g/ml]**	**added [ml]**	**H_2O [ml]**	**NIPAM [g]**	**BIS [g]**	**KPS [g]**	**SDS [g]**	**Temp. [°C]**	**δ 20°C**	**δ 50°C**
$^*C_{433}S_{1.99}$-0	437	0.53	0.02	6	0.020	0.001	0.001	0.0000	80	1.99	0.00
$^*C_{433}S_{1.75}$-$SDS_{0.2}$	437	0.53	0.02	6	0.020	0.001	0.001	0.0003	80	1.75	1.10
$^*C_{433}S_{1.63}$-SDS_{2}	437	0.53	0.02	6	0.020	0.001	0.001	0.0035	80	1.63	1.11
$^*C_{433}S_{1.73}$-$KPS_{0.03}$	437	0.53	0.02	6	0.020	0.001	0.002	0.0000	80	1.99	1.13
$^*C_{433}S_{1.61}$-$KPS_{0.05}$	437	0.53	0.02	6	0.020	0.001	0.003	0.0000	80	1.83	1.18
$C_{340}S_{2.72}$-T_{80}	340	0.11	2.00	255	1.002	0.072	0.026	0.0000	80	2.72	1.50
$C_{340}S_{2.86}$-T_{70}	340	0.11	2.00	255	1.002	0.072	0.026	0.0000	70	2.86	1.54
$C_{340}S_{3.00}$-T_{60}	340	0.11	2.00	255	1.000	0.072	0.026	0.0000	60	3.00	1.52
$C_{340}S_{3.36}$-T_{45-65}	340	0.11	1.00	255	1.000	0.071	0.026	0.0000	45-65	3.36	1.85
$C_{245}S_{1.26}$-C1	245	0.10	2.00	55	0.101	0.008	0.006	0.0319	80	1.26	1.17
$C_{245}S_{1.35}$-C2	245	0.10	2.00	55	0.202	0.015	0.006	0.0314	80	1.35	1.19
$C_{245}S_{1.44}$-C3	245	0.10	2.00	55	0.302	0.022	0.006	0.0316	80	1.44	1.21
$C_{245}S_{1.43}$-C4	245	0.10	2.00	55	0.401	0.029	0.006	0.0314	80	1.43	1.14
$C_{245}S_{1.45}$-C5	245	0.10	2.00	55	0.500	0.036	0.006	0.0314	80	1.45	1.15
$C_{245}S_{1.52}$-C6	245	0.10	2.00	55	0.600	0.043	0.006	0.0315	80	1.52	1.19
$C_{245}S_{1.57}$-C7	245	0.10	2.00	55	1.000	0.072	0.006	0.0320	80	1.57	1.23
$C_{245}S_{1.85}$-C8	245	0.10	2.00	55	2.001	0.144	0.006	0.0322	80	1.85	1.39
$C_{245}S_{1.68}$	245	0.11	0.33	125	0.076	0.006	0.013	0.0000	70	1.68	1.23
$C_{245}S_{1.71}$	245	0.11	0.33	125	0.088	0.006	0.013	0.0000	70	1.71	1.25
$C_{245}S_{2.07}$	245	0.11	0.33	125	0.095	0.006	0.013	0.0000	70	2.07	1.32
$C_{245}S_{2.21}$	245	0.11	0.33	125	0.100	0.007	0.013	0.0000	70	2.21	1.30
$C_{245}S_{2.49}$	245	0.11	0.33	125	0.106	0.008	0.013	0.0000	70	2.49	1.37
$C_{245}S_{2.89}$	245	0.11	0.33	125	0.265	0.018	0.013	0.0000	70	2.89	1.74
$C_{245}S_{3.07}$	245	0.11	0.33	125	0.404	0.027	0.013	0.0000	70	3.07	1.82
$C_{388}S_{1.75}$	388	0.37	1.00	125	0.192	0.014	0.013	0.0000	70	1.75	1.26
$C_{388}S_{2.12}$	388	0.37	1.00	125	0.304	0.021	0.013	0.0000	70	2.12	1.38
$C_{388}S_{2.43}$	388	0.37	1.00	125	0.383	0.027	0.013	0.0000	70	2.43	1.42
$C_{388}S_{2.62}$	388	0.37	1.00	125	0.502	0.035	0.013	0.0000	70	2.62	1.51
$C_{455}S_{1.25}$	455	0.20	0.36	125	0.086	0.006	0.013	0.0000	70	1.25	1.11
$C_{455}S_{2.11}$	455	0.20	0.36	125	0.229	0.016	0.013	0.0000	70	2.11	1.32
$C_{455}S_{2.23}$	455	0.20	0.36	125	0.502	0.037	0.013	0.0000	70	2.23	1.46
$C_{455}S_{2.30}$	455	0.20	0.36	125	0.601	0.041	0.013	0.0000	70	2.30	1.45
$C_{455}S_{2.25}$	455	0.20	0.36	125	0.751	0.052	0.013	0.0000	70	2.25	1.51
$C_{455}S_{2.34}$	455	0.20	0.36	125	1.003	0.070	0.013	0.0000	70	2.34	1.41

*Small scale synthesis.

Chapter 5

Compression of colloidal monolayers at liquid interfaces: in- vs. ex-situ investigation

Keumkyung Kuk[a], Vahan Abgarjan[a], Lukas Gregel[a], Yichu Zhou[a], Virginia Carrasco-Fadanelli[b], Ivo Buttinoni[b], and Matthias Karg[a*]

[a]Institut für Physikalische Chemie I: Kolloide und Nanooptik, Heinrich-Heine-Universität Düsseldorf, Universitätsstr. 1, 40225 Düsseldorf, Germany
[b]Institut für Experimentelle Physik der kondensierten Materie, Heinrich-Heine-Universität Düsseldorf, Universitätsstr. 1, 40225 Düsseldorf, Germany

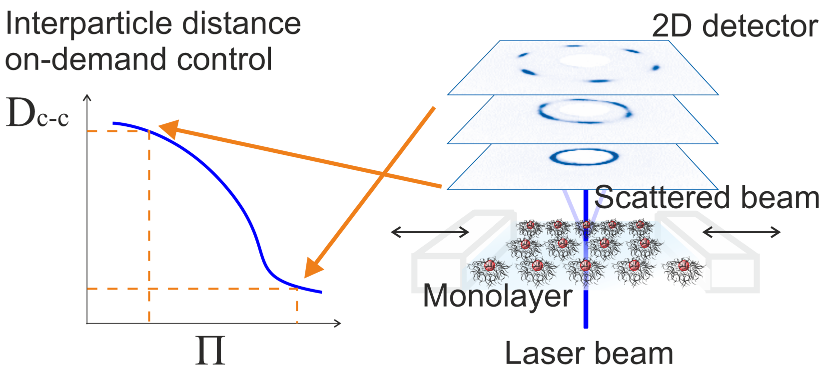

KEYWORDS: Colloidal monolayers; Core-shell microgels; Liquid Interfaces; Langmuir trough compression; Small-angle light scattering; Isostructural phase transition.

Note that this section is written in American English.

5.1 Abstract

The assembly of colloidal particles at liquid/liquid or air/liquid interfaces is a versatile procedure to create microstructured monolayers and study their behavior under compression. When combined with soft and deformable particles such as microgels, compression is used to tune not only the interparticle distance but also the underlying microstructure of the monolayer. So far, the great majority of studies on microgel-laden interfaces is conducted *ex situ* after transfer to solid substrates, for example, via Langmuir-Blodgett deposition. This type of analysis relies on the stringent assumption that the microstructure is conserved during transfer and subsequent drying. In this work, we couple a Langmuir trough to a custom-built small-angle light scattering setup to monitor colloidal monolayers *in situ* during compression. By comparing the results with *ex situ* and *in situ* microscopy measurements, we conclude that Langmuir-Blodgett deposition can alter the structural properties of the colloidal monolayers significantly.

5.2 Introduction

Colloidal monolayers at liquid interfaces, namely, micro- and nanoparticle-laden liquid interfaces, are widely used in fundamental and applied studies. Colloidal particles can self-assemble, in fact, in two-dimensional materials with properties (e.g., photonic or electronic) similar to those of atomic structures. However, unlike atomic counterparts, the colloidal building blocks can be engineered in terms of the chemical composition, [182–185] shape, [16, 185–187] and morphology, [154, 166] in order to tailor the assembly behavior and spatial arrangement. One of the methods for preparing colloidal monolayers is via confining particles at the flat interfacial plane between two immiscible fluids (e.g., an air/water or oil/water interface). [188] This approach offers great advantages not only for studies of gas-liquid-solid phase transitions as the particle concentration (i.e., the number of particles per unit area) can be tuned *in situ* by means of lateral barriers, [17, 150] but also for scalable fabrications for both planar and curved surfaces with areas ranging from cm^2 up to m^2 scales. [41, 42, 189] In the latter approach, the microstructures at the liquid interface are transferred and deposited on solid surfaces (Langmuir-Blodgett deposition) to obtain dried colloidal films, e.g., for coating or photonic applications. [36, 190–193] In contrast to assemblies of rigid spheres, soft colloidal objects like microgels and nanogels [168] can be deformed, for example, under external compression giving access to richer phase diagrams and complex superstructures. [53, 145]

The structural properties of colloid-laden interfaces are typically extracted from microscopy images by detecting the centers of mass of the colloidal units. [104, 194–197] This “particle-tracking” method quickly becomes time-consuming and computationally demanding in the presence of many particles. Even more importantly, it can be only applied above the Abbe diffraction limit. For example, due to the mostly small sizes synthesized to date, assemblies of coreless and core-shell microgels have been mainly characterized *ex situ*—by looking at dried samples with atomic force or electron microscopes—under the assumption that the structure is unaltered during Langmuir-Blodgett deposition. [71, 72, 150, 151, 160, 166, 162, 164] Only recently, *in situ* observation of local regions of the particle-laden interface was achieved via atomic force microscopy. [101] In this study, we propose an *in situ* method—a Langmuir trough combined with small-angle light scattering (LT-SALS)—to characterize colloidal monolayers at the air/water interface. To demonstrate its versatility, colloids of different morphologies were monitored during compression: silica particles (rigid spheres), poly-*N*-isopropylacrylamide (PNIPAM) microgels (soft spheres) and silica-PNIPAM core-shell microgels (hard core-soft shell spheres). The focus of our study, however, lies on the assembly of the core-shell (CS) microgel system. We first present the results from an *ex situ* structural analysis using Langmuir-Blodgett deposition. Then, we compare these results to an *in situ* analysis performed using LT-SALS as well as fluorescence microscopy. Our results indicate that there are severe structural differences between the microstructures of CS microgels at air/water interfaces and after transfer to a solid substrate. These drying effects are in stark contrast with the widely accepted assumption that the interfacial structure is replicated during Langmuir-Blodgett deposition for microgel type building blocks. We discuss analogies and differences with existing works as well as possible reasons for the observed structural changes during drying.

5.3 Results

5.3.1 Core-shell microgels

We prepared monolayers of CS microgels at an air/water interface in a Langmuir trough and studied their structure under compression using *ex situ* light microscopy (Method 1), *in situ* fluorescence microscopy (Method 2) and *in situ* small-angle light scattering (Method 3).

CS microgels possess two relevant length scales: the diameter of the incompressible core (here, silica) and the thickness of the soft, deformable shell (here, PNIPAM). In bulk, these length scales simply define the boundaries of the interparticle interactions. When the microgels are confined and spread at the air/water (or oil/water) interface, the situation becomes more complex because the shells laterally deform at the interface leading to changes in shell morphology and shape, and consequently the total diameter, D_i(interfacial diameter), which is larger than the bulk hydrodynamic diameter, D_h. [17, 145, 198, 199] Generally, there are three different scenarios for the spatial arrangement of CS microgels at air/water or oil/water interfaces: At very low number of particles per unit area (n_p/A), i.e., for near-zero surface pressures, the CS microgels mostly stay apart in an unordered, fluid-like state. In the second regime, as the n_p/A increases, the microgel shells start to touch (shell-shell contact) more frequently. Finally, in the third regime, the shells are squeezed and/or interpenetrated (core-core contact) until the critical point, where the monolayer buckles, breaks and/or is pushed into the subphase (water). Theoretically, if the energy difference between the partially and fully overlapped shells is small enough, energy minimization is achieved by the overlap of shells in some directions at the cost of other neighboring shells, [9, 11, 13] leading to a change in the symmetry of the monolayer. In experimental studies, however, such a symmetry change of the microgel monolayer with increasing n_p/A has only been partially observed. [161] In most cases, core-shell structured microgels [17, 72, 160] and coreless microgels [56, 141, 151, 152, 162, 164] seem to undergo an "isostructural solid-solid phase transition" characterized by microgels in hexagonal arrangement with "shell-shell" contact versus a denser phase, also of hexagonal order, where the microgels are in "core-core" contact. [149, 150] Note that the interparticle distance in "core-core" contact includes the diameter of the core, D_c, as well as the compressed microgel shell. The discrepancies between numerical and experimental studies concerning the phase behavior at interfaces have been ascribed to capillary forces and a highly nonlinear mechanical response of the polymer chains (i.e., the PNIPAM corona) under compression [150, 160, 161, 164] In the following, we report the same "isostructural solid-solid phase transition" only during *ex situ* characterization (Method 1) of monolayers of micron-sized CS microgels. Remarkably, this phenomenon is not observed during *in situ* experiments (Methods 2 and 3).

5.3.2 Method 1 (*ex situ* microscopy)

The *ex situ* microstructural analysis relies on the microscopic investigation of the colloidal monolayer upon transfer from the liquid interface to a solid substrate followed by drying. This leads to dry, substrate-supported colloidal monolayers. When the transfer to the solid substrate is done continuously while the monolayer is compressed in the Langmuir trough, the monolayer position on the substrate can be linked to the corresponding surface pressure at the liquid interface. [149, 150] In this study, the CS microgel system used for the *in situ* and *ex situ* comparison has a core diameter D_c = 340 ± 20 nm and a total hydrodynamic diameter D_h = 920 ± 18 nm (see Synthesis Section for more details). Figure 5.1A shows the measured compression isotherm during the Langmuir-Blodgett deposition along with the corresponding microscopy images. Note that we use a linear color coding from light blue to black linked with low to high surface pressure (Π) throughout this article. From the mid Π regime (16.3 mN/m and higher), the images were taken in dark field mode to facilitate image analysis. The monolayer images at lower Π were recorded in bright field mode. With increasing compression, i.e., decreasing available area, A, the surface pressure increases continuously. In the low Π regime, the CS microgels are not homogeneously distributed over the accessible area (see microscopy images) but rather show hexagonal arrangements with shell-shell contacts and some voids among numerous crystalline domains. This indicates the presence of attractive interparticle interactions despite the large interparticle distances, in agreement with previously reported results from *in situ* and *ex situ* analysis of CS microgel monolayers. [17, 149, 166] As Π increases, the crystalline domains grow while the voids close. In the high Π regime, we observe the formation of CS microgel clusters in "core-core" contact. The critical surface pressure of this "isostructural solid-solid phase transition" is around 16 - 18 mN/m for the presented CS microgel, which can be also identified both in the splitting of the first peak of the radial distribution functions (RDFs, Figure 5.1B) and in the diffraction patterns of the dried monolayers (Figure 5.2). Although the *ex situ* "core-core" distance should lie within the detection limit of our current SALS setup, the microstructures produce diffuse scattering patterns (Figure 5.1C and D), instead of revealing two distinctive length scales. This is due to the fact that the "isostructural phase transitions" is only locally isostructural, i.e., the monolayers, on mm^2 scale, do not show a defined symmetry. The transition is more pronounced for higher values of Π, i.e., the diffuse contribution to the scattering patterns increases with increasing Π. For low to medium values of Π, the RDFs are characterized by the first peak corresponding to the interparticle distance, i.e., center-to-center distance from *ex situ* image $D_{\text{c-c}}^{\text{im,ex}}$, whereas for high Π above the critical value (e.g., 23.2 mN/m), the peak splits near D_{h}. Figure 5.1C reflects the appearance of these two distinct interparticle distances, as the value of $D_{\text{c-c}}^{\text{im,ex}}$ approaches D_{h}. In summary, the *ex situ* analysis reveals that the CS microgel monolayers undergo an "isostructural solid-solid phase transition" upon compression, in agreement with previous studies. [72, 161]

5.3.3 Method 2 (*in situ* microscopy)

in situ analysis of the monolayers of CS microgels at the air/water interface under compression was done by combining fluorescence microscopy with a microscopy trough, i.e., a trough equipped with an optical window. Figure 5.3A shows representative microscopy images taken at various values of Π during compression. At near zero Π, we observe clusters of CS microgels due to attractive (capillary) interparticle interactions (see Figure 5.11 in Supporting

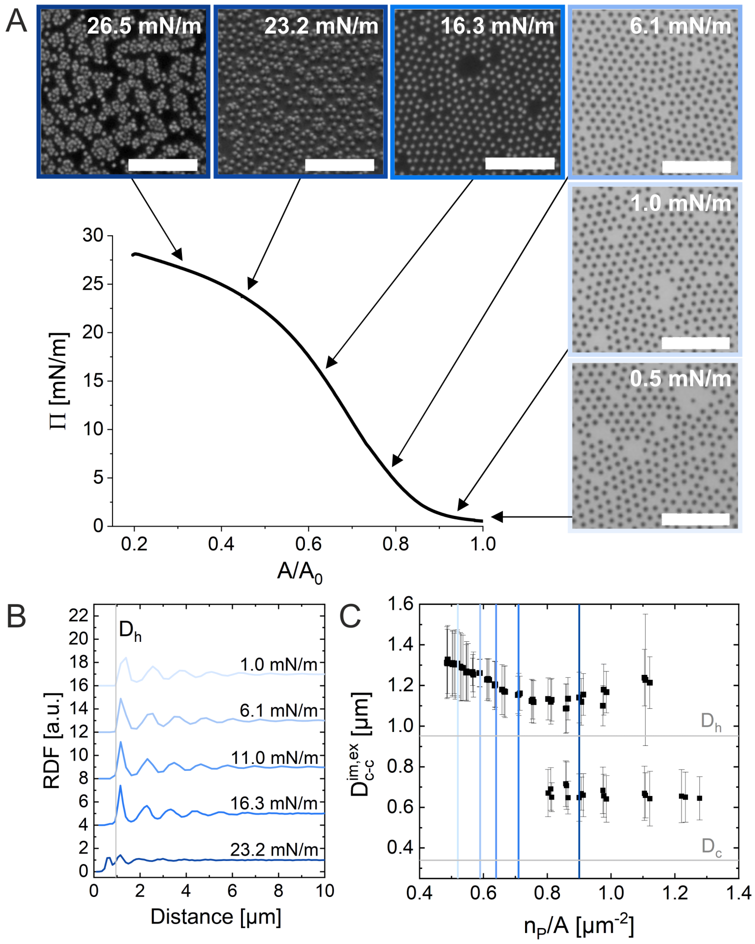

Fig. 5.1 A) Compression isotherm of the CS microgels at the air/water interface: Surface pressure (Π) as a function of normalized area (A/A_0). The inserted images correspond to optical microscopy images taken *ex situ* using the substrate-supported monolayers obtained from simultaneous Langmuir-Blodgett deposition (dried monolayer). The black arrows indicate the corresponding Π for each microscopy image. The scale bars correspond to 10 µm. B) Radial distribution functions (RDF) for different Π. C) Interparticle distance $D_{\text{c-c}}^{\text{im,ex}}$ as a function of the number of particles per unit area (n_{p}/A). The colored vertical reference lines indicate the corresponding Π from B).

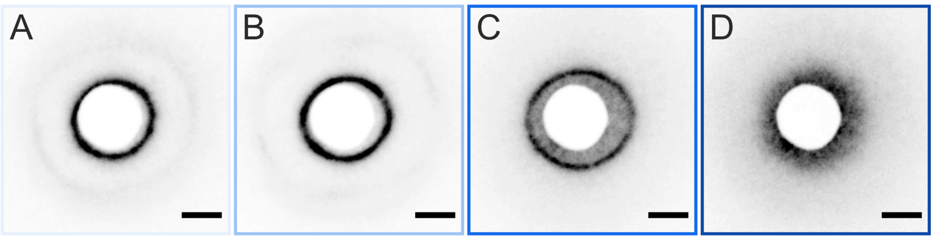

Fig. 5.2 Scattering pattern of the dried CS microgel monolayer. The corresponding surface pressures (Π) are A) 0.5 mN/m, B) 6 mN/m, C) 19 mN/m, and D) 24 mN/m. The scale bars correspond to 10 mm.

Information (SI)), as also reported for other large (D_h > 700 nm) coreless and CS microgels. [71, 105, 149, 166] In the regime of low Π, we observe similar microstructures as for the *ex situ* analysis after transfer to a substrate. However, the degree of order appears to be lower at the air/water interface. For medium-to-high values of Π, the comparison with *ex situ* results reveals striking differences: unlike $D_\text{c-c}^\text{im,ex}$, the *in situ* interparticle distances, $D_\text{c-c}^\text{im,in}$, continuously decrease and the degrees of order increase with increasing Π. An "isostructural solid-solid phase transition" is not observed, in contrast to the assembly behavior reported for other similarly-sized coreless and CS microgels. [72, 149] This becomes even more evident when looking at selected RDFs as presented in Figure 5.3B. The first double peak in the RDFs for higher Π is not present. Furthermore, the higher degree of order is reflected by the large number of distinct peaks in the RDF computed for the highest Π. In contrast to the high Π regime studied in the *ex situ* analysis, the monolayer possesses pronounced long-range order when studied at the air/water interface. Figure 5.3C shows the evolution of $D_\text{c-c}^\text{im,in}$ with n_p/A in direct comparison with the values obtained from *ex situ* analysis $D_\text{c-c}^\text{im,ex}$, shadowed area). The data clearly shows a continuous decrease in $D_\text{c-c}^\text{im,in}$ with increasing n_p/A, indicating a continuous compression of the soft colloidal monolayer. Starting from approximately 1.5 μm, $D_\text{c-c}^\text{im,in}$ decreases linearly with increasing n_p/A until a pronounced deviation from the *ex situ* results appears when approaching distances that are close to D_h. The final values, at high compression, are slightly larger than half the initial $D_\text{c-c}^\text{im,in}$ and lie—until the monolayer buckles—in between the two distinct distances (shell-shell and "core-core") determined by the *ex situ* analysis. To summarize, the *in situ* measurements using fluorescence microscopy revealed significant differences not only in the microstructure of the monolayer but also in terms of the evolution of the interparticle distance and a noticeable shift in n_p/A for corresponding Π (see Figure 5.12A and B in SI for more details). For the studied CS microgels, these findings point towards a pronounced drying and/or substrate effect upon transfer by Langmuir-Blodgett deposition, as typically performed for such *ex situ* microstructure analysis. We address this further when discussing the LT-SALS experiments in the next section.

5.3.4 Method 3 (*in situ* LT-SALS)

We realized a custom-built setup that combines a Langmuir trough featuring a transparent glass window in the trough bottom (microscopy trough) with a custom-built SALS setup that allows to measure diffraction patterns at high frame rates (up to 30 frames per second, in our case). The details of this setup are provided in the Experimental Section and in the SI. Furthermore, the SI addresses the achievable q-range for various laser wavelength highlighting the versatility of the presented LT-SALS method. Figure 5.4 shows the compression isotherm

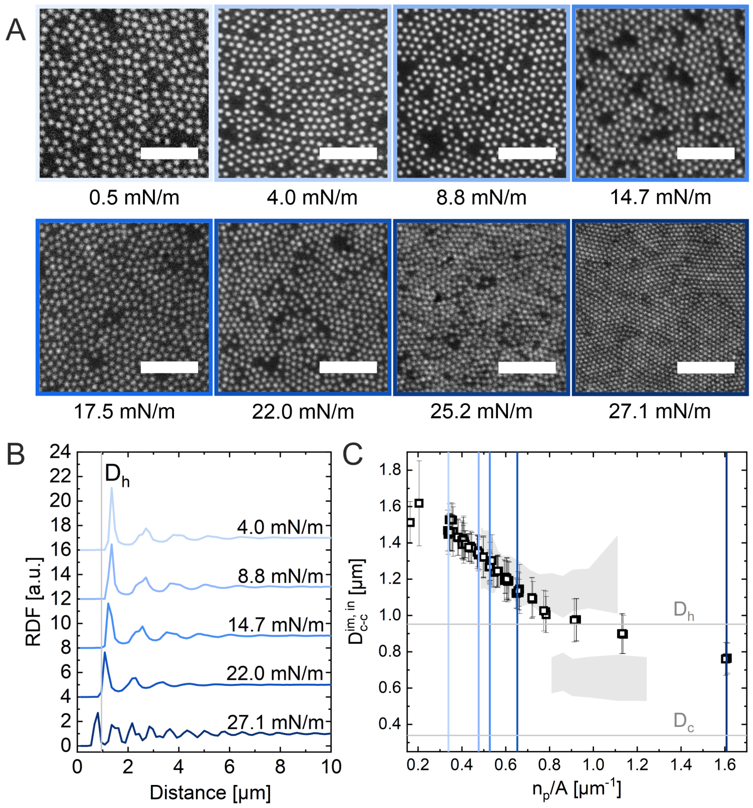

Fig. 5.3 A) Fluorescence microscopy images of the CS microgel monolayer at the air/water interface at various surface pressures (Π). The scale bars correspond to 10 μm. B) Radial distribution functions (RDF) for different Π. C) Interparticle distance $D_{\text{c-c}}^{\text{im,in}}$ as a function of the number of particles per unit area (n_{p}/A). The colored vertical reference lines indicate the corresponding Π from B) and the shadowed area represents the data points from the *ex situ* measurements (Figure 5.1C).

along with six selected frames recorded by LT-SALS. The selected frames are correlated to the respective values of Π in the isotherm as indicated by the black arrows. The full video recorded during the compression can be found in the SI. [30] The diffraction patterns evolve from a small to a larger ring in a continuous manner in the low to mid Π regime, indicating a continuous decrease in $D_{\text{c-c}}$ in real space. This continuous evolution of the diffraction ring goes on well beyond the critical value of Π where the structural transition was observed in the *ex situ* analysis (Method 1 and Figure 5.2). This is in agreement with the results from *in situ* analysis using fluorescence microscopy (Method 2). As the compression proceeds approaching the high Π regime, the diffraction pattern moves more rapidly away from the center revealing diffraction peaks with six-fold symmetry. After the maximum Π is passed at approximately 34 mN/m, the scattering intensity around the beam stop increases abruptly, indicating the collapse of the monolayer (data are not shown; the collapse can be seen in the Supplementary Video, SI).

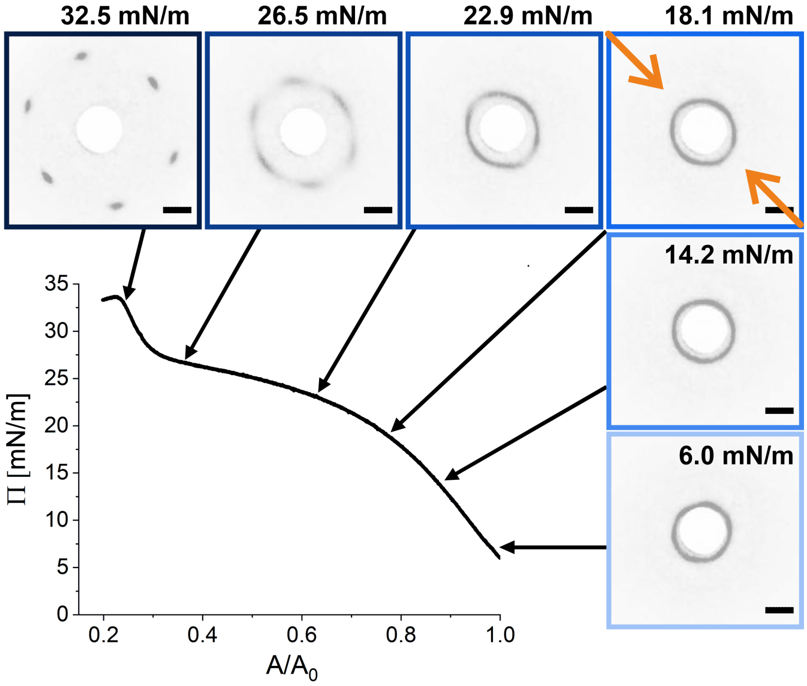

Fig. 5.4 Compression isotherm of the monolayer of CS microgels at the air/water interface: Surface pressure (Π) as a function of the normalized area (A/A_0). The images are diffraction patterns of selected frames from a video recorded during the compression (see also SI). The black arrows indicate the corresponding Π at time of measurement. The greyscale of the images was inverted for better visibility. The orange arrows indicate the compression direction and the white circle at the center is the beam stop. The scale bars correspond to 10 mm (real space dimensions on the detection screen).

Figure 5.5A shows the radial averaging of the intensity of the SALS images as a function of the magnitude of the scattering vector q. The resulting scattering profiles show single peaks that correspond to the structure factor of the monolayer. With increasing compression, the position of the structure factor maximum shifts to larger q, i.e., smaller real space distances, and its intensity drops significantly in the high Π regime. The oval shape of the diffraction pattern in the mid Π regime and the increasing full width at half maxima (FWHM) in radial averaging provide interesting insight into the order of the uniaxially compressed monolayer. This, however, is out of the scope of this work and thus will not be discussed here. The calculated real space interparticle distance from the position of the structure factor maximum, $D_{\text{c-c}}^{\text{SALS}}$ (see SI for more details), is plotted against Π in Figure 5.5B, which also contains the values of $D_{\text{c-c}}^{\text{im,in}}$ from the *in situ* fluorescence microscopy (Method 2) as shadowed area for direct comparison. The two data sets overlap and demonstrate the continuous decrease in interparticle distance with increasing Π. There is no indication of the "isostructural solid-solid phase transition" as observed in the *ex situ* analysis (Method 1). The increase in degree of order during the compression can be monitored by azimuthal averaging at the respective structure factor maximum as shown in Figure 5.5C. With increasing Π, the azimuthal profiles show a transition from a rather isotropic signal to pronounced Bragg peaks at 60°intervals indicating the hexagonal arrangement of the CS microgels in the monolayer. The FWHMs of all six peaks were averaged (FWHM$_{\text{avg}}$) and plotted against $D_{\text{c-c}}^{\text{SALS}}$ in Figure 5.5D. The FWHM$_{\text{avg}}$ notably lowers before the $D_{\text{c-c}}^{\text{SALS}}$ reaches values similar to D_{h}, which supports the previous observation of increasing order.

In conclusion, the results obtained using the three Methods (*ex situ* microscopy, *in situ* microscopy and *in situ* LT-SALS) are compared in Figure 5.6A. The grey and blue shadowed areas illustrate the calculated interparticle distances from LT-SALS and *in situ* fluorescence microscopy, respectively, whereas the filled squares correspond to the *ex situ* measurements. The graph highlights the conflict between the *ex situ* and *in situ* analysis of our CS microgel monolayers. The continuous evolution of interparticle distance in monolayers at the air/water interface during the continuous compression was also observed for other CS microgels, as illustrated in Figure 6B and 6C, where the interparticle distance (normalized by the core diameter) is plotted as a function of Π for CS microgels with different shell thickness (Figure 5.6B) and overall hydrodynamic diameters ranging from 770 to 1170 nm (Figure 5.6C).

5.3.5 Application of LT-SALS to Other Colloidal Systems

In this section, we would like to briefly emphasize the versatility of LT-SALS by showing data for two additional representative colloidal systems, i.e., silica particles (as an example of rigid spheres) and PNIPAM microgels without rigid cores (as an example of soft spheres).

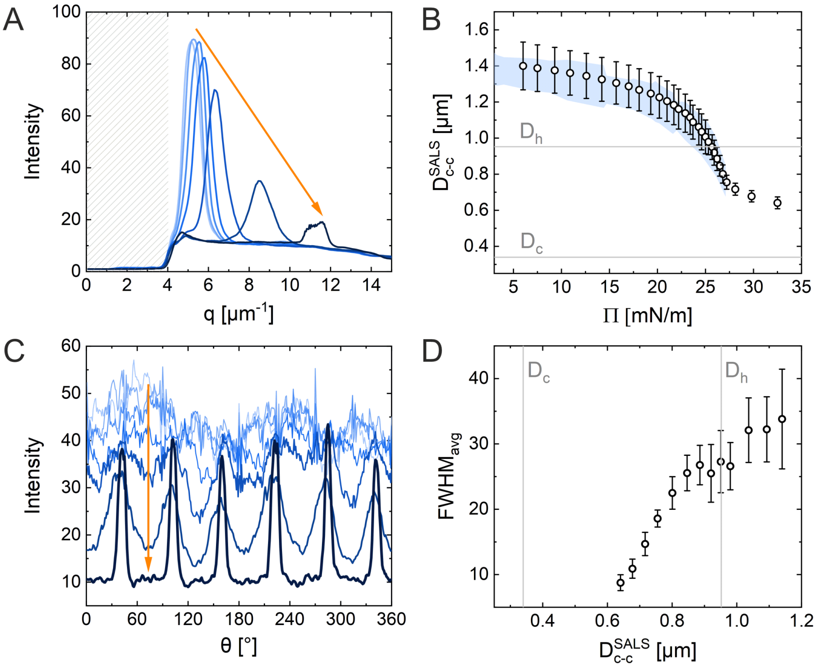

Fig. 5.5 A) Normalized integrated scattering intensity as a function of the magnitude of the scattering vector $\vec{q}$ obtained from radial averaging of the diffraction patterns. The shadowed area indicates the area covered by the beam stop. B) Calculated interparticle distances obtained from structure factor analysis of the radially averaged data shown in A), $D^{\text{SALS}}_{\text{c-c}}$ as a function of surface pressure (Π). The blue-colored area represents the data set from the *in situ* fluorescence microscopy. C) Normalized integrated intensity as a function of the azimuthal angle (θ) as analysis results of azimuthal averaging. D) Width of the Bragg peaks FWHM$_{\text{avg}}$ averaged for all six peaks as a function of $D^{\text{SALS}}_{\text{c-c}}$. The vertical grey lines highlight the core and total CS microgel diameter.

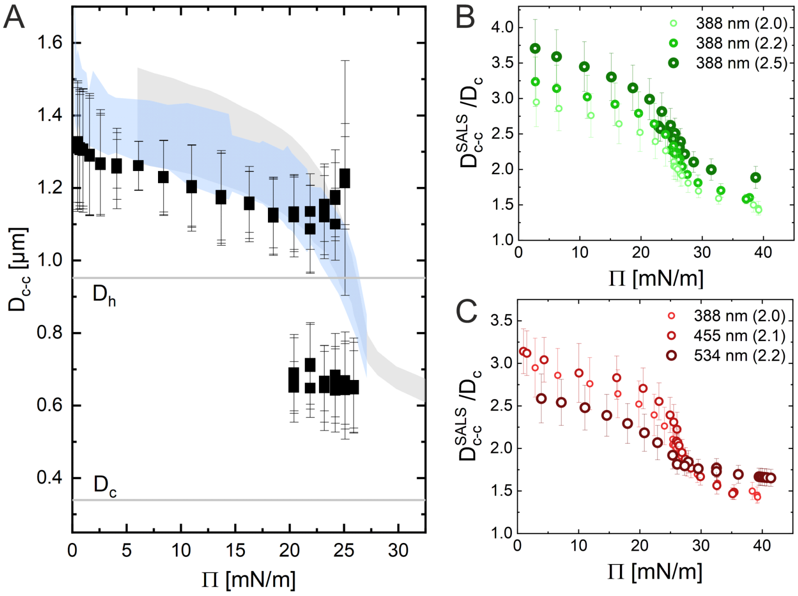

Fig. 5.6 A) $D_{c\text{-}c}$ versus surface pressure (Π) plot illustrating the difference between *ex situ* (black squares) and *in situ* (blue and grey shadows) measurements. B) LT-SALS analysis results from core-shell microgels with various shell thickness and C) different overall sizes. The numbers outside of the parentheses in the legend denote the diameter of the silica core (i.e., 388 nm) and the number inside of the parentheses their shell-to-core size ratio (i.e., 2.0).

In Figure 5.7, the compression isotherms are shown along with the diffraction patterns for selected values of Π. The incompressible nature of the silica particles (diameter measured by transmission electron microscopy, D_{TEM} = 695 ± 22 nm) with a nearly hard-spheres interaction potential is well depicted by the steeply increasing Π over relatively small changes in accessible area *A* (Figure 5.7A). The diffraction images corresponding to different values of Π reveal diffraction rings indicative of polycrystalline microstructures without any preferred domain orientation, as reported for other hard sphere and hard sphere-like systems. [200–202] As such, there are no distinguishable Bragg peaks. During compression, the position of the diffraction ring remains nearly unchanged ($D^{SALS}_{c\text{-}c}$= 719 ± 15 nm). Therefore, the system is characterized by only one length scale from the beginning to the end of the compression as expected for hard spheres in contact. This characteristic length scale, i.e. *in situ* interparticle spacing, of the silica particle monolayer is also present in the *ex situ* microscopic images and the diffraction patterns of the dried silica monolayer as shown in Figure 5.13 (SI).

The diffraction pattern obtained from the monolayers of the PNIPAM microgels (D_h = 858 ± 41 nm) goes through a transition from a diffraction ring (unordered state) to six distinct Bragg peaks (hexagonally ordered state) near the maximum Π. The monolayers showed rather small changes in Π per area reduced over the course of compression. The experiment was conducted in a highly compressed state not only because the high Π regime is where the structural change is most visible but also because the interparticle distance in the low Π regime is far too large to be resolved by diffraction analysis with our current setup. Figure 5.7B illustrates LT-SALS measurement from the final stage of the compression. The position of the diffraction patterns changes from the edge of the beam stop ($D_{\text{c-c}}^{\text{SALS}} \approx 1690$ nm) and moves away from the center to the furthest peak position, i.e., the smallest possible interparticle distance ($D_{\text{c-c}}^{\text{SALS}} = 762 \pm 128$ nm), although there is only a slight change in Π. The *in situ* fluorescence microscopy (Method 2) at lower Π (0-29.2 mN/m) in Figure 5.14 (SI) confirms that the interparticle distance at the air/water interface evolves in a continuous manner throughout the compression also for these coreless microgels. Additionally, the contrast in the spatial arrangements between the *in situ* monolayer and the dried microgels (Figure 5.15, SI), which resembles reported dried monolayer of similarly sized CS microgels, [161] further supports our conclusion that the drying process accompanies structural changes.

5.4 Discussion

“Isostructural phase transitions” in microgel-laden monolayers under compression have been ascribed to the combination of attractive capillary forces and local failures of the polymer shells, which would otherwise prevent “core-core” contact. Both contributions depend on various parameters including the degree of deformability of the shells (which is mainly determined by the crosslinker density [172]), the size of the core and the shell, the materials, and the overall synthesis protocol. *ex situ* measurements suggest that microgels with low crosslinker density show a more continuous evolution of the interparticle distance, whereas higher crosslinker densities give rise to “isostructural phase transitions”. [72, 151, 162, 164] However, we want to note that small microgels with low crosslinker density tend to self-assemble into less ordered structures. [44] Phase transitions seem also to be more likely when large microgels (e.g., $D_{\text{h}} = 1450$ nm [149]) are used or when the polymer shells are thicker in the case of CS microgels. [72] Nonetheless, there exist still several controversial results; for example, Vogel et al. [203] and Rauh et al. [17] studied CS microgels of similar size, but “isostructural phase transitions” were only observed in reference. [17] Importantly, all these results are based on *ex situ* measurements and only recent works started to provide *in situ* data. [101, 146] In particular, acquiring structural information on statistically relevant areas remains challenging. In this manuscript, we used *in situ* methods (Method 2 and Method 3) to investigate monolayers of CS microgels of size and crosslinker density similar to references [71, 72, 161, 164] and, to a smaller extent, monolayers made of coreless microgels

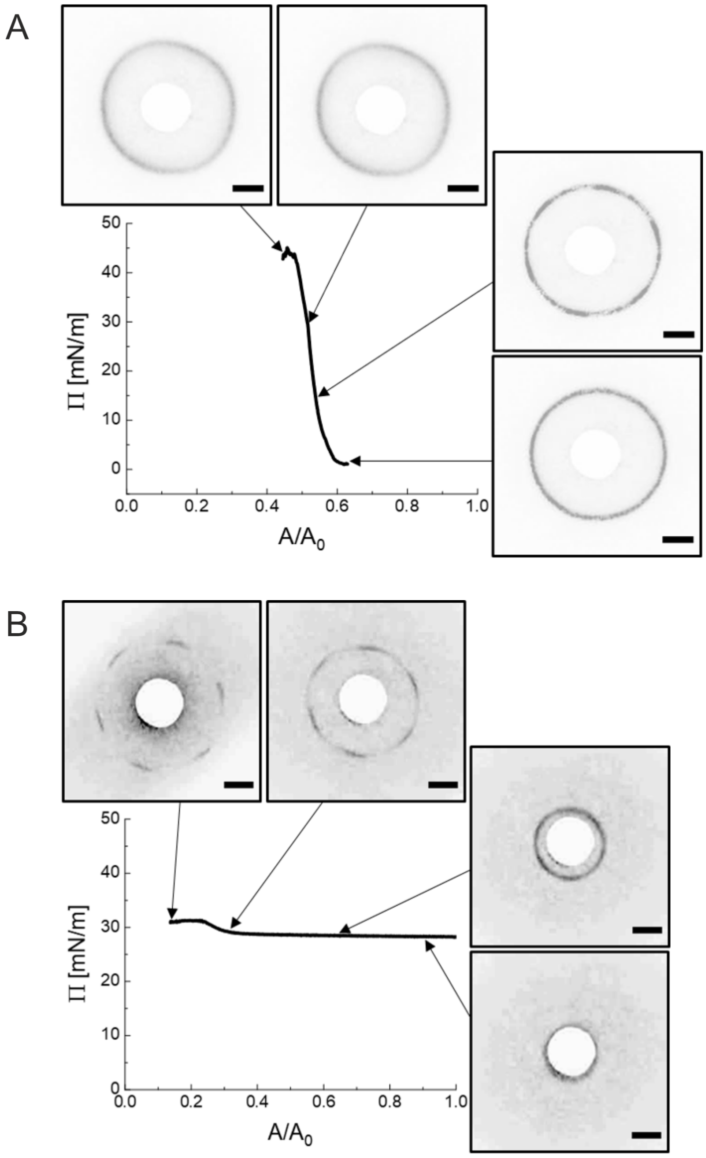

Fig. 5.7 A) Π against A/A_0, compression isotherm for silica particles along with the diffraction patterns at corresponding Π. B) Π against A/A_0, compression isotherm for PNIPAM microgels along with the diffraction patterns at corresponding Π. The contrast of the images was adjusted for better visibility. The scale bars correspond to 10 mm.

similar to references. [105, 149] In all cases, our results strongly point towards a continuous evolution of the interparticle distance, i.e., no "isostructural phase transition". The direct comparison with *ex situ* measurements (Method 1) suggests that the "structural transitions" are an artifact of the transfer and/or drying process. As such, the conflicting literature can be partly explained by taking into account the further complexity introduced by the *ex situ* measurement protocol. For example, in contrast to the often applied synchronized Langmuir-Blodgett deposition during compression also depositions at fixed surface pressures were performed. [151] What happens when a microgel-laden monolayer is transferred onto a solid substrate? Figure 5.8A illustrates a sketch of a typical CS microgel, while Figures 5.8B1 and C1 depict CS microgels with shells of different deformability at the air/water interface. As water evaporates, the microgels approach the substrate and the bottom part of the microgels will start to touch the substrate, most likely causing further deformations as illustrated in Figures 5.8B2 and C2. The contact area between the microgels and the substrate and the resulting adhesion depends on (1) the properties of the microgels (e.g., their morphology), the ones of the underlying surface (e.g., its wettability) and the transfer protocol (e.g., deposition speed). [77, 204] As the level of subphase lowers further, the microgels protrude more and more from the liquid film as shown in Figures 5.8B3 and C3, leading to a deformation of the meniscus and attractive immersion capillary forces. [50, 134, 203] Although these forces have not been measured experimentally for CS microgels, they qualitatively explain the formation of clusters as monolayers are transferred to the substrate. We briefly verified that the transfer protocol affects the *ex situ* assemblies by drying CS microgel monolayers with overall hydrodynamic diameters ranging from approximately 500 to 1000 nm [23] (5 mol.% crosslinker density) with two different drying conditions; 'slow' drying at ambient conditions against open air, and 'fast' drying using a heat gun. Figure 5.9 shows that structural changes consistent with an "isostructural phase transition" at the interface appear only after slow evaporation (blue panels). This observation implies that the microgels have enough time to rearrange when the monolayer is dried slowly under ambient conditions. This is in line with the experimental and theoretical findings of Volk et al. [18] It is noteworthy, however, that the "freezing" of monolayers by fast drying has its limits and will depend on the core dimension, the shell-to-core size ratio, and the crosslinker density. A similar conclusion was drawn by Vasudevan et al. [71] Furthermore, as the temperature influences the microgel fraction in the water subphase and mostly along the vertical direction, [146] differences in the adhesion and contact area with the substrate during drying are expected. The AFM images of Figure 5.16 (SI) reveal such a structural difference between slow and fast-dried monolayers. In particular, the phase images show the difference in contact area on the substrate. Similarly, Bochenek et al. have also reported that the drying conditions have a direct influence on the resulting microstructure. [56, 152]

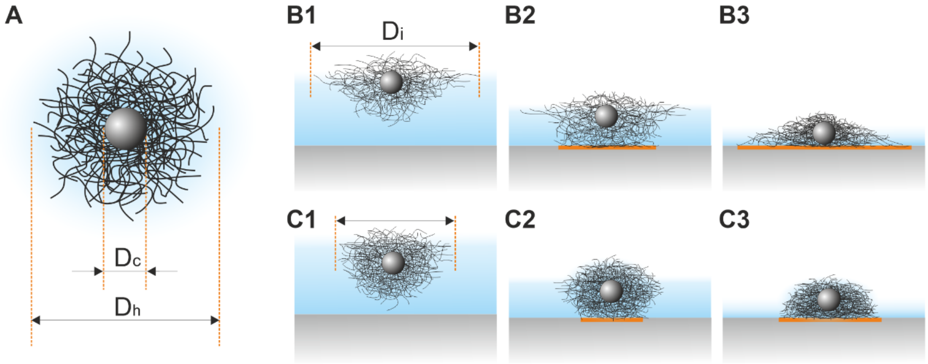

Fig. 5.8 A) Schematic illustration of the structure of a CS microgel. D_c denotes the diameter of the core and D_h the hydrodynamic diameter. B1)-B3) CS microgels with high deformability adsorbed at the air/water interface at three different drying stages. D_i denotes the diameter at the interface and the orange area depicts the contact area between the microgel and the substrate. C1)-C3) the same set of illustrations for CS microgels with low deformability.

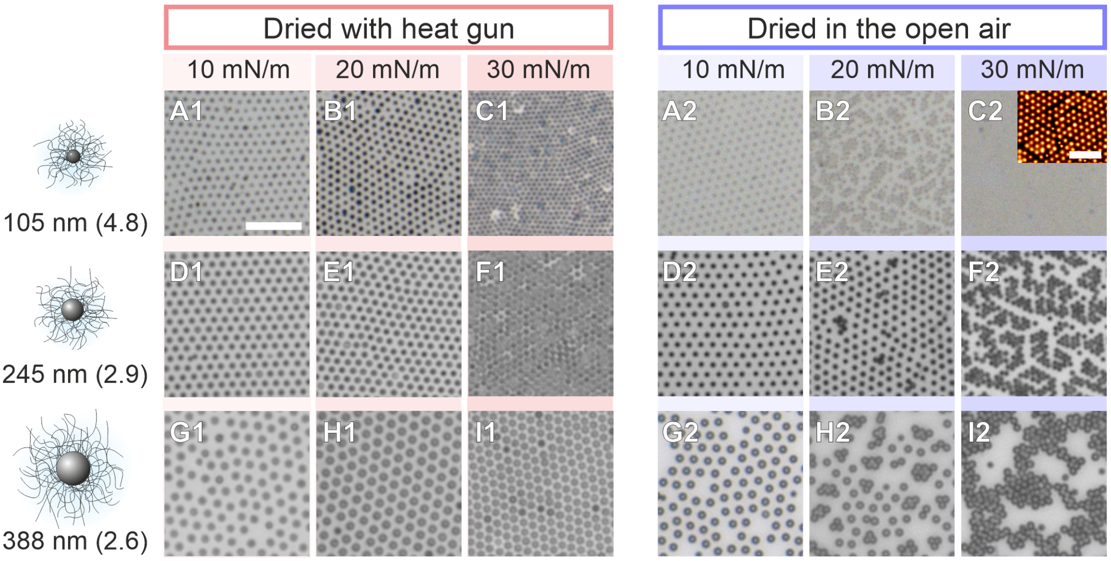

Fig. 5.9 Influence of drying conditions of CS microgel monolayers transferred to solid substrates at different surface pressures of 10 mN/m (A), 20 mN/m (B), and 30 mN/m (C). Left panel: Fast drying using a heat gun. Right panel: Slow drying against air at ambient conditions. Shown are results from CS microgels with different core sizes (105, 245, and 388 nm, from top to bottom) and shell-to-core size ratios. The scale bars correspond to 5 μm. The inset in C2 is an AFM image of the corresponding monolayer. The scale bar corresponds to 2 μm. The microgels are labeled with core diameter along with their shell-to-core size ratio in parentheses.

5.5 Conclusion

In this work, we have investigated the isothermal compression of different colloidal monolayers assembled at air/water interfaces using a Langmuir trough in combination with a self-built setup for small-angle light scattering measurements (LT-SALS). This setup allowed us to measure the interparticle distances and characterize the structural order of the monolayers *in situ*, while the total available surface area was continuously reduced by the barriers of the Langmuir trough. When using core-shell microgels with rigid cores and soft and deformable shells, we found stark differences between microstructures analyzed *ex situ* (i.e., monolayers that were transferred to solid substrates) in comparison with the *in situ* structural analysis based on optical diffraction. The *ex situ* analysis revealed an “isostructural phase transition” from core-shell microgels in shell-shell contact to “core-core” contact during compression. In contrast, the *in situ* analysis revealed a continuous decrease of interparticle distance as the monolayer is compressed. No phase transition was observed. This key result was also confirmed by *in situ* real space analysis of the monolayer using fluorescence microscopy. As a proof of concept, we also demonstrated that the *in situ* investigation using small-angle light scattering can be also applied to monolayers of rigid particles as well as low optical contrast PNIPAM microgels. LT-SALS is fast, non-destructive and relatively easy to set up from low cost components. Compared to *in situ* optical microscopy, it has several important advantages: 1) Very large monolayer areas > 1 mm^2 can be probed. Such large areas correspond to, for example, > 40×10^4 core-shell microgels that are simultaneously probed. 2) It is not necessary to have markers or strong refractive index contrast in colloid systems under investigation. 3) The measurement is less sensitive to external interferences such as vibrations. 4) Microstructural phase transitions become evident immediately due to changes of the diffraction pattern, i.e., a transition from a diffraction ring to Bragg peaks revealing the transition from a disordered to an ordered state. 5) The processing and analysis (e.g., radial averaging, peak position and width) of the diffraction patterns is much less prone to errors and less time-consuming when compared to real space analysis of microscopy images for which the centers of mass of all imaged particles have to be identified. We believe that the presented methodology will stimulate further research on colloidal monolayers at liquid/liquid or air/liquid interfaces, in particular when softness and deformability of objects are studied. [148, 172] Furthermore, the fact that phase transitions can be directly monitored *in situ* at the respective interface will allow systematic studies required to achieve a more comprehensive understanding of colloidal assembly at interfaces [53] and enable on-demand tailoring of colloidal microstructures on solid substrates—provided that the transfer protocol to the substrate is suitable to maintain the microstructure. The next important steps in this line of research are further investigation on the role of the transfer protocol as well as the surface chemistry of the substrate during the drying procedure.

5.6 Materials

Ethanol (Sigma-Aldrich, 99.8%), ethanol (Heinrich-Heine-University, chemical store, p.a.), tetraethyl orthosilicate (TEOS, Sigma-Aldrich, 98%), chloroform (Fischer Scientific, 99.8%), ammonium hydroxide solution (NH_3 (aq.), PanReac AppliChem, 30%), methacryloxyethyl thiocarbamoyl rhodamine B (MRB, Polysciences, Inc.), 3-aminopropyltrimethoxysilane (APS, Sigma-Aldrich, 97%), rhodamine B isothiocyanate (Sigma-Aldrich, mixed isomers), 3-(trimethoxysilyl)propyl methacrylate (MPS, Sigma-Aldrich, 98%), *N*,*N*'-methylenebisacrylamide (BIS, Sigma-Aldrich, 98%), potassium peroxodisulfate (KPS, Sigma-Aldrich, 99%), and sodium chloride (NaCl, Sigma-Aldrich, 99.5%) were used as received. Water was purified by a Milli-Q system (18.2 $M\Omega \cdot cm$) and *N*-isopropylacrylamide (NIPAM, TCI, 97%) by recrystallization from cyclohexane (Fisher Scientific, 99.8%).

5.7 Synthesis

5.7.1 Silica particles and silica-PNIPAM CS microgels

The detailed synthesis protocol for both silica nanoparticles and micron-sized silica-PNIPAM microgels can be found in. [23] In short, silica particles were synthesized via the well-known Stöber procedure. RITC dye was incorporated in the particles that were used for fluorescence microscopy experiments. The PNIPAM shell encapsulation was done via seeded precipitation polymerization. The silica particles used to create monolayers at the air/water interface were measured to be 695 ± 22 nm (126 particles counted) in diameter by TEM. Its ethanolic dispersion was mixed with chloroform with 1:4 volume ratio to assist spreading of the silica particles at the air/water interface. Surface charges were screened by adding 100 mM NaCl in the aqueous subphase of the Langmuir trough in order to achieve rigid sphere-like interactions. The main CS microgels used for the *in situ* and *ex situ* comparison had a core with a diameter of 340 ± 20 nm. The D_h of the total CS microgel was measured to be 920 ± 18 nm at 20°C using dynamic light scattering (DLS). The purified dispersion was freeze-dried, re-dispersed in ethanol with 5 w/v% and stored on a 3D shaker overnight prior to the monolayer deposition at the air/water interface. Ethanol was used as spreading agent.

5.7.2 PNIPAM microgel synthesis

The synthesis protocol for the PNIPAM microgels was adopted from a previously published work. [66] 5 g of PNIPAM and 50 mg of BIS were dissolved in 50 ml of water in a three-neck round-bottom flask equipped with a reflux condenser and a magnetic stirrer. 1 mg of MRB dye was dissolved in 1 ml of water and added to the flask. The mixture was heated to 40°C and purged with nitrogen while stirring. 20 ml of the mixture was transferred to another flask, where 10 ml of additional water was added. The rest was kept in a syringe with a needle and placed on a syringe pump for the continuous feeding of the monomers. The mixture in the flask was heated to 80°C and equilibrated. 10.4 mg of KPS was dissolved in 2 ml water and added to the flask. Once the dispersion started to become turbid, indicating that the polymerization was initiated, the syringe pump was started with the speed of 1 ml/min. 5 minutes after the feeding process, the polymerization was quenched by dipping the flask in an ice bath and the dispersion was filtered through glass wool. The synthesized PNIPAM microgels were dialyzed against water for two weeks, freeze-dried and re-dispersed in ethanol (1 w/v%) as for the CS microgels. The size of the PNIPAM microgels at 20°C was determined by DLS (D_h = 858 nm ± 41 nm).

5.8 Experimental

5.8.1 *ex situ* investigation after Langmuir-Blodgett deposition (Method 1)

For the *ex situ* analysis, we followed the well-established protocol to study the phase behavior of CS microgel monolayers at the air/water interface. [17, 72, 160] According to the protocol, the microgel monolayer at the air/water interface is simultaneously transferred to a substrate during the compression, dried as the substrate is pulled out and examined under a microscope, hence referred to as an *ex situ* approach. The total duration of the substrate pulled out is often matched with the total duration of the compression, consequently enabling the position of the substrate to the corresponding Π tracing. This link between the substrate position to Π was established under the assumption that the number of particles transferred from the air/water interface per time is negligible thus does not influence the measured value of Π. The transfer of the monolayer was carried out using a Langmuir-Blodgett deposition trough (Microtrough G2, Kibron Inc.) equipped with a film balance, two Delrin barriers, a dip coater and an acrylic cover box. A standard microscope glass slide was treated in an ultrasonic bath sequentially with Hellmanex aqueous solution (2 vol.%), water (2 ×) and in ethanol (2 ×) for 15 minutes each. The cleaned glass slide was then cut in half along its length and the position markings were carved on its back to trace the corresponding Π at the moment of monolayer transfer (see Figure 5.10A for a schematic illustration of the procedure). Before the deposition of the particle monolayer, the trough and the barriers were thoroughly cleaned with water, ethanol and again rinsed with water. The trough was then filled with water with the barriers closed. The glass slide was thoroughly rinsed with water before being mounted to the dip coater (parallel to the barriers and perpendicular to the air/water interface), positioned at the center of the trough and lowered 55 mm below the interface. An aspirator with a narrow tip was used to remove any residual floating substances at the interface between the two barriers as well as to flatten the interface by lowering its level to the height of the trough wall. A Wilhelmy plate was rinsed with water and ethanol and held over a flame to remove any impurities and cooled before it was mounted to the film balance. The barriers were then opened to the maximum area. Only when the fluctuation of the surface tension value was below 0.3 mN/m while opening the barriers, the particles were deposited at the air/water interface using a 10 or 20 μl micropipette. The colloidal dispersion was treated alternating between vortex mixing and sonication for 2-4 minutes prior to the deposition. The injection was done slowly at a shallow angle with the tip of the micropipette gently touching the interface. The compression was started with the speed of 150 mm^2/min after at least 15 minutes of equilibration time after deposition. The glass substrate was pulled out simultaneously at the speed of 84 mm/min over a time that matched the total duration of the compression. The glass substrate was left hanging until it was completely dried. Three images were taken every 2.5 mm using an upright microscope (Eclipse LV150N, Nikon). The acquired images were processed and analyzed by ImageJ (1.53k, National Institutes of Health, USA) alongside the recorded compression isotherm. Additional information regarding image processing can be found in SI. All experiments were done at room temperature. The interparticle distances were determined from the first peak of the radial distribution functions (RDFs) and are denoted as $D_{\text{c-c}}^{\text{im,ex}}$, where D stands for "distance", im for "image", ex for "*ex situ*" and c-c for "center-to-center".

5.8.2 *in situ* investigation by fluorescence microscopy combined with a Langmuir trough (Method 2)

The *in situ* measurements by fluorescence microscopy were conducted in another Langmuir trough (KSV NIMA inverted, Biolin Scientific) equipped with two Delrin barriers, an inverted microscopy trough and a black acrylic cabinet. A microscope (Olympus IX73) equipped with a mercury lamp, a fluorescence filter set, a CMOS camera and a 60× objective was used to probe the colloid-laden interface at various values of Π. The setup was placed on an optical table combined with pneumatic vibration isolation (Nexus, Thorlabs Inc.) and is illustrated in Figure 5.10B. The microscopy trough was cleaned and prepared in the same way as for the *ex situ* experiments previously described. Once the air/water interface was clean enough (surface pressure fluctuation below 0.3 mN/m, measured by a Wilhelmy plate), the microgels were deposited at the interface. The compression was done stepwise with the compression speed of 10 mm/min. Images were taken after at least 15 minutes of equilibration time at each step. Three different volumes of the microgel dispersion were used and consequently three compression isotherms were measured to address the full range of Π. Three images were acquired from different positions for each measured Π and processed by ImageJ alongside the Π measured at the moment of image acquisition. All experiments were done at room temperature.

5.8.3 *in situ* investigation by LT-SALS (Method 3)

The *in situ* measurements by LT-SALS were performed with the same Langmuir trough (KSV NIMA) used for the *in situ* fluorescence microscopy experiments. Along with the Langmuir trough, the cabinet was placed on an optical table, on which a blue diode laser (MediaLas, LDM-20-405, 20 mW, 405 nm) and two mirrors (Thorlabs, BB1-E02) were set up. A customized metal frames was installed around the Langmuir trough to mount a paper screen and a CCD camera (Thorlabs, DCU223C-MVL6WA) above the trough. The schematic of the setup is depicted in Figure 5.10C (see also the SI for more details regarding the setup and laser alignment). The monolayer deposition at the air/water interface was done as for the *in situ* fluorescence microscopy study. The compression was started after at least 15 minutes of equilibration time with the speed of 150 mm^2/min. The laser intensity was adjusted with a neutral density filter (Thorlabs, NDC-50C-4M). Diffraction patterns were recorded during the entire compression at 0.2 frames per second. The resulting video was analyzed alongside the recorded compression isotherm using ImageJ (one data point every five seconds). All experiments were done at room temperature.

5.8.4 Dynamic light scattering (DLS)

DLS measurements were performed with a 3D LS spectrometer (LS Instruments) at a constant temperature of 20°C. The measurements were repeated three times with 40 seconds of acquisition time. The device was equipped with a HeNe laser (632.8 nm), a decalin bath and two avalanche photodiodes in pseudo-cross-correlation mode as detectors. The dilute samples (volume fraction « 0.001) were measured in borosilicate cuvettes with an outside

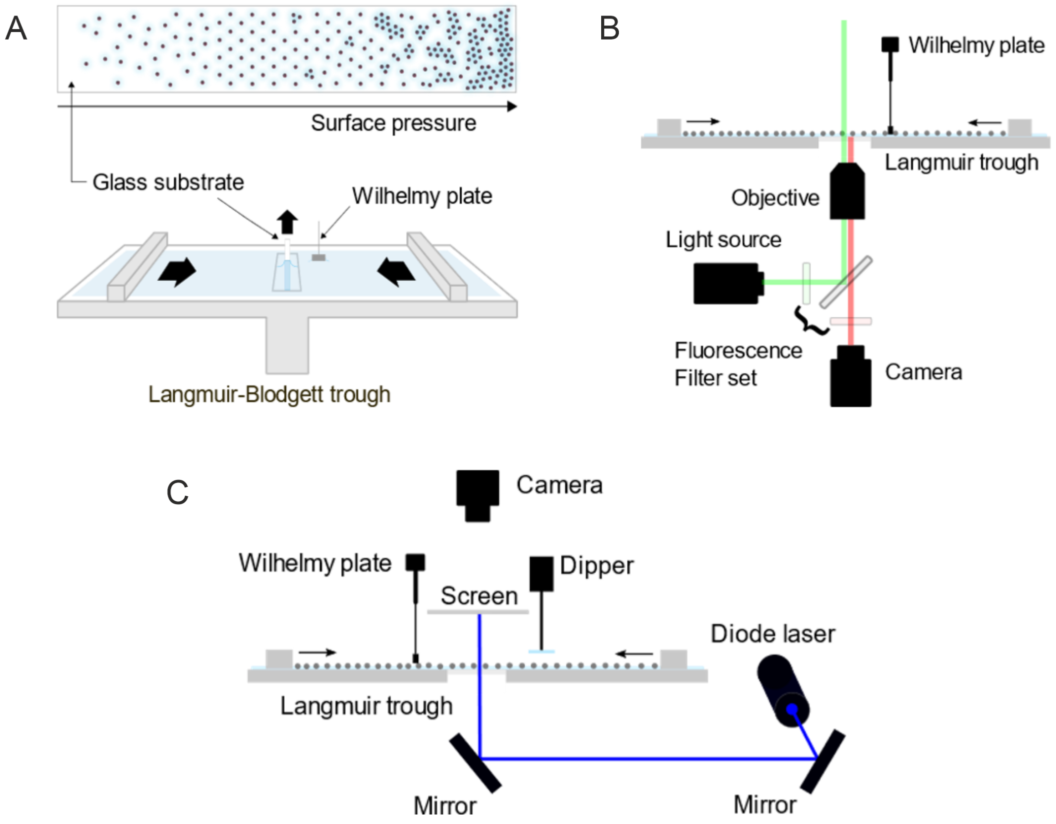

Fig. 5.10 Schematic illustration of A) the transfer of a colloidal monolayer to a glass substrate using a Langmuir-Blodgett trough, B) the Langmuir trough combined with a fluorescence microscope, and C) the Langmuir trough combined with a small-angle light scattering (LT-SALS) setup.

diameter of 10 mm. The obtained intensity-time autocorrelation functions were analyzed using cumulant analysis.

5.8.5 Transmission electron microscopy (TEM)

TEM measurements were performed using a JEOL JEM-2100 Plus microscope operated in bright-field mode at 80 kV acceleration voltage. The sample preparation was done by applying a drop of the respective particle dispersion on a carbon-coated copper grid (200 mesh, Science Services) and drying at room temperature. The captured images were then processed with ImageJ for the size analysis.

5.9 Acknowledgements

The authors acknowledge the DFG and the state of NRW for funding the cryo-TEM (INST 208/749-1 FUGG). M.K. acknowledges the German Research Foundation (DFG) for funding under grant KA3880/6-1. The authors also would like to thank Sonja Schiller (HHU Dusseldorf) for assistance in building the setup, Dr. Kiran Kaithakkal Jathavedan for providing the PNIPAM microgels, Marius Otten (HHU Dusseldorf) for TEM imaging and Jonathan Garthe (HHU Dusseldorf) for Langmuir-Blodgett deposition of many samples. K.K would like to express special thanks to Prof. Michel Cloitre, Prof. Igor Potemkin, Prof. Jérôme J. Crassous, Prof. Janne-Mieke Meijer, Prof. Walter Richtering and others for inspiring lectures and fruitful discussions during the 3rd International Summer School on functional microgels and microgel systems. The authors acknowledge the reviewers for their constructive feedback and helpful suggestions.

5.10 Supporting Information

5.10.1 *in situ* fluorescence microscopy of the main CS microgel at low Π

Figure 5.11 shows a microscopy image (*in situ*) of a monolayer of the main CS microgel (the same CS microgel presented in Figure 5.1-5.4—the main CS microgel). Here, Π is very low (0.2 mM/m) but still showing that attractive interactions are present at the interface.

5.10.2 Additional *ex situ* vs *in situ* differences for the main CS microgels

Figure 5.12A shows $D_{\text{c-c}}$ plotted as a function of the particle number per unit area (n_{p}/A). Theoretical values of $D_{\text{c-c}}$ for close-packed, perfectly hexagonally ordered monolayers were

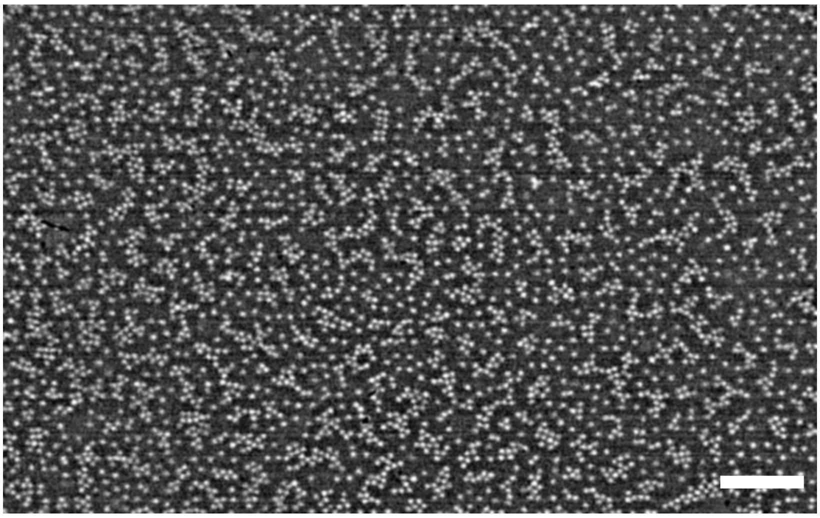

Fig. 5.11 Fluorescence microscopy image (Method2) of a CS microgel monolayer at $\Pi = 0.2$ mM/m. The scale bar corresponds to 20 μm. The image was processed by ImageJ (Bandpass filter – Gaussian Blur) for better visibility.

calculated according to our already published work. [23] These values are compared with ex- and *in situ* microscopy data. Figure 5.12B illustrates the systematic shift of n_p/A in *ex situ* measurement compared (filled squares) to the *in situ* method (open squares) at the same measured Π.

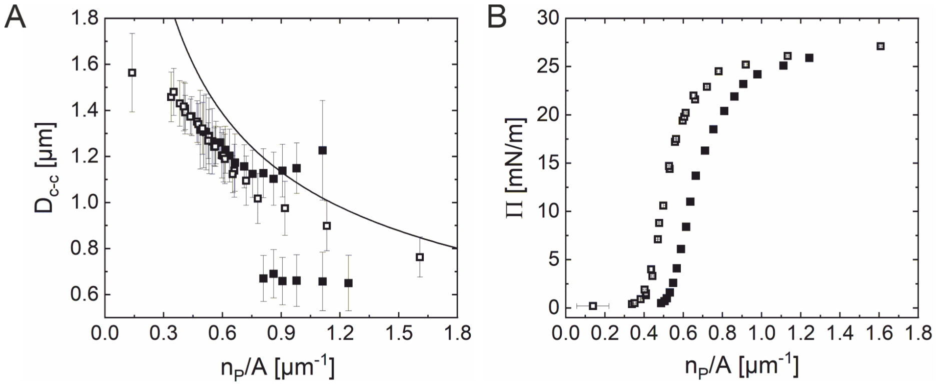

Fig. 5.12 A) $D_{\text{c-c}}$ as a function of n_p/A. The solid line corresponds to the calculated, theoretical evolution of $D_{\text{c-c}}$ (under the assumptions that the monolayer has a perfect hexagonal symmetry with the area fraction of 0.9069). The filled squares correspond to the *ex situ* and the empty squares to the *in situ* measurement results, respectively. B) Π as a function of n_p/A obtained from *ex situ* (filled squares) and *in situ* (empty squares) measurements.

5.10.3 Monolayers of silica particles

The monolayer of silica particles shown in Figure 5.7A of the main manuscript was transferred and dried onto a solid substrate using Langmuir-Blodgett deposition. Figure 5.13 shows microscopic images and SALS patterns of these monolayers for different values of Π (see caption). The diffraction patterns vary from ring-like to peak-like depending on the position on the substrate.

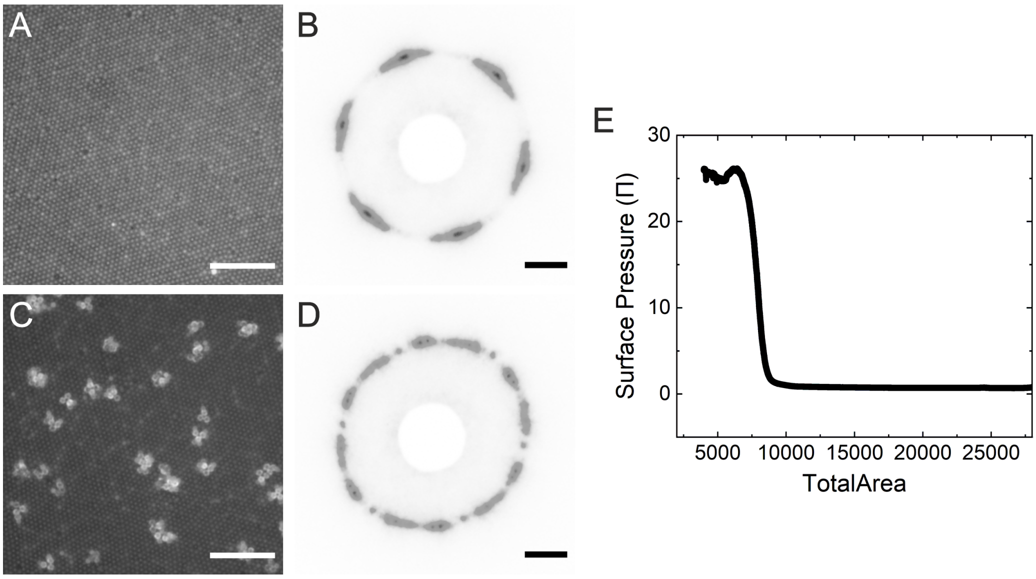

Fig. 5.13 A) Optical light microscopy image and B) diffraction pattern of a dried silica monolayer (*ex situ*) at Π = 0.5 mN/m. C) and D) show the same but at Π approx. 20 mN/m. The scale bars in A) and C) correspond to 10 μm. The scale bars in B) and D) correspond to 10 mm. E) Compression isotherm recorded during the Langmuir-Blodgett deposition.

5.10.4 Monolayers of (coreless) PNIPAM microgels

The system of coreless microgels shown in Figure 5.7B of the main manuscript was also investigated *in situ* using fluorescence microscopy (Method 2), also in a range of Πs where the interparticle distance is too large to be resolved in our current LT-SALS setup. Figure 5.14 shows microscopic images of the microgel monolayer at different Π. We do not observe an “isostructural phase transition”.

The same monolayer of microgels was then studied *ex situ* after Langmuir-Blodgett deposition. Figure 5.15A and C show optical light microscopy images of the dried microgel monolayers prepared at two different Π of 30.2 (black) and 31.2 mN/m (red). Figure 5.15B and D show AFM images of the corresponding microgel monolayers. Figure 5.15E shows

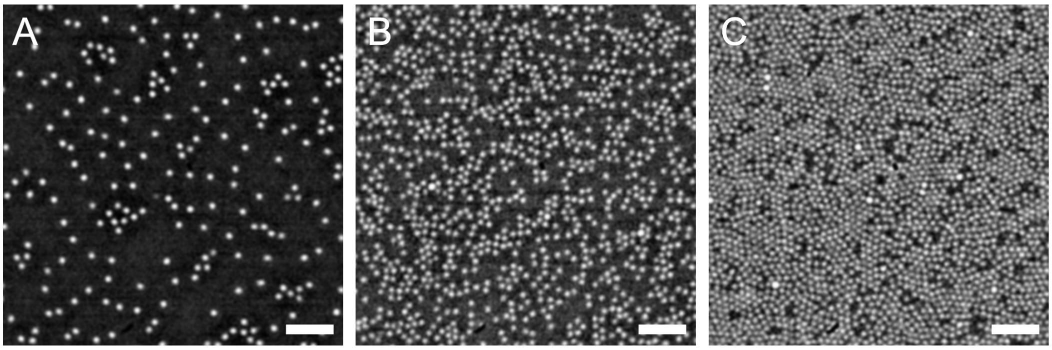

Fig. 5.14 Microgel monolayer (*in situ*) Π at A) 3.7, B) 28.4, C) 29.2 mN/m. The scale bars correspond to 10 μm. The images were processed by ImageJ (Bandpass filter – Gaussian Blur) for better visibility.

calculated radial distribution functions (RDFs) as well as nearest neighbor center-to-center distances, $D_{\text{c-c}}$. Figure 5.15F displays the diffraction pattern recorded by SALS, representative for the microgel monolayers taken from Π between 30.2 and 31.2 mN/m.

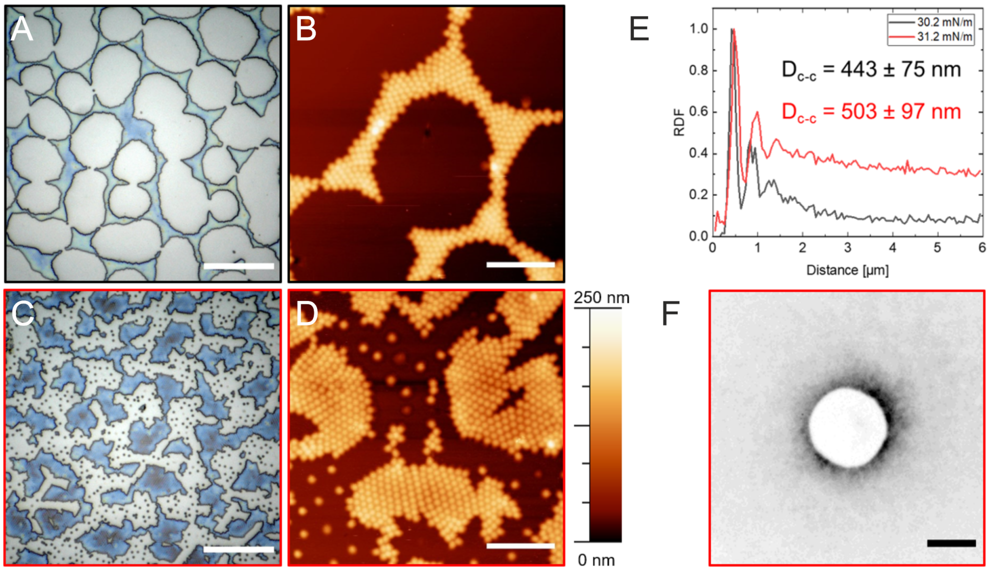

Fig. 5.15 A) Microgel monolayer (*ex situ*) at $\Pi = 30.2$ mN/m by light microscopy, scale bar: 20 μm B) by AFM, scale bar: 5 μm. C)-D) the same data set for the microgel monolayer (*ex situ*) at $\Pi = 31.2$ mN/m. E) interparticle distance from RDF. F) Scattering pattern of the microgel monolayer from C), scale bar: 10 mm.

5.10.5 AFM images of CS microgel from Figure 5.9—105 nm (4.8)

The microscopic image of CS microgel (D_c: 105 nm, shell-to-core size ratio: 4.8) in Figure 5.9C2 (dried in open air) of the main manuscript could not be resolved due to the relatively homogeneous refractive index of the microgel, in comparison with Figure 5.9C1 (dried with heat gun). Figure 5.16A and C show AFM measurements on these monolayers at lower Π (10 mN/m), and Figure 5.16C and D are the corresponding phase images.

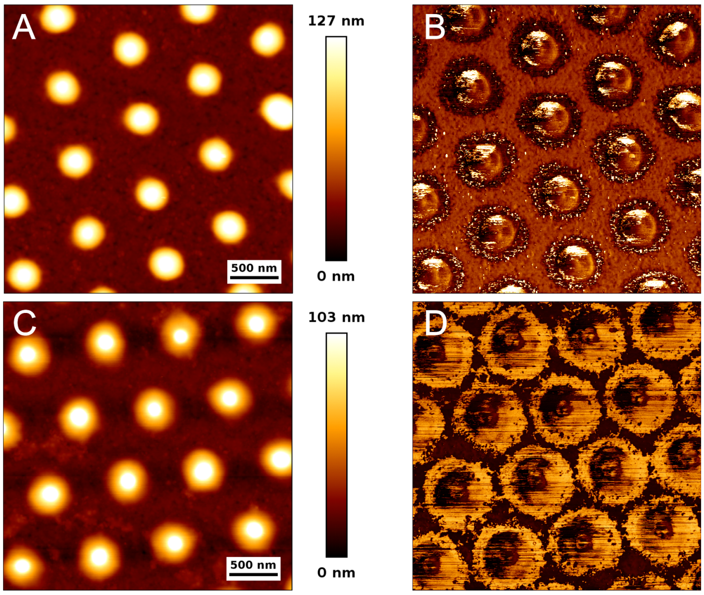

Fig. 5.16 A) AFM image of CS microgel—105 nm (4.8)—monolayer dried with heat gun B) phase image of A). C)-D) the same set of data for the monolayer dried in open air at room temperature.

The interparticle distance measured by LT-SALS ($D_{\text{c-c}}^{\text{SALS}}$) was calculated as follows:

$$q = \frac{4\pi n}{\lambda}\sin\left(\frac{1}{2}\arctan\left(\frac{xy}{D_{\text{S-D}}}\right)\right)$$

where q is the magnitude of the scattering vector in μm^{-1}, n is the refractive index (refractive index of air, $n = 1$), λ is the wavelength of the light in μm, x is the distance from the primary beam in pixels, y is the conversion factor in mm per pixel, and $D_{\text{S-D}}$ is the sample-to-detector distance in mm. The scattering vector yields the lattice spacing $D_{\text{hk}} = \frac{2\pi}{q}$. For a two-dimensional, hexagonally ordered system, the interparticle distance is $D_{\text{c-c}} = \frac{2}{\sqrt{3}} D_{\text{hk}}$.

With a blue diode laser ($\lambda = 405$ nm), the available q-value ranges from 0.39 to 15.74 μm^{-1} ($D_{\text{c-c}}$ approximately from 460 nm up to 18 μm). With a green and red diode laser ($\lambda = 532$ nm, 632.8 nm), the available q-value ranges from 0.30 to 11.98 μm^{-1} ($D_{\text{c-c}}$ approximately from 600 nm up to 24 μm) and from 0.25 to 10.07 μm^{-1} ($D_{\text{c-c}}$ approximately from 720 nm up to 29 μm), respectively. Figure 5.17 depicts LT-SALS measurements done with blue and red lasers as well as the $D_{\text{c-c}}$ range for three different laser types graphically.

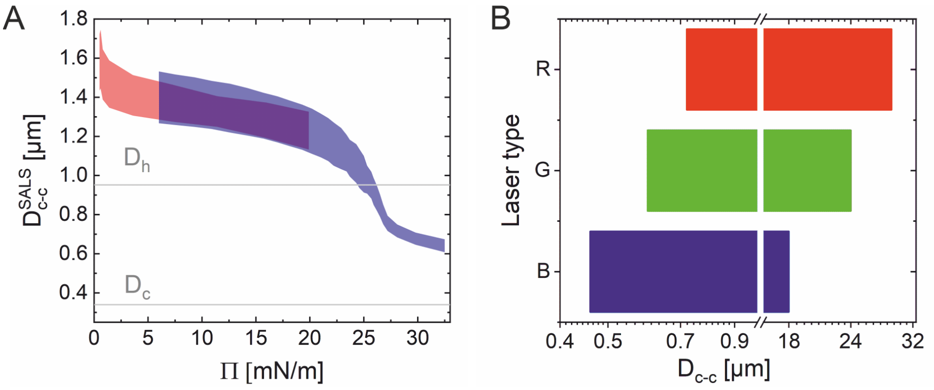

Fig. 5.17 A) LT-SALS measurement done with blue and red lasers on the same CS microgel. B) Calculated possible range of $D_{\text{c-c}}$ for different laser wavelengths for our setup, R-red, G-green and B-blue.

5.10.6 Image processing and analysis by ImageJ (1.53k, National Institutes of Health, USA)

Radial Distribution Functions (RDFs) were calculated with ImageJ macro version 2011-08-22 by Ajay Gopal using the center of mass positions of each CS microgel. To find the centers, the *ex situ* light microscopy images were pre-processed with Gaussian blur. Particles at the edges of the images were excluded. The *in situ* fluorescence microscopy images were then processed with Bandpass filter, background subtraction and Gaussian blur. Grey scaled LT-SALS images were radially and azimuthally averaged by Radial Profile Plot (Version 2009-08-14 by Paul Baggethun) and Azimuthal Average (Version 2007-09-08 by Philippe Carl), respectively.

5.10.7 LT-SALS setup

The level of accuracy was checked with all the involved components in the laser path using a circular level. The laser was aligned with the camera center with two mirrors and through the microscopy window of the trough by using a pinhole on a rail, which consisted of two parallel rods screwed into the optical plate. After the alignment, the rail and the pinhole were removed. The Langmuir trough and the camera were placed back in the laser path. The paper screen (width: 90 mm) was rolled around two metal rods, fastened parallel to the trough and fixed on the customized frame, see Figure 5.18. The laser beam center was marked on the screen for various size of beam stops to be glued on when required. The sample-to-detector distance ($D_{\text{S-D}}$) was measured with a ruler ensuring all four corners of the screen have the same distance to the trough wall. The pixel/mm value was determined using millimeter paper after all the involved components were fixed on their positions. The screen was rolled back and put aside on one metal rod for the cleaning of the trough. The trough was filled again with water before the screen was rolled out and fixed back to its position. Then the monolayer was deposited at the air/water interface. The $D_{\text{S-D}}$ of our current setup could be varied from 25 to 200 mm (scattering angle ranges from 2 - 74°).

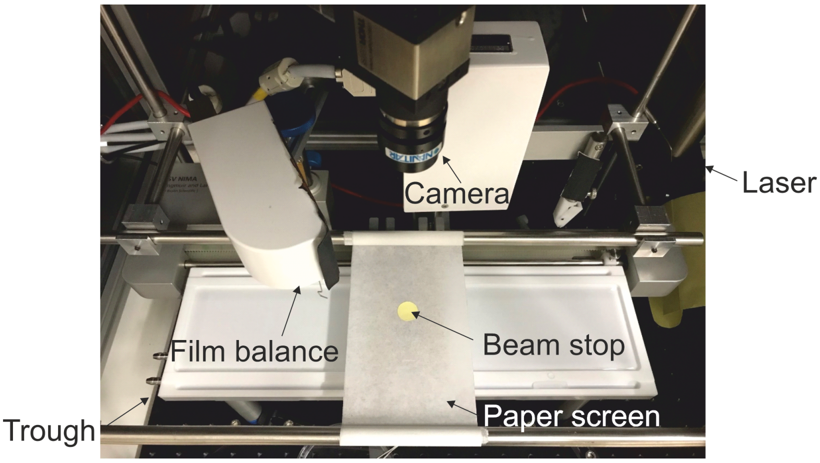

Fig. 5.18 Photograph of the LT-SALS setup.

Chapter 6

Drying of soft colloidal film

Keumkyung Kuk[a], Julian Ringling[a], Kevin Gräff[b], Sebastian Hänsch[c], Virginia Carrasco-Fadanelli[d], Andrey A. Rudov[e,f], Igor I. Potemkin[e,f], Regine von Klitzing[b], Ivo Buttinoni[d], and Matthias Karg[a*]

[a]Institut für Physikalische Chemie I: Kolloide und Nanooptik, Heinrich-Heine-Universität Düsseldorf, Universitätsstr. 1, 40225 Düsseldorf, Germany
[b]Institute for Condensed Matter Physics, Soft Matter at Interfaces, Technische Universität Darmstadt, Hochschulstr. 8, 64289 Darmstadt, Germany
[c]Center for Advanced Imaging, Heinrich-Heine-Universität Düsseldorf, Universitätsstraße 1, 40225 Düsseldorf, Germany
[d]Institut für Experimentelle Physik der kondensierten Materie, Heinrich-Heine-Universität Düsseldorf, Universitätsstr. 1, 40225 Düsseldorf, Germany
[e]Leibniz Institute for Interactive Materials, 52056 Aachen, Germany
[f]Physics Department, Lomonosov Moscow State University, Moscow 119991, Russian Federation

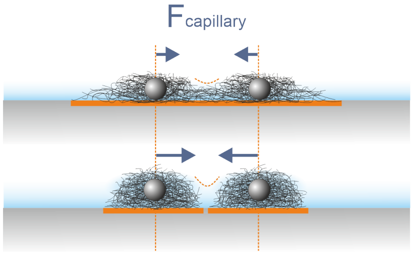

KEYWORDS: interface-mediated colloidal assembly; thin film; microgel-to-substrate adhesion; microgels; capillary forces;

Note that this section is written in American English, and still in progress.

6.1 Introduction

Surface active agents are ubiquitous in our daily lives and paramount for numerous industrial applications including emulsion stabilization, foam formation, detergency, pharmaceutical drug delivery, and structured surfaces. [205] They often consist of amphiphilic molecules (surfactants) that adsorb onto the interface between two immiscible phases (e.g., water and air), lower the surface tension, and stabilize the interface, e.g., against droplet coalescence. Remarkably, the same stabilization can be achieved via adsorption of solid micro- and nanoparticles, as in the case of Pickering emulsions. [126] In contrast to molecular surfactants, solid particles offer a reduced environmental footprint as they do not alter the chemical composition of the fluid surface [206] and generate interfacial films with significantly greater thickness due to their larger size. [127] Additionally, the solid particles need longer times to adsorb (in line with their characteristic diffusion timescale). And their presence at the interfaces often leads to the deformation of the interface due to their weight/size, [207] shape, [208] porosity, [139] and/or wetting properties, [209] which give rise to capillary interactions among adjacent particles. For example, the attractive force felt between two particles at the air/water interface (flotation capillary force) increases with the sixth power of the particle size and becomes negligible when the particle is smaller than 10 μm. [134, 210] Contrastingly, tiny particles, as small as protein globules, can be subject to the influence of a strong attractive force when trapped in a thin water film (immersion capillary force). [50]

Consequently, such interfacial deformations can have dramatic impacts on the way a film dries on hard surfaces, leading, for example, to highly inhomogeneous drying conditions during coating and deposition processes. The problem can be potentially solved by employing "sticky" and deformable polymeric particles. Examples are poly(*N*-isopropylacrylamide) (PNIPAM) microgels, i.e., highly swollen crosslinked polymer networks that can be synthesized in different structures, sizes, and softness. They also readily adsorbed at various interfaces as their solid counterparts do, assuming a "fried egg" shape at the interface, i.e., by stretching along the interfacial plane. They then can be assembled into closed-packed viscoelastic films of high porosity properties that are reminiscent of biological interfaces [211] and interactions, e.g., cell adhesion. [212, 213]

To date, the microstructure and mechanical properties of microgel-laden interfaces have been widely studied using Langmuir-Blodgett setups (fluid interface-assisted assembly by means of lateral compression, followed by deposition onto solid substrates) using microgels with various sizes and crosslinker densities. Conversely, very little is known about how these films dry, even though drying effects could significantly alter the microstructure of a microgel-laden interface upon transfer onto solid substrates. [30, 214] The research gap exists primarily because visualizing interfaces deformed by such microgels is difficult, and a comprehensive theoretical framework that describes the complex physics during drying is yet to be established. [51, 80, 140, 142]

In this work, we use a combination of video microscopy and thin film interference to shed light on the drying process of microgel interfacial films on differently modified substrates (hydrophobic vs. hydrophilic). By considering micron-sized silica-PNIPAM core-shell (CS) microgels [23] of comparable sizes and different crosslinker densities (i.e., softness), we elucidate the interplay between two key elements: the microgel-to-substrate adhesion and the capillary forces experienced by microgels in an immersed state (immersion capillary force). Relatively homogeneous drying is reported for microgel films with a lower crosslinker density on hydrophobic substrates, whereas the correspondence with a higher crosslinking density on hydrophilic solid surfaces leads to significant alterations in the original microstructure. We anticipate similar effects during the deposition of other soft films, such as those composed of polymers or lipids.

6.2 Results

We synthesized three batches of silica-PNIPAM core-shell microgel systems, denoted as $C_{437}S_{2.6}$-1.0, $C_{437}S_{2.3}$-2.5, and $C_{437}S_{2.4}$-7.5. The nomenclature C_iS_j-k carries following information: C represents the core with a diameter D_c = i (measured in nm through transmission electron microscopy); S denotes the shell, characterized by an overall shell-to-core size ratio of j; and k indicates the crosslinker density of the shell in mol.%. Consequently, the three model microgels share the same core and have a comparable overall hydrodynamic size. However, they feature shells of varying elasticity, with $C_{437}S_{2.4}$-7.5 being the most elastic among the three. The difference in elasticity among the CS microgels becomes evident in the lateral deformation degree at the air/water interface (due to interfacial tension), the interfacial diameter D_i (here defined as mean nearest center-to-center distance, $D_{c\text{-}c}$, at surface pressure, Π, 0 mN/m) normalized by the hydrodynamic diameter, D_h, as shown in Figure 6.1 and Table 6.1 in the Supporting Information, SI. The D_i measurements were done by reflected light microscopy with 30 minutes of equilibration time after the adsorption of CS microgels at the air/water interface from ethanolic dispersion (ethanol as the spreading agent) as well as from aqueous dispersion (spontaneous adsorption from subphase), where they form clusters. Such clustering of the CS microgels are shown in Figure 6.9 in SI.

Using ethanol as a spreading agent, the microgels were floated at the air/water interface in a Langmuir-Blodgett trough (Microtrough G2, Kibron Inc.), where the surface-modified solid substrate was immersed (90°to the interface and parallel to the barriers) by a dipper. The

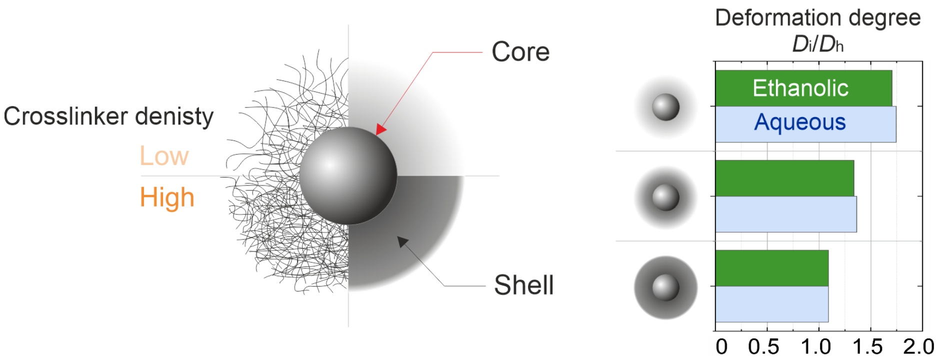

Fig. 6.1 Schematic illustration of the core-shell microgel with various crosslinker densities: $C_{437}S_{2.6}$-1.0, $C_{437}S_{2.3}$-2.5, and $C_{437}S_{2.4}$-7.5 with their lateral deformation degrees at the air/water interface (D_i/D_h).

microgel-laden interface was later compressed by means of lateral barriers to reach a given Π. Three values of Π are considered to achieve various $D_{c\text{-}c}$ (i.e., compression state): approx. 10, 20, and 30 mN/m, to which we will refer as ‘low’, ‘mid’, and ‘high Π’. Video microscopy of drying interface was performed by transferring the microgel-laden interface rapidly at constant surface pressure, [111, 151, 215] using a technique known as Langmuir-Blodgett deposition. For the preparation of hydrophilic substrates, standard microscopy glass slides were thoroughly cleaned and subsequently plasma-treated right before the experiment. For the hydrophobic substrates, the glass slides were RCA cleaned [23] and fluorinated via chemical vapor deposition. Details regarding the microgel synthesis, Langmuir-Blodgett deposition and substrate preparation are in the Experimental Section. Images of the drying microgel-laden interfaces (frequently known as microgel monolayer or microgel films) are taken *in situ* soon after the transfer, approx. 5 fps using reflected brightfield microscopy (Eclipse LV150N, Nikon) equipped with a camera (DS-Fi3). They show unprecedented resolution down to the single-microgel level (even at a high Π) thanks to the thick shells and silica cores providing large center-to-center distances and strong optical contrast, respectively. Under our imaging conditions, the drying microgel films also exhibit iridescent colors resulting from thin film interference. [216] These colors can be used to map the local height of the microgel-laden interface with respect to the underlying substrate (details about this method are given in the Experimental Section).

Figure 6.2 depicts the drying of a $C_{437}S_{2.3}$-2.5 film at mid Π on hydrophilic (Figure 6.2, panels A1-F1) and hydrophobic (Figure 6.2, panels A2-F2) substrates at various stages of the drying process (the corresponding Videos are in SI). Confocal scans of the meniscus cross-section are used to measure the slope of the meniscus during drying (see Experimental Section), i.e., the receding wetting angles $\theta_1 = 0.82° \pm 0.16°$(hydrophilic substrate, Figure

6.10 in SI) and $\theta_2 = 2.00° \pm 0.53°$(hydrophobic substrate, Figure 6.11 in SI). Panel A1 shows the microstructure of the microgel film on the inclined interface. Following this stage, we report the formation of a thin fluid layer, where the microgel-laden interface aligns parallel to the solid surfaces evidenced by the positioning of all microgels in the focal plane in panels B1 and B2. As the level of water lowers further (panels B-D), the color of the core region (i.e., silica core plus swollen microgel around it) becomes increasingly distinct from the rest, signifying different surface elevations. On hydrophilic substrates, regions with low microgel concentration (empty areas) grow in size as the drying proceeds (hereinafter called hole formation, see Figure 6.2, panels C1-E1), pushing the microgels against each other until the films completely dries (Figure 6.2, panel F1). This hole formation appears to be largely influenced by the fluid dynamics, as evidenced by the circular shape of the enlarging holes, which are also observed for both micron-sized hard sphere-like systems [210] and microgel systems. [161] Remarkably, the microgel migrations (hereinafter called XY displacement) are negligible when the drying takes place on hydrophobic substrates (Figure 6.2, panels C2-F2). The characterization is repeated at different values of Π. The corresponding microscopy images are depicted in Figure 6.12 in SI. We quantify the effect of water evaporation on the microgel films by measuring $D_{\text{c-c}}$ before and after the drying (Figure 6.13 in SI). Note that $D_{\text{c-c}}$ changes significantly when the underlying substrate is hydrophilic.

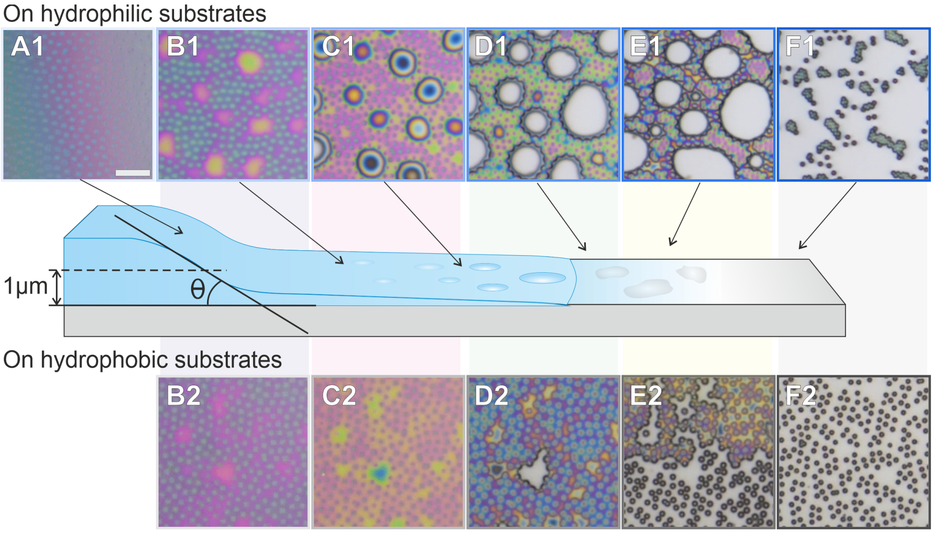

Fig. 6.2 Sketch illustrating the drying of microgel films and reflected light microscopy images of $C_{437}S_{2.3}$-2.5 films at $\Pi \approx 20$ mN/m transferred onto hydrophilic (A1-F1) and hydrophobic substrates (B2-F2). The colors are due to thin-film interference and will be later used to determine the local height. The scale bar corresponds to 5 μm. θ is the receding wetting angle of the meniscus.

We take a further step to characterize the drying of soft films and compare two CS microgels with different crosslinker—*N*,*N'*-methylenebisacrylamide (BIS)—densities. Figure 6.3 illustrates different stages of the drying process of $C_{437}S_{2.6}$-1.0 and $C_{437}S_{2.4}$-7.5 microgel films at mid Π. For "softer" and thus more deformable microgels ($C_{437}S_{2.6}$-1.0, Figure 6.3, panels A-D), the surface chemistry of the substrate has minimal to no influence on the spatial rearrangement upon drying, i.e., no XY displacement. Significant microstructural changes, to the degree reported in panels A1-F1 of Figure 6.1 ($C_{437}S_{2.3}$-2.5 films), only occur at high Π on hydrophilic surfaces (Figure 5.16 in SI). Conversely, microgels with "harder", more elastic shells ($C_{437}S_{2.4}$-7.5, Figure 6.3E-H) undergo significant XY displacement as they dry onto either of the two substrates. In particular, an abrupt and sudden collapse of microgels (i.e., a fast and large hole formation) is observed when the film dries onto hydrophilic substrates and the thin layer of fluid reaches a critical thickness. On the other hand, on hydrophobic substrates, they tend to lean and/or slide towards one another, creating maze-looking grain boundary-like cracks. In analogy to Figure 6.12 and 6.13 in SI, we also report microscopic images and $D_{\text{c-c}}$ for different Π values, as depicted in Figure 6.14-6.16 in SI. Similar behaviors were observed for coreless PNIPAM microgels of comparable sizes (Figure 6.17, 6.18 in SI) as well as for smaller CS microgels (Figure 6.19 in SI) at a mid-high Π regime.

6.3 Discussion

Predicting how soft interfacial films dry onto solid substrates is far from trivial. In our model system consisting of microgel-laden interfaces transferred onto solid substrates, a rich drying scenario emerged depending on (1) the wettability of the substrate, (2) the elasticity of the individual microgels, and (3) the surface pressure of the microgel-laden interface. We adjusted these parameters by (1) functionalizing the solid surface, (2) tuning the amount of crosslinker during microgel synthesis and (3) compressing the interface. To elucidate the physical phenomena that occur during the drying of such films, we first illustrate microgels deformed at air/water interface for "softer" and "harder" CS microgels, as depicted in Figure 6.4 panels A1 and B1, respectively. Note, however, that the "softness" of microgels at the air/water interface is ill-defined due to the lateral deformation (see e.g., Figure 6.1) caused by interfacial tension, leading to non-isotropic softness within the polymeric network: the portion at the interface (denoted as I-part, Figure 6.4 panels A1, B1) experiences more stretching than the portion in the bulk (B-part). [141] Additionally, the crosslinker density is not homogeneous within the shell, being higher near the core and lower in the outer layer. Nevertheless, the primary determinant of the "softness" of microgel is known to

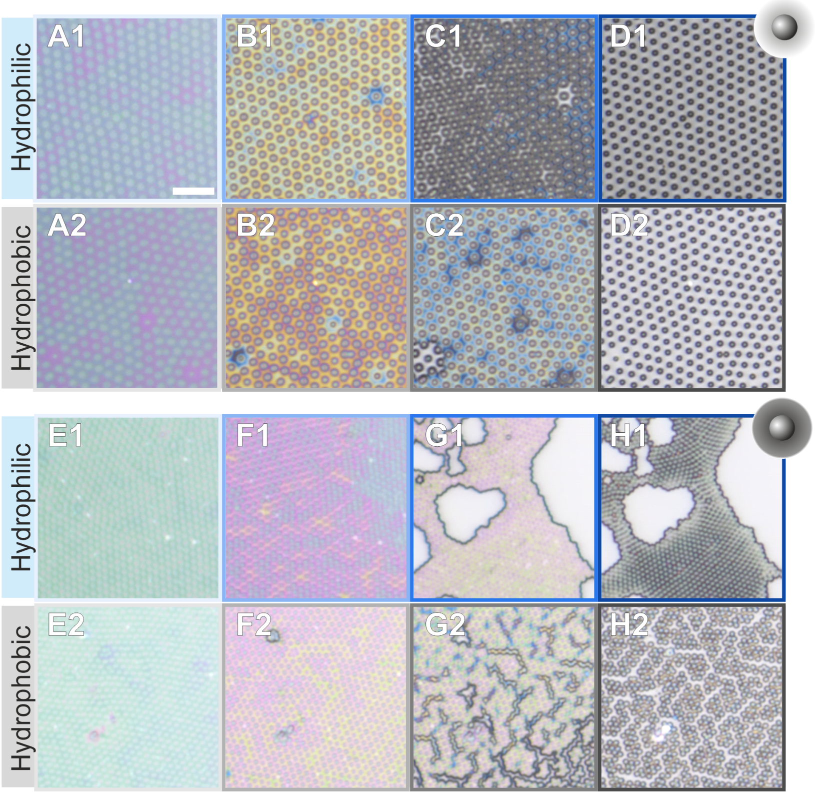

Fig. 6.3 Reflected light microscopy images of $C_{437}S_{2.6}$-1.0 (A-D) and $C_{437}S_{2.4}$-7.5 microgel films (E-H) at mid Π (near 20 mN/m) transferred onto hydrophilic (A1-D1, E1-H1) and hydrophobic substrates (A2-D2, E2-H1). The scale bar corresponds to 5μm. The sketches of CS microgels on the top right corner of panels visually show that they have the same core but shells with different crosslinker densities.

be the crosslinker density. [172] In this work, we qualitatively use the word 'softness' to describe the ability of the polymer shell to deform and stretch. As water evaporates from the thin fluid layer (see e.g., Figure 6.1, panels C-D), the bottom B-part of the shells come in contact with the underlying substrate (S-part, Figure 6.4 panels A2, B2). If the resulting adhesion is not strong enough to resist the de-wetting of water, microgels migrate (hole formation) and collapse (see e.g., Figure 6.1, panels D1, H1). If the adhesion is strong enough, microgels stay in position in the thin water film, where the meniscus slope angle (Ψ) and microgel-to-substrate contact area (colored orange) increase while the average film thickness decreases as the drying proceeds. At the same $D_{\text{c-c}}$ and a given film height ($D_\text{h} < H < D_\text{c}$), the harder microgels will be under a stronger immersion capillary force due to the steeper meniscus slope angle ($\Psi_\text{harder} > \Psi_\text{softer}$) and have weaker microgel-to-substrate adhesion (i.e., smaller contact area) due to high elasticity of the polymer network. At a critical height (H^*), the immersion capillary force can surpass the microgel-to-substrate adhesion, causing the microgels to collapse onto one another (Figure 6.4 panel B3), i.e., the gradual decrease in $D_{\text{c-c}}$ as the effective volume of microgel reduces due to evaporating water. If the adhesion persists stronger than the acting immersion capillary force, the migration of microgels do not occur (Figure 6.4 panel A3, no XY displacement) and the microstructure of the microgel-laden interface is preserved, unless the higher center part of microgels tilt/lean towards one another. Therefore, if the goal is to produce dried replicas of the interfacial microstructure, soft microgels with hydrophobic (or oppositely charged) substrates are to be used rather than hard microgels with hydrophilic substrate.

6.3.1 Wettability of the substrate

Using a combination of 3D superresolution fluorescence microscopy and dissipative particle dynamics, Hoppe Alvarez et al. [77, 204] and Shaulli et al. [217] have demonstrated that poly(*N*-isopropylmethacrylamide) microgels maintain their native spherical shapes at the interface of a buffer solution and hydrophilic substrates. In stark contrast, at the buffer solution/hydrophobic substrate interface (high surface energy), the same microgels undergo significant deformation, creating larger contact area between the microgels and the substrate. This is attributed to the fact that the interaction between the hydrophobic surface and the amphiphilic polymer chains is more energetically favorable compared to that with water molecules. This leads to both stronger microgel-to-substrate adhesion (higher microgel deformation) and weaker immersion capillary attractions (lower microgel height), resulting in restricted mobility of the microgels during the drying. We recreated the contact scenarios between the microgel-laden interfaces and solid substrates using a modified thin film pressure balance (TFPB) equipped with a porous silica plate connected to a capillary tube filled with

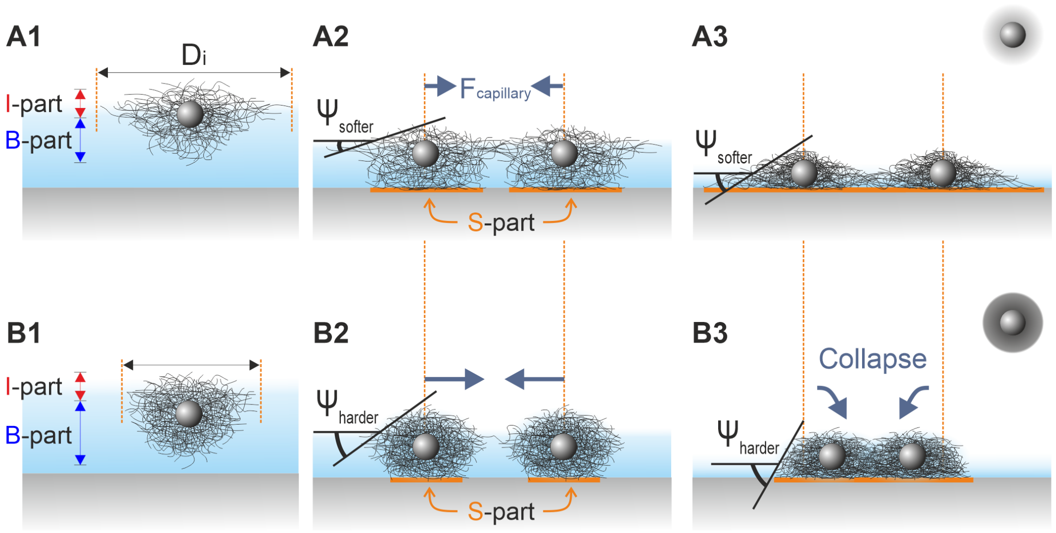

Fig. 6.4 Schematic illustration of microgels at the air/water interface and their interfacial diameter, D_i, for CS microgels with a lower (A1) and higher crosslinker density (B1). At the same $D_{c\text{-}c}$ and a given film height ($D_h < H < D_c$), softer microgels have larger contact area to the substrate and lower meniscus slope angle (Ψ_{softer}, A2) compared to harder microgels (Ψ_{harder}, B2), and thus more likely to stay in position (A3) than to collapse (B3).

water (Figure 6.5A and Figure 6.20 in SI). [216] The silica plate is soaked with water and has a truncated hole, where the air/water interface is created on the top and the substrate is placed on the bottom. By modulating the air pressure in the pressure port, the setup enables the on-demand position control of the microgel-laden interface between far from the solid substrate (Figure 6.5B) and close, where microgels are trapped in the thin film on the substrate (Figure 6.5C) and iridescent colors from thin film interference are observed. More details can be found in the Experimental Section. Microgels, once trapped in the thin fluid film, can be released back to the air/water interface on demand (see Video in SI), provided that the underlying substrate is hydrophilic, i.e., when microgel-to-substrate adhesion is weak. In stark contrast, the TFPB experiment conducted on hydrophobic substrates revealed that the on-demand trapping of the microgel monolayers in the thin film is not achievable on hydrophobic substrates. When attempted, it only resulted in multilayers, see Figure 6.21 in SI. This spontaneous and favored adsorption of microgels from the water phase to a hydrophobic substrate was also reported in the drying experiment on microgel-laden droplets. [218]

We further verified the drying scenarios of microgel-laden interfaces through molecular dynamics simulations. Specifically, we constructed a system based on experimental results in which 16 CS microgels were positioned at the air/liquid interface on differently modified substrates (hydrophobic vs. hydrophilic) during a continuous water evaporation process, as illustrated in Figure 6.6 (panels A-E), analogous to Figure 6.2. More details on simulation

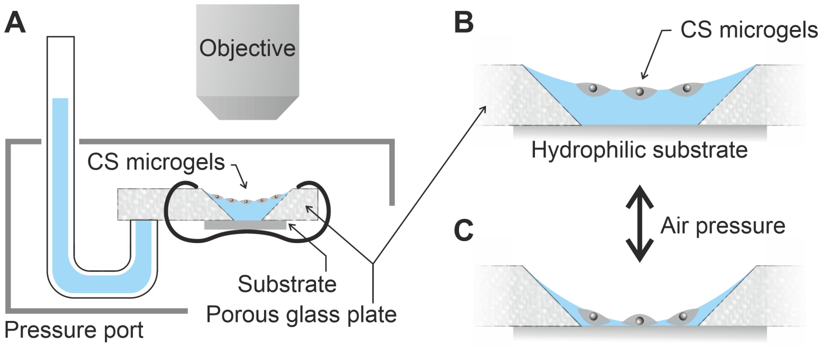

Fig. 6.5 Schematic illustration of modified thin film pressure balance setup (A) and the microgel-laden interface oscillation experiment by pressure modulation on the hydrophilic: between air/water interface (B) and in the thin film on the substrate (C). The video of $C_{437}S_{2.3}$-2.5 film is provided in SI.

parameters can be found in SI. It is important to note that the evaporation of water from the interface is not uniform. The most rapid drying occurs in the regions between the microgels, where lower density of the polymer enables efficient evaporation. This asymmetry results in the formation of a drying front (hole formation), prompting XY displacement of microgels. The simulation results show that the mobility of the microgels on the hydrophobic substrate is reduced (Figure 6.6, panels A2-E2), as also corroborated by a higher $D_{\text{c-c}}$ value and the distribution of the microgels in the dried layer, as detailed in Table 6.2 in SI. However, it is evident that the microgel-to-substrate adhesion is insufficient to prevent XY displacement in both cases. This might be due to the fact that the experimental scenarios are far out-of-equilibrium state, closer to the interaction between the dried polymer and substrate, whereas in simulation is conducted near equilibrium. Nevertheless, shape and size transformation of the microgels during the drying illustrated by the simulation are in line with our understanding (Figure 6.4, panels B1-B3). Figure 6.2 illustrates the microgel deformation at the air/water interface (panels A,A1) and varying extent of microgel spreading on hydrophilic (higher, panels B,B1) and on hydrophobic substrates (lower, panels C,C1). Additionally, a longer equilibration time resulted in an increase in the contact area between the microgel and the hydrophobic substrate, whereas it remained minimal for the hydrophilic substrate (Figure 6.24 in SI), indicating that the drying condition such as surrounding temperature and humidity can influence the outcome of the drying.

6.3.2 Softness of microgels

For a more quantitative validation, we measure H^* corresponding to the onset of XY-displacements of the microgel particles (if any) after the formation of a thin fluid layer.

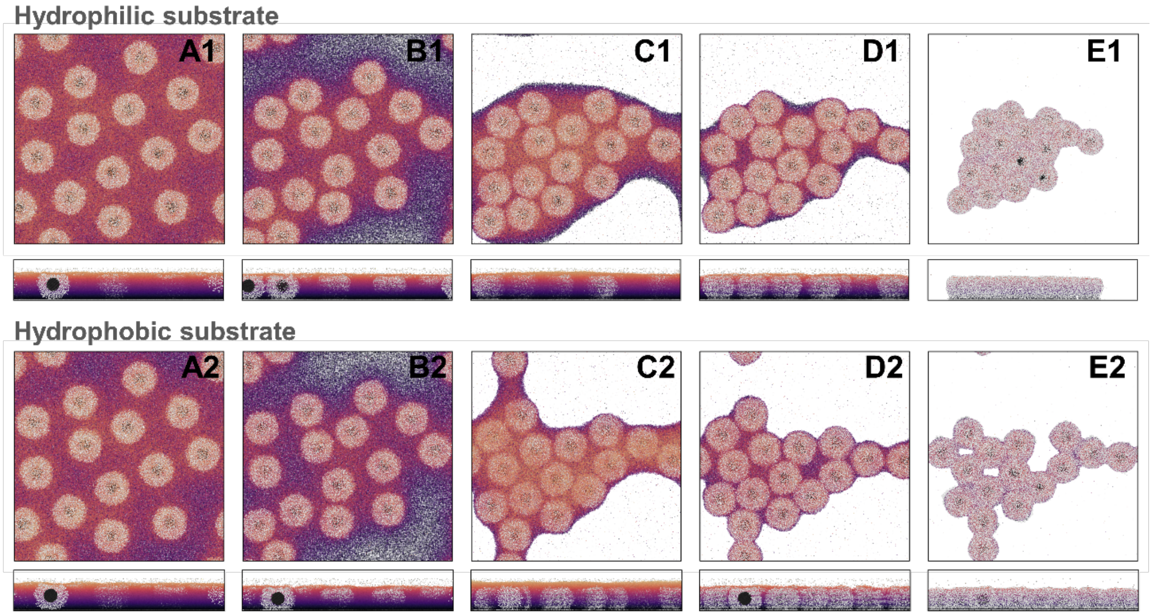

Fig. 6.6 Illustration of the different stages of microgel film drying on hydrophilic (A1-E1) and hydrophobic (A2-E2) substrates. The narrow panels below are cross-sections of each panel.

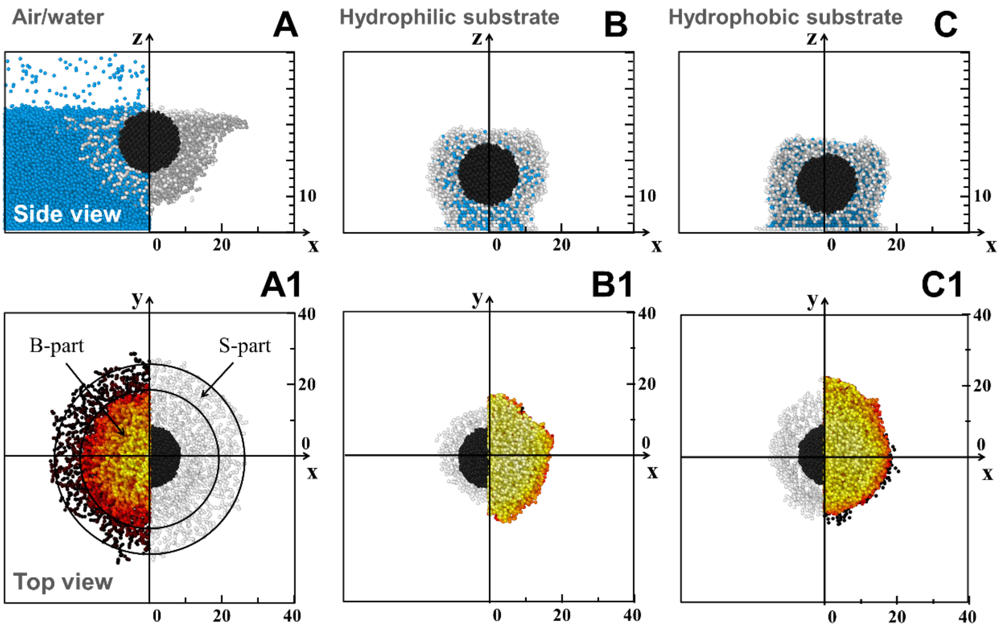

Fig. 6.7 Illustration of the allocated CS microgel structure in the monolayer before (A,A1) and after drying on hydrophobic (B,B1) and hydrophobic substrates (C,C1).

We consider interfaces filled with CS microgel of different softness ($C_{437}S_{2.6}$-1.0, $C_{437}S_{2.3}$-2.5, and $C_{437}S_{2.4}$-7.5) at a comparable $D_{\text{c-c}}$ ($\approx$ 840 nm, at the water-air interface), and extract the instantaneous velocity V of the particles (i.e., the displacement of the core's center between consecutive frames) and the height of the microgel film as it dries. The height profiles of the drying films were traced by their apparent colors, which stem from thin film interference, [216, 136] under the assumption that the interface is perfectly flat and the refractive index of the thin film equals that of water throughout the drying process. However, it is important to note that as the drying progresses, the height profiles will be increasingly underestimated due to the increasing effective refractive index of the film (increasing polymer volume fraction). Furthermore, higher refractive index and spherical shape of silica cores introduce further complexity. To simplify the calculation, we masked the core areas (arbitrarily determined, approximately 600 nm in diameter) and only considered the height of the shell area (H in Figure 6.8A) for radial averaging. $H = H^*$, when the microgels start to move from their original XY-position. The methodology is described in detail in the Experimental Section.

Figure 6.8 (panels B-D) shows the evolution of the height profiles of microgel-laden interfaces drying on hydrophilic (blue) and hydrophobic (grey) substrates as a function of a normalized time, where $t = 0$ is the onset of XY-displacement of the individual microgels. The corresponding instantaneous velocities are in Figure 6.22 in SI. All height profiles exhibit plateau regions near $H = D_{\text{c}}$, possibly due to the combination of: 1) the elasticity of the microgel networks supported by the core, 2) increased polymer volume fraction, 3) artefact of radial averaging (due to the changes in Ψ as the drying proceeds). Notably, the height of the microgel films is generally higher on hydrophilic substrates compared to hydrophobic substrates because of the stronger microgel-to-substrate adhesion and more pronounced deformations of the polymer networks in contact with the solid surface (see Figure 6.4). The critical height H^* is also consistently higher for interfaces made of microgels with more elastic shells, as illustrated in Figure 6.8 (panels B-D) and Table 6.1. The high elasticity of the polymer network appears to resist the thinning of the film, which could also result in a relatively smaller contact area with the substrate and, consequently, weaker microgel-to-substrate adhesion and higher mobility during drying. The difference in softness among CS microgels is also evident in the lateral deformation rate at the air/water interface in Figure 6.1, Figure 6.9, and Table 6.1. Our results indicate that the drying of a microgel film involves an intricate interplay among various factors, such as microgel-to-substrate adhesion, microgel compression state, immersion capillary forces, free energy associated with interface formation, drying conditions and others. Further quantification of the phenomena requires values of the slope angle of the meniscus and microgel adhesion both of which will change as the drying progresses.

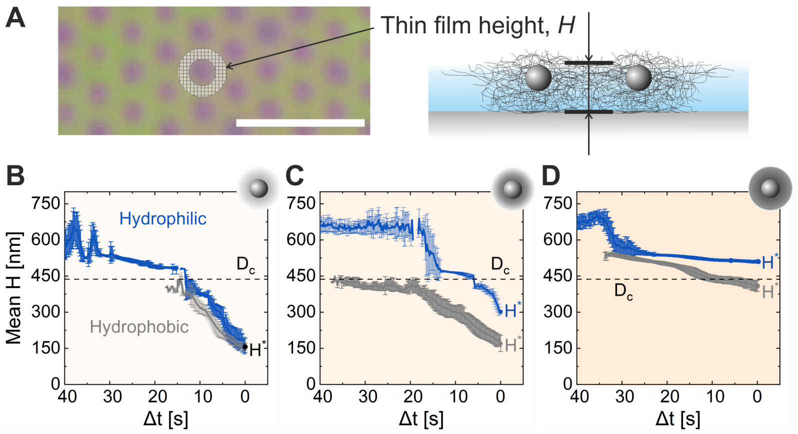

Fig. 6.8 Film height, *H*, shown in an exemplary frame (A, left) and in a sketch (B, right). Evolution of the height profiles of 10 randomly chosen CS microgels in corresponding films drying on the hydrophilic (blue) and hydrophobic (grey) substrates for $C_{437}S_{2.6}$-1.0 (B), $C_{437}S_{2.3}$-2.5 (C), and $C_{437}S_{2.4}$-7.5 (D).

6.4 Conclusion

Interparticle interactions among soft colloids and their phase behavior at interfaces are of great importance in fundamental colloid and interface science. Studying such phenomena at interfaces, however, is challenging due to the difficulty in visualization of the subject matter as well as the deformed interface, particularly in condensed (or highly compressed) states. The present work visualized and quantified the drying process of the microgel monolayers on various solid substrates at a single microgel level, which is crucial for applications of such “2D” microstructures created via fluid interface-assisted assembly. Using variously crosslinked CS microgels, we demonstrated that the resulting microstructure of the microgel monolayers is significantly influenced by the elasticity of the microgels and the wettability of the substrates. In general, CS microgels with lower elasticity better maintain the assembled structure due to higher deformation at the interfaces. This results in stronger adhesion to the substrate and, consequently, lower mobility during the drying process.

We experimentally showed that the drying dynamics of such monolayers involve an intricate interplay among various factors, including microgel-to-substrate adhesion, immersion capillary forces, and the free energy associated with interface formation. Our results find support in molecular dynamics simulations, where the hole formation and microgels’ varying degree of deformation on differently surface-modified substrates are visualized. This implies that the interpretation of the "2D" assembly of soft colloids at interfaces must consider the often-overlooked 3D aspects, as also highlighted in a recent study on emulsion stabilization by microgels. [219] While the presence of the core increases the operative immersion capillary force and may influence the shell's elasticity, when trapped in thin liquid films (i.e., during drying on a substrate), the deformation of the interface is inevitable, even for submicron-sized microgels without cores. The system will then react on the microgels to minimize the surface energy configuration. [220] Therefore interpreting *ex situ* results, i.e., data obtained after transfer onto a substrate, should be approached with caution.

To date, there is no generally accepted model for the interactions among soft colloids at interfaces bridging from dilute to condensed (compressed) state. In future investigations, it would be intriguing to explore the interparticle interactions of these soft colloids, especially at the single colloid level, using techniques such as optical tweezers. Such endeavors have the potential to enhance our understanding of the complex phase and rheological behaviors exhibited by these soft colloids. Furthermore, for applications where solid support is required, it could be interesting to explore the influence of varying surface roughness or porosity and to measure microgel-to-substrate adhesion forces, possibly using (polymer shell coated) colloidal atomic force microscopy probes in an aqueous environment.

6.5 Experimental section

6.5.1 Materials

Ethanol (Sigma-Aldrich, 99.8%), ethanol (Heinrich-Heine-University, chemical store, p.a.), tetraethyl orthosilicate (TEOS, Sigma-Aldrich, 98%), ammonium hydroxide solution (NH_3 (aq.), VWR, 25%), ammonium hydroxide solution (NH_3 (aq.), PanReac AppliChem, 30%), hydrogen peroxide solution (H_2O_2, Fisher Chemical, 30 wt %), methacryloxyethyl thiocarbamoyl rhodamine B (MRB, Polysciences, Inc.), 3-aminopropyltrimethoxysilane (APS, Sigma-Aldrich, 97%), rhodamine B isothiocyanate (Sigma-Aldrich, mixed isomers), 1H,1H,2H,2H-perfluoroctyltriethoxysilan (PFOES, J&K Scientific, 97%) 3-(trimethoxysilyl)propyl methacrylate (MPS, Sigma-Aldrich, 98%), *N*,*N*'-methylenebisacrylamide (BIS, Sigma-Aldrich, 98%), and potassium peroxodisulfate (KPS, Sigma-Aldrich, 99%) were used as received. Water was purified by a Milli-Q system (18.2 $M\Omega \cdot cm$) and *N*-isopropylacrylamide (NIPAM, TCI, 97%) by recrystallization from cyclohexane (Fisher Scientific, 99.8%).

6.5.2 Synthesis

The synthesis of CS microgels was done via seeded precipitation polymerization. The synthesis protocols of the micron-sized CS microgels are detailed elsewhere. [23] The coreless microgels were synthesized via precipitation polymerization according to previously published work. [65, 66] The synthesis protocols were modified for dye incorporation for sMG (Figure 6.17) as described in [30] as well as for lMG (Figure 6.18). lMG was synthesized with 2.11 g of PNIPAM and 60 mg of BIS (2 mol.%), dissolved in 125 ml of water. The mixture was injected through a 0.2 μm Nylon syringe filter into a three-neck round-bottom flask equipped with a reflux condenser and a magnetic stirrer. 250 μL of MRB dye aq. solution (1 mg/ml) was added to the flask. The mixture was heated to 45°C and equilibrated for an hour while purged with nitrogen under stirring. 0.1054g KPS in 5 ml water was added to the flask through a 0.2 μm Nylon syringe filter. After initiation, the temperature was ramped up to 65°C in 40 minutes. The reaction was kept overnight under stirring at 65°C. The dispersion was then filtered through glass wool. The synthesized PNIPAM microgels were dialyzed against water for two weeks, freeze-dried, and re-dispersed in ethanol (1 w/v%).

6.6 Methods

6.6.1 Dynamic light scattering (DLS)

he hydrodynamic diameter, D_h, of the CS microgels was measured using a Zetasizer Nano S (Malvern Panalytical). The device is equipped with a HeNe laser (4 mW, 633 nm) and a temperature-controlled jacket. Measurements were performed at a scattering angle of 173°at 20°C. Three measurements were performed. Values of D_h reported are averaged from the z-averages obtained from the measurement software.

6.6.2 Glass substrate surface modification and contact angle measurement

For the preparation of glass substrate with a hydrophilic surface, standard microscope glass slides were thoroughly cleaned and rinsed using water and ethanol, and then plasma-treated prior to the monolayer transfer. For the hydrophobic surface modification, the glass substrates were RCA cleaned [179, 180] and surface-modified via chemical vapor deposition. 200 μl of PFOES was stored with the cleaned glass substrates in a desiccator overnight under vacuum (25-30 mbar). The glass substrates were then placed in an oven at 120°C for an hour to ensure covalent bonding and washed in ethanol in an ultrasonic bath to remove unreacted silane molecules. The contact angle with 5 μl water droplet was measured by a drop shape analyzer (DSA100E, Krüss) at room temperature (25.5-26.6°C, relative humidity 35-46%).

6.6.3 *In situ* monolayer drying via light and fluorescence microscopy

The transfer of the CS microgel monolayer on the two differently modified substrates was carried out using a Langmuir-Blodgett deposition trough (Microtrough G2, Kibron Inc.) equipped with a film balance, two Delrin barriers, a dip coater, and an acrylic cover box. The monolayer deposition was done rapidly maintaining the measured surface pressure (surface pressure changed during the transfer:1.4 ± 1.1 mN/m, compression speed: 187 mm/min, deeper speed: 279 mm/min) positioned at 90°to the air/water interface and parallel to the barriers. The "wet" monolayer on the glass slide was then placed under a light microscope (Eclipse LV150N, Nikon) equipped with a 100× objective for the *in situ* monitoring of the drying monolayer. Coreless microgels were investigated under a fluorescence microscope (Olympus IX73) equipped with a mercury lamp, a fluorescence filter set, a CMOS camera, and a 60× objective.

6.6.4 *In situ* monolayer drying via confocal laser scanning microscopy

XZ *in situ* time series scans of the drying CS microgel monolayers were acquired using a Zeiss inverted LSM880 Airyscan microscope system (Zeiss Microscopy GmbH, Oberkochen, Germany), equipped with a Plan-Apochromat 40x/0.95 dry objective lens. Microgel monolayers were prepared as described at the air/water interface in a crystallizing dish and transferred on cover glasses as described in [23] and were mounted immediately on the microscope motorized stage. The time series scans were started in regions that were visibly not in the dried state. Two simultaneous acquired channels were set up in fluorescence and reflective mode to observe the Rhodamine B labeled silica cores in the monolayer and their distance to the cover glass and the water meniscus, respectively. 561 nm was used at 3% intensity as an excitation laser line with a PMT detector set at a range of 580-670 nm for the acquisition of the fluorescence. For simultaneous acquisition of the laser reflection, another GaAsP detector was set at a range of 540-580 nm overlapping with the 561nm excitation laser line. The general acquisition parameters were set as the following. The calculated pinhole size was used at 0.44 airy units. The x-axis pixel size was set to 208 nm at a total scan length of 213 μm. The z-axis covered a range of 49 μm as 100 slices with an interval of 492 nm. The scans were performed in line scan fast Z mode at a scan speed of 2.05 μsec/pixel resulting in an average framerate of 1.08 s/frame.

6.6.5 Monolayer oscillation experiment with thin film pressure balance

To investigate the adsorption and desorption of microgel monolayers at the water/substrate interface, a custom-built thin film pressure balance (TFPB) using the porous glass plate method [221, 222] in wetting configuration [223] was used at 22°C. The porous glass plate is attached to a glass capillary tube (film holder), which is filled with water in a way that the water can travel from the porous glass plate to the capillary tube and vice versa. The substrate of interest (various hydrophilic glasses, silicon wafers, and hydrophobic glass) is placed underneath a hole of 1 mm in diameter in the porous glass plate (pore size 10-16 μm, porosity P16 (ISO 4793)) and fixed with a stainless-steel clamp, as shown in Figure 6.20A. The monolayers were prepared as for the confocal microscopy using the whole film holder with the clamped substrate submerged before injecting certain volumes of microgel ethanolic dispersion at the air/water interface, which corresponds to a surface pressure of approx. 20 mN/m. The film holder is placed in a sealed stainless-steel pressure chamber with a quartz glass window for the imaging, as shown in Figure 6.20B. The area of interest is illuminated by a cold-filtered halogen lamp through the reflective light microscope optics and imaged by a color CMOS camera (JAI Go-2400-USB, pixel size: 5.86 μm × 5.86 μm, Stemmer Imaging Puchheim, Germany). In combination with the optics (reflected light microscope, extension tube), the resolution of the camera system is 1.72 pixel μm^{-1}.

6.6.6 Microgel monolayer thickness calculation based on wetting film color simulation

The microgel monolayers under light microscopy start to appear colorful due to interference effects when the microgel monolayer-to-substrate distance lowers below 1 μm. A model color spectrum was simulated with an algorithm based on a water slab covering a reflective surface (modified from the free-standing water slab color simulation in [216, 136]). The spectrum is represented in the hue, saturation, and value (HSV) color space, and is stored in thickness steps of 1 nm in a lookup table. Each film thickness in the range from 100 to 1000 nm has a corresponding set of unambiguous HSV values. Pixel by pixel the hue values of the film image are automatically compared with the lookup table and the corresponding film thickness for each pixel is the result. The height of their shell's shoulder (H, Figure 6.8A) was traced as the thin fluid layer dries. For each image and each particle, H is calculated using the average color of a circular region around the core, stemming from thin film interference (note that the areas occupied with the cores themselves are excluded from the analysis).

6.6.7 Particle tracking

The detection of the onset of the XY displacement was achieved via particle tracking of the individual microgels in terms of velocity. The averaged velocity over all microgels in the frames does not allow for the precise detection of the onset of the XY displacement because the length and height of the microgel thin film varies in all cases, leading to many frames containing both swollen and collapsed CS microgels in varying ratios. Consequently, 10 CS microgels were randomly selected for analysis.

6.7 Supporting Information

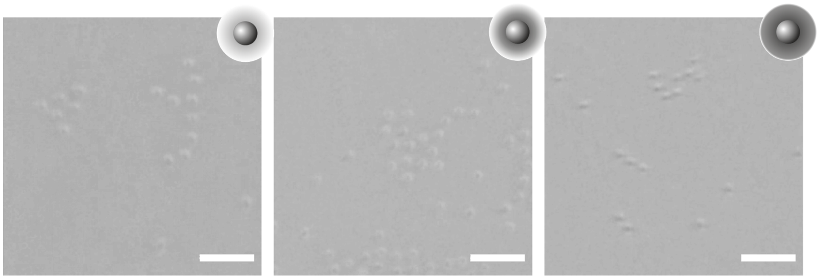

Fig. 6.9 Reflected light microscopy images of $C_{437}S_{2.6}$-1.0, $C_{437}S_{2.3}$-2.5, and $C_{437}S_{2.4}$-7.5 at the air/water interface at 0 mN/m. At least 200 microgels were used for the acquisition of the mean nearest center-to-center distance, $D_{\text{c-c}}$, in Figure 6.1.

Table 6.1 The critical height, H^*, of CS microgels at the water/solid interface and deformation rate at the air/water interface.

	Water/solid interface				Air/water interface	
	Hydrophilic		Hydrophobic		*Ethanolic	**Aqueous
	H^* [nm]	H^*/D_h	H^* [nm]	H^*/D_h	Deformation degree (D_i/D_h)	
$C_{437}S_{2.6}$-1.0	159 ± 35	15.8%	157 ± 14	15.6%	170.5%	174.5%
$C_{437}S_{2.3}$-2.5	301 ± 6	27.0%	169 ± 33	15.1%	133.7%	136.4%
$C_{437}S_{2.4}$-7.5	511 ± 6	48.6%	409 ± 23	38.8%	109.2%	109.2%

Fig. 6.10 *In situ* monitoring of the drying $C_{437}S_{2.3}$-2.5 film on the hydrophilic substrates via confocal microscopy. A-C depict the lowering of the monolayer (upper line, dots are rhodamine B dyed core) to the substrate (lower line). D shows the interference pattern that arises from the slope of the meniscus (in the red box with a dotted line) and the monolayer thin film on the left. E shows the drying front of the microgel monolayer indicated by the higher intensity of the dried monolayer. The scale bar corresponds to 20 μm.

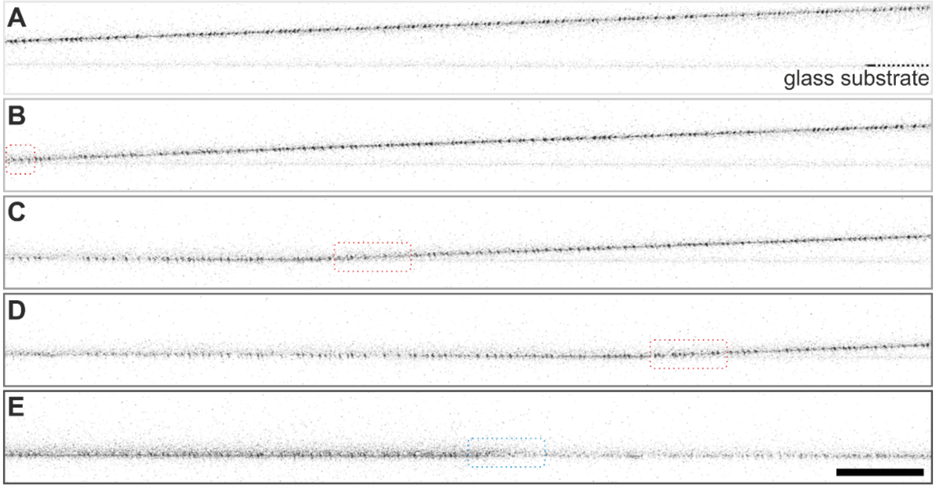

Fig. 6.11 *In situ* monitoring of the drying $C_{437}S_{2.3}$-2.5 film on the hydrophobic substrate via confocal microscopy. A and B depict the lowering of the monolayer to the substrate. B and C show the beginning of the monolayer thin film. E shows the drying front of the microgel monolayer indicated by the higher intensity of the dried monolayer. The scale bar corresponds to 20 μm.

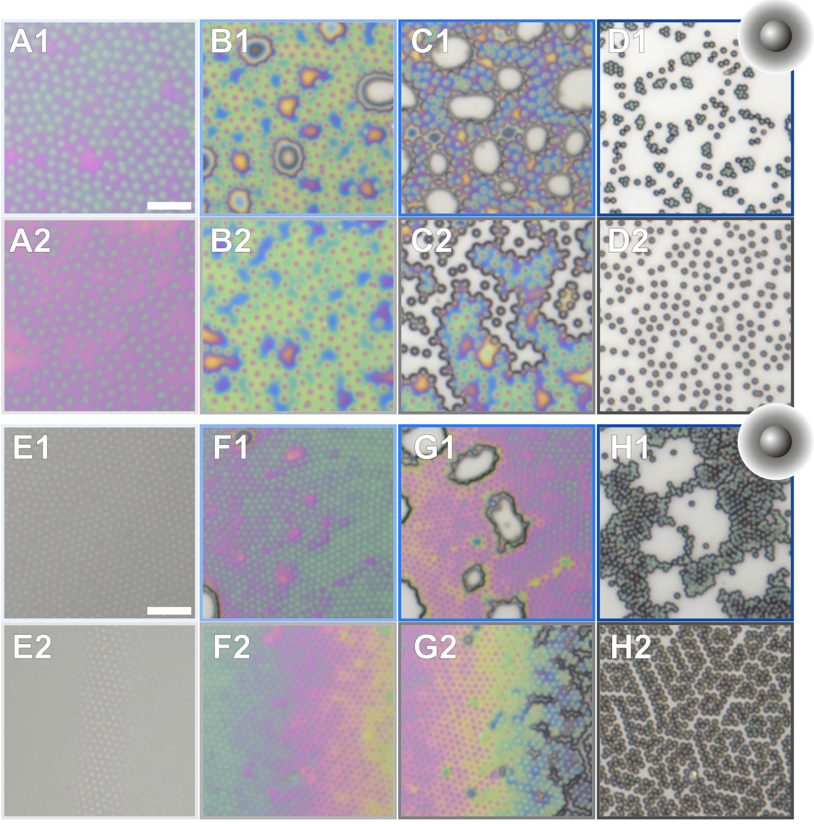

Fig. 6.12 *In situ* monitoring of the drying of $C_{437}S_{2.3}$-2.5 film, transferred from Π near 10 mN/m, drying on hydrophilic (A1-D1) and on hydrophobic substrates (A2-D2). (E1-H2) are the same data sets for the microgel film transferred from Π near 30 mN/m. The scale bars correspond to 5 μm.

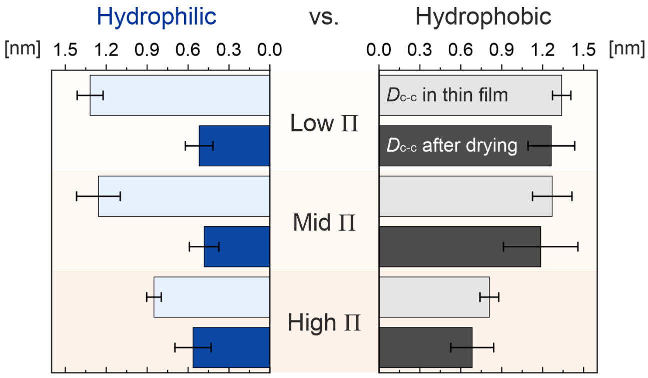

Fig. 6.13 Center-to-center distance, $D_{\text{c-c}}$, of $C_{437}S_{2.3}$-2.5 film drying onto hydrophilic (blue) and hydrophobic (gray) substrates. Distances in thin film are shown using lighter colors and compared to the ones of fully dried microgel clusters (darker colors). The error bars are the standard deviations of the first peaks of the radial distribution functions.

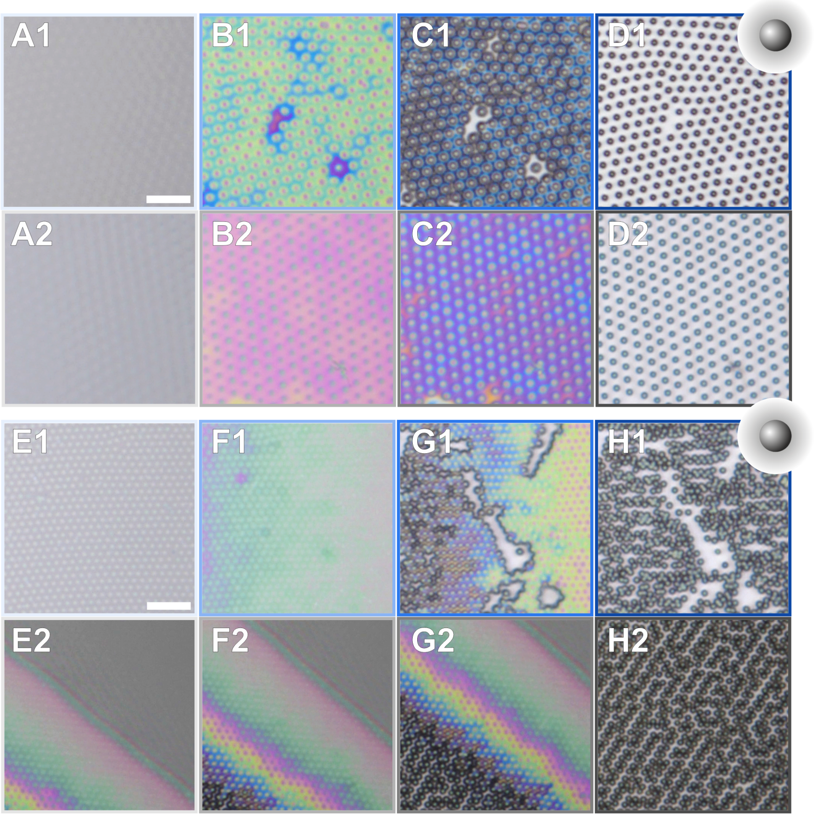

Fig. 6.14 *In situ* monitoring of the monolayer of $C_{437}S_{2.6}$-1.0 transferred from Π near 10 mN/m, drying on A1-D1) hydrophilic and on A2-D2) hydrophobic substrates. E1-H2) are the same sets of data for the monolayer transferred from Π near 30 mN/m. The scale bars correspond to 5 μm.

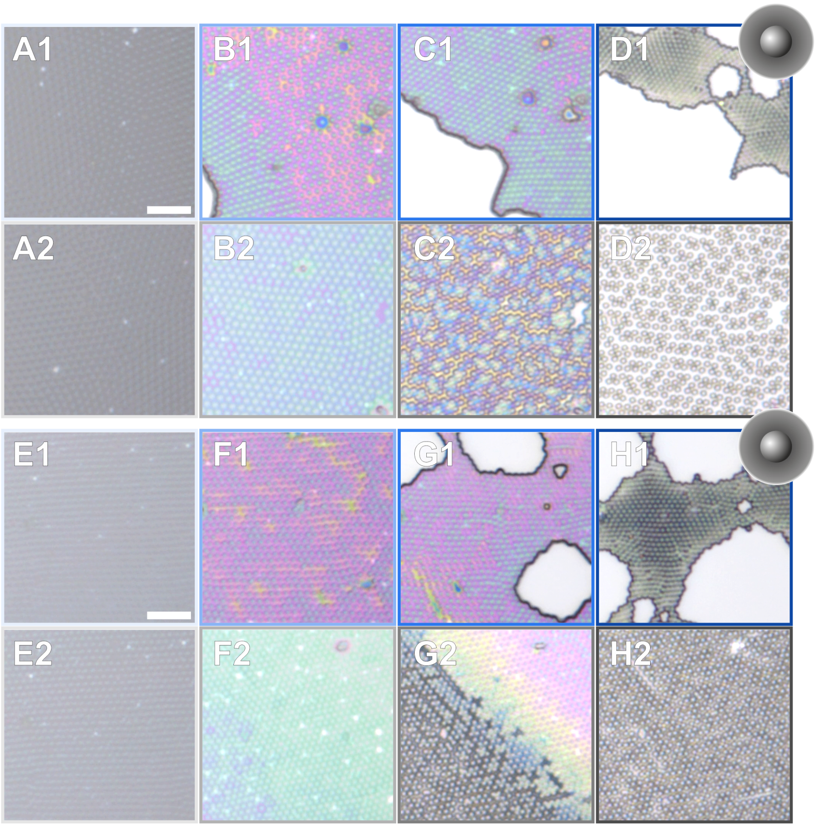

Fig. 6.15 *In situ* monitoring of the monolayer of $C_{437}S_{2.4}$-7.5 transferred from Π near 10 mN/m, drying on A1-D1) hydrophilic and on A2-D2) hydrophobic substrates. E1-H2) are the same sets of data for the monolayer transferred from Π near 30 mN/m. The scale bars correspond to 5 μm.

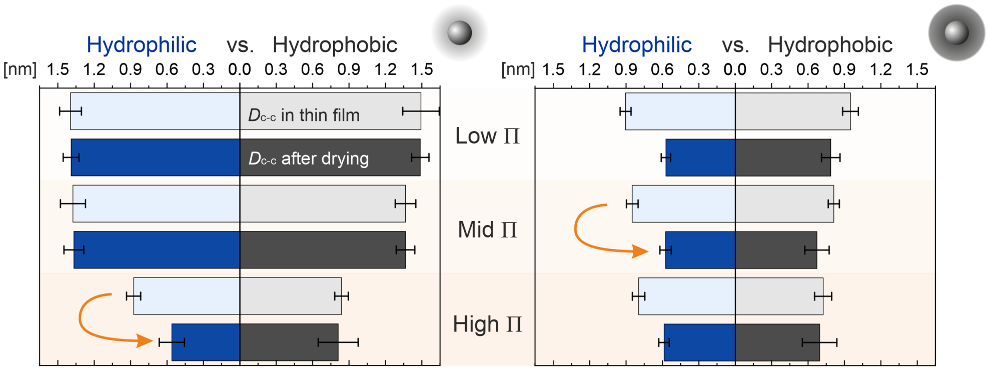

Fig. 6.16 Center-to-center distance, $D_{c\text{-}c}$, of $C_{437}S_{2.6}$-1.0 and $C_{437}S_{2.4}$-7.5. films drying on hydrophilic (blue) and hydrophobic substrates (gray) in the thin fluid film (lighter color), as compared to that of dried monolayer (darker color).

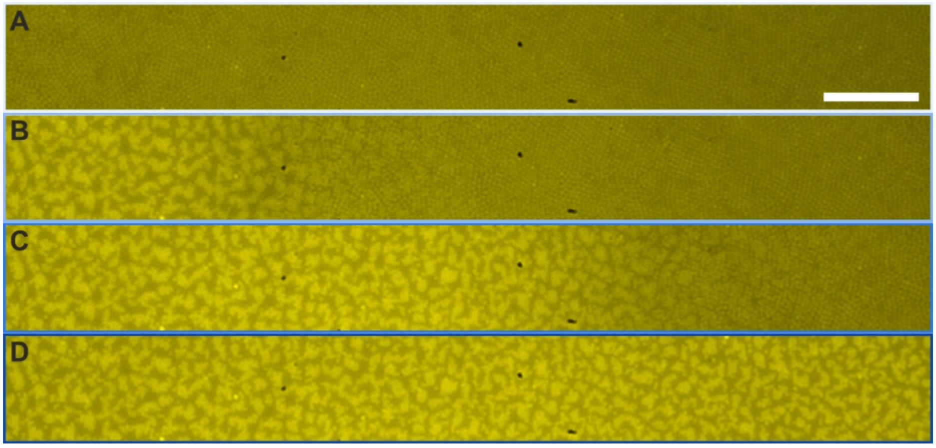

Fig. 6.17 Drying of coreless PNIAPM microgel (sMG, $D_\mathrm{h} \approx 800$ nm) film via fluorescence microscopy, scale bar corresponds to 20 μm.

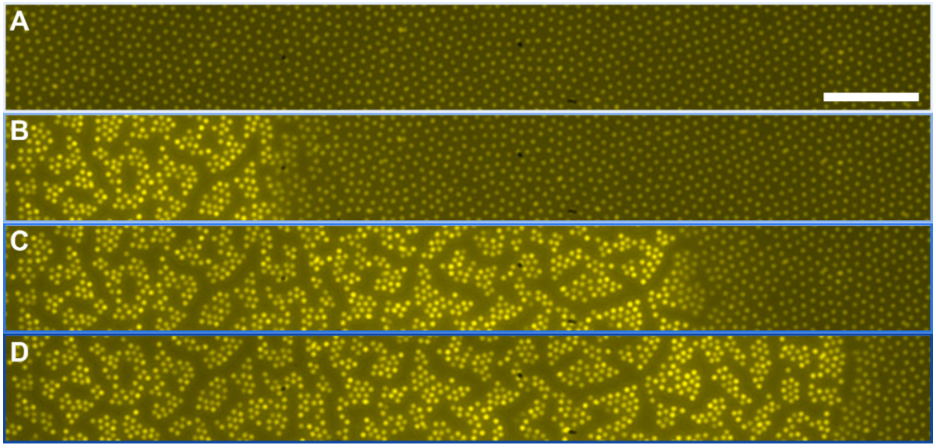

Fig. 6.18 Drying of coreless PNIAPM microgel (lMG, $D_\mathrm{h} \approx 1.5$ nm) film via fluorescence microscopy, scale bar corresponds to 20 μm.

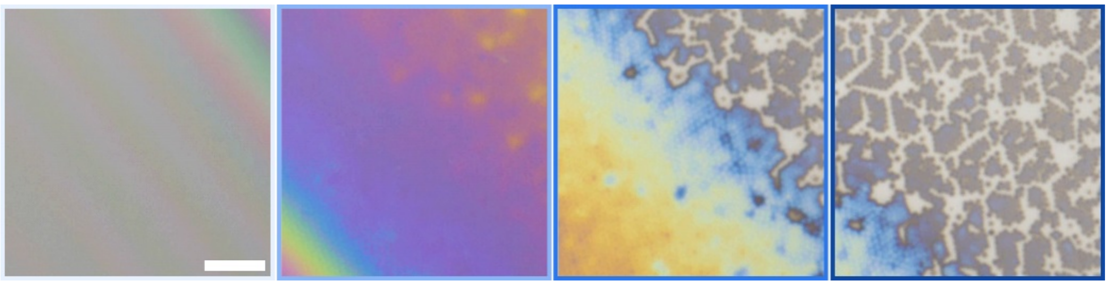

Fig. 6.19 Drying of $C_{105}S_{4.8}$-5.0 film, transferred from Π approx. 30 mN/m, scale bar corresponds to 5 μm.

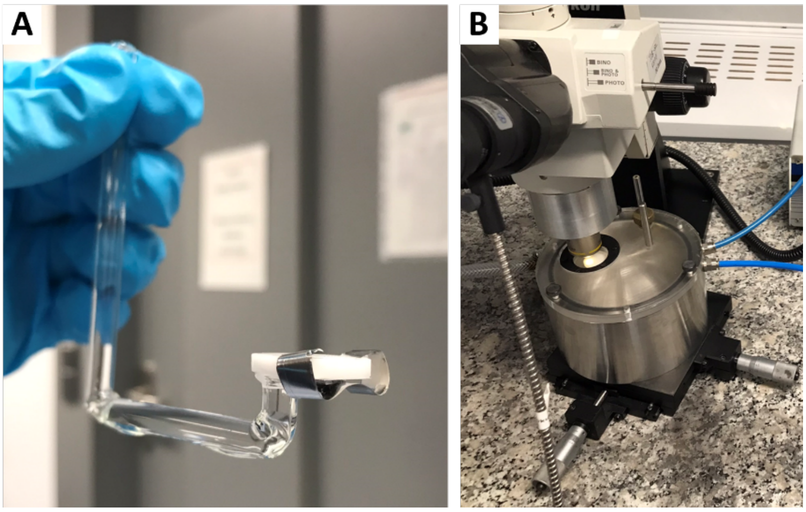

Fig. 6.20 A) A porous glass plate is attached to a glass capillary tube (film holder) used for the thin film pressure balance technique. The sample is attached to the glass plate using a stainless-steel clamp. B) The stainless-steel pressure chamber with a quartz glass window is placed under a reflective light microscope.

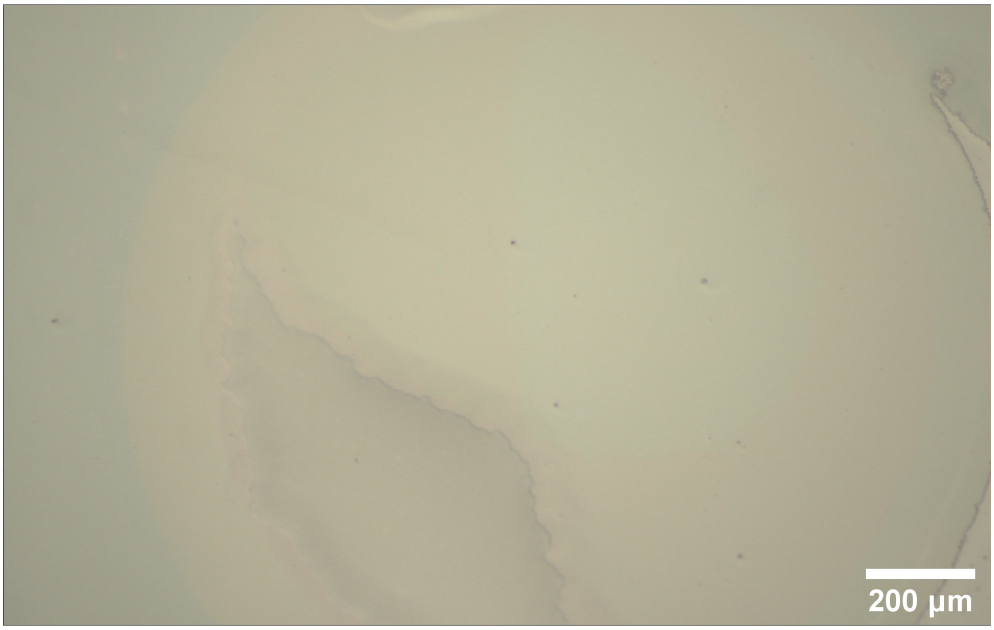

Fig. 6.21 The interface oscillation experiment depicted in Figure 6.5, only results in the formation of multilayers (4 layers of $C_{437}S_{2.3}$-2.5 film) when attempted on hydrophobic substrates.

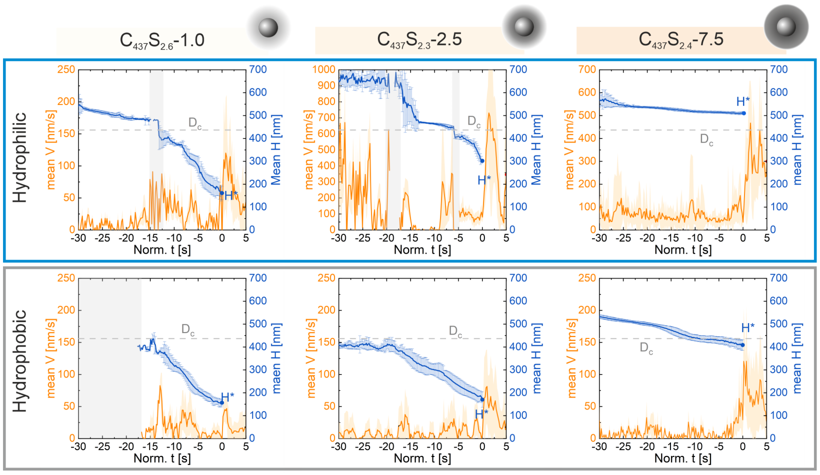

Fig. 6.22 The mean velocity, V, and film height, H, of 10 randomly chosen CS microgels are plotted against normalized time, where 0 is the onset of the collapse of the individual microgels. D_c and H^* denote the diameter of the core and the critical height of the monolayer, respectively. The shadowed areas (grey) are frames where the monolayers were out-of-focus. Monolayer drift with preferred directions is baseline-subtracted.

6.7.1 Molecular dynamics simulations

We utilized a microgel with a hydrodynamic diameter of $40 \pm 0.6\sigma$ (where σ is the diameter of a single bead) in a swollen state in water. The diameter of the solid core is $16 \pm 0.3\sigma$, resulting in a shell-to-core ratio of approximately 2.5. Figure 6.23 presents an overview of the monolayers of CS microgels at two different compression states—low and high Π.

In summary, the simulations were conducted as follows: $N_p = 16$ microgels of the same architecture were randomly placed near the air/water interface. We controlled the compression degree by simultaneously adjusting the dimensions of the simulation box in the X and Y directions, L_x and L_y. The microgel at the interface consists of a three-dimensional swollen part, namely the bulky part (B-part, Figure 6A1 in the main manuscript), immersed in the liquid phase, and a thin two-dimensional polymeric layer, namely the (air/water) interface part (I-part) and substrate part (S-part). We calculated the center of mass of each particle and computed the average 2D radial distribution functions, $g(r)$. The position of the first maximum of $g(r)$ allows us to estimate the interparticle distance. At low Π, $D_\text{c-c} = 50.1 \pm 0.4\sigma$, and at high Π, $D_\text{c-c} = 31.2 \pm 0.2\sigma$ (Table 6.2). To regulate the affinity of the microgels to the substrate, we varied the parameter $\varepsilon_\text{S-sub}$ within the range $[3\varepsilon, 20\varepsilon]$. A higher $\varepsilon_\text{S-sub}$ corresponds to a stronger attraction between the substrate and the microgels.

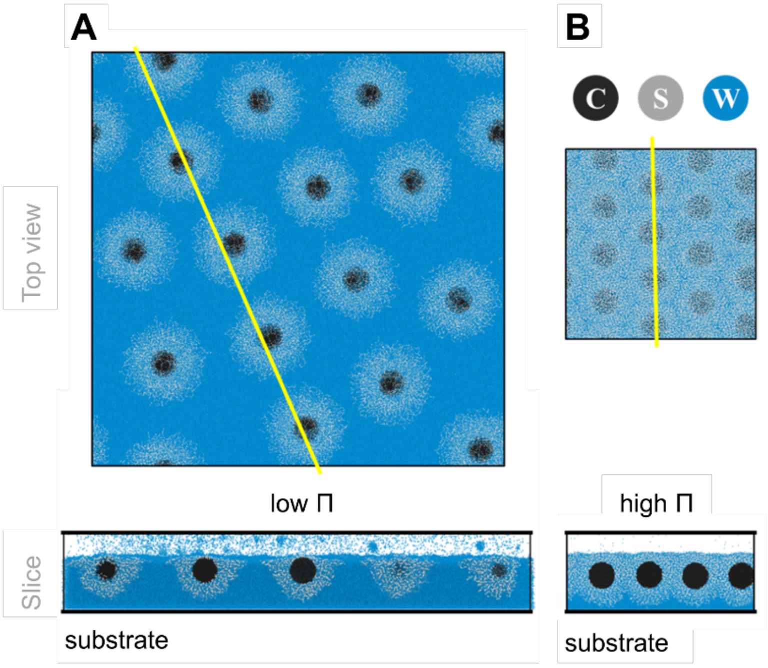

Fig. 6.23 The snapshots of microgel monolayers at liquid/air interface. Cases of low (B) and high (A) compression degrees. View from the air. Solid core, C, shell, S and water, W, beads are colored in black, grey and blue, respectively. The yellow line indicates the slice area.

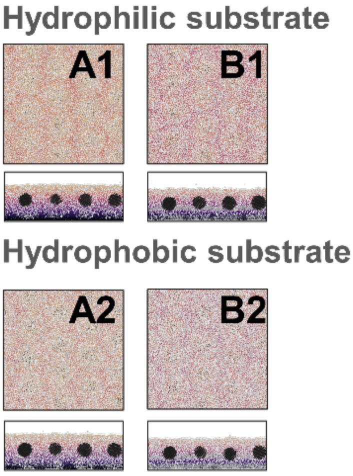

Fig. 6.24 Illustration of the different stages of monolayer drying on hydrophilic (A1-B1) and hydrophobic (A2-B2) substrates. The monolayer was transferred at a high compression degree. $\varepsilon_{S\text{-sub}} = 10\varepsilon$. Case of high affinity of the microgels to the substrate.

Table 6.2 The interparticle distance, $D_{\text{c-c}}$, of dried CS monolayers on hydrophilic substrates and hydrophobic substrates in thin film is compared to that at the air/water interphase. $\varepsilon_{\text{S-sub}}$ represents the affinity of the microgels to the substrate. $\varepsilon_{\text{S-sub}} = 20\varepsilon$ corresponds to the case of high affinity, while $\varepsilon_{\text{S-sub}} = 3\varepsilon$ corresponds to the low affinity case.

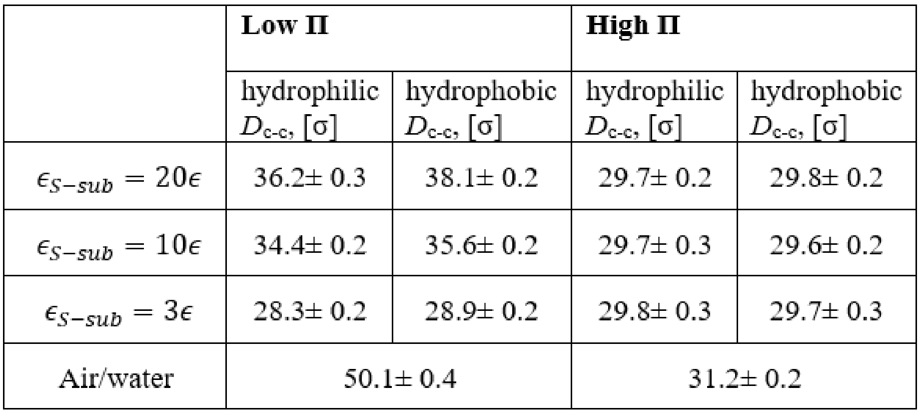

	Low Π		**High Π**	
	hydrophilic $D_{\text{c-c}}$, [σ]	hydrophobic $D_{\text{c-c}}$, [σ]	hydrophilic $D_{\text{c-c}}$, [σ]	hydrophobic $D_{\text{c-c}}$, [σ]
$\epsilon_{S-sub} = 20\epsilon$	36.2± 0.3	38.1± 0.2	29.7± 0.2	29.8± 0.2
$\epsilon_{S-sub} = 10\epsilon$	34.4± 0.2	35.6± 0.2	29.7± 0.3	29.6± 0.2
$\epsilon_{S-sub} = 3\epsilon$	28.3± 0.2	28.9± 0.2	29.8± 0.3	29.7± 0.3
Air/water	50.1± 0.4		31.2± 0.2	

Chapter 7

Conclusion and Outlook

In this thesis, the interfacial assembly and phase behaviour of soft colloids were investigated using micron-sized HCSS microgels of various dimensions and morphologies. We reported a synthesis protocol for the preparation of the micron-sized HCSS microgels with a controllable shell-to-core size ratio. Furthermore, we demonstrated their suitability and applicability as model systems by using customisable in-house small-angle light scattering and various microscopic techniques for the structural analysis during the assembly process as well as the drying dynamics of the microgel monolayers.

The comparison between the *in situ* and *ex situ* measurements during the assembly of the microgels in both reciprocal and real spaces has revealed significant differences in microstructures. *In situ* microstructures exhibit mainly hexagonal order, which pronounces with increasing surface pressure, i.e., degree of compression. This implies that the HCSS microgels (synthesised using precipitation polymerisation, core diameter ranging from approximately 200-500 nm, overall hydrodynamic diameter ranging from 600-1000 nm, and crosslinker densities ranging from 1-7.5 mol.%) do not undergo anisotropic collapse (see, Figure 1.2). This finding might suggest that the morphologies of such microgels at fluid/liquid interfaces have high energy barriers for the interpenetration/overlap of microgel shells, making the anisotropic collapse among microgels energetically not favourable. In fact, a recent study by Zhou et al. [142] conducted direct measurements of counterion clouds around microgels and demonstrated that deswelling occurs prior to contact in bulk due to osmotic pressure. For the formation of quasicrystals, therefore, it might be necessary to use microgels characterised by a lower energy barrier for interpenetration/overlap of their shells at the fluid/liquid interfaces.

Despite the relatively small size (< 10 μm, for flotation capillary force), the microgels appear to be under the influence of the capillary attractive interaction at the air/water interface, leading to clustering behaviour even at near zero surface pressure. However, when compressed further, this capillary interaction seems to be counteracted by other involved contributions, (possibly) including the elasticity of the microgel, electrostatic interactions, Marangoni flow [138]], and osmotic pressure. This is evidenced by the reversibility of microgel monolayers, as observed through the repeated compression-expansion cycles in both small-angle light scattering (SALS) and microscopy (manuscript in preparation), where changes in interparticle distance and surface pressure are closely linked (specific to a given system).

Furthermore, we demonstrated that the drying dynamics of these microgel monolayers entail a complex interplay of multiple factors. This includes the adhesion between microgels and the substrate, immersion capillary forces (linked to microgel elasticity and core size), and the free energy associated with interface formation. As the drying proceeds, the water evaporates and the microgels at the air/water interface make contact with the substrates, leading to microgel-to-substrate adhesion, which is strongly influenced by the surface chemistry of the substrate. When the adhesion is insufficient to resist the de-wetting of water on the substrate, microgels migrate with water and collapse onto each other as water leaves the microgel's body. Conversely, with strong adhesion, microgels stay in position and form a thin film (trapped in a water-thin film), experiencing an increasingly potent immersion capillary force as the drying progresses. This force can slide/tilt the microgels towards neighbouring microgels, creating intricate maze-like grain boundary-like cracks.

For applications requiring precise control of interparticle distance and symmetry, therefore microgels with a lower crosslinker density, designed for strong adhesion to target substrates, are favourable under drying conditions of rapid subphase evaporation. Considerations should be given to interparticle distance and the core size ratio to restrict the mobility of the mass centre of the microgels under the influence of operative immersion capillary forces. From a fundamental perspective, I believe that the study of microgel interactions at interfaces should begin at the single microgel level before extending to many-body interactions. It would be interesting to measure interparticle forces between two microgels perhaps with optical tweezers at various fluid/liquid interfaces. One could also link such results to nucleation (clustering) pathways of microgels at near-zero surface pressure via tracking particles. Synthesis protocols for larger HCSS microgels with high monodispersity could be beneficial for such investigations. The knowledge we require from the bulk characterisation and experiments should be transferred with caution. For instance, the swelling ratio of a PNIPAM microgel may not exhibit a straightforward correlation with the compressibility or softness of a microgel at the interface–interfacial elasticity of a microgel–because of the interfacial tension contributions, which may be linked to the interfacial rheological properties of the corresponding microgel monolayer. Additionally, it is worth noting that the interfacial tension contribution in the interaction between microgels might vary with the degree of compression, possibly decreasing as the mass centre of microgels sinks down during compression. This could lead to a reduction in the effective contact angle of the microgels, affecting their detachment energy. Last but not least, I believe, close collaborations between the experimental and theoretical/simulation teams are essential in acquiring knowledge to fully understand these complex phenomena.

References

[1] Alice P. Gast and William B. Russel. Simple ordering in complex fluids. *Physics Today*, 51(12):24–30, 1998.

[2] Ron Lifshitz. What is a crystal? *Zeitschrift für Kristallographie*, 222(6):266, 2007.

[3] D. Shechtman, I. Blech, D. Gratias, and J. W. Cahn. Metallic phase with long-range orientational order and no translational symmetry. *Physical Review Letters*, 53(20):1951–1953, 1984.

[4] Istvan Hargittai. Forty years of quasicrystals: a bumpy road to triumph. *Structural Chemistry*, 33(2):311–314, 2022.

[5] Tomonari Dotera. Quasicrystals in soft matter. *Israel Journal of Chemistry*, 51(11-12):1197–1205, 2011.

[6] Xiangbing Zeng. Liquid quasicrystals. *Current Opinion in Colloid & Interface Science*, 9(6):384–389, 2005.

[7] Steffen Fischer, Alexander Exner, Kathrin Zielske, Jan Perlich, Sofia Deloudi, Walter Steurer, Peter Lindner, and Stephan Förster. Colloidal quasicrystals with 12-fold and 18-fold diffraction symmetry. *Proceedings of the National Academy of Sciences*, 108(5):1810–1814, 2011.

[8] Jayasri Dontabhaktuni, Miha Ravnik, and Slobodan Žumer. Quasicrystalline tilings with nematic colloidal platelets. *Proceedings of the National Academy of Sciences*, 111(7):2464–2469, 2014.

[9] E. A. Jagla. Phase behavior of a system of particles with core collapse. *Physical Review E*, 58(2):1478–1486, 1998.

[10] E. A. Jagla. Core-softened potentials and the anomalous properties of water. *The Journal of Chemical Physics*, 111(19):8980–8986, 1999.

[11] T. Dotera, T. Oshiro, and P. Ziherl. Mosaic two-lengthscale quasicrystals. *Nature*, 506(7487):208–211, 2014.

[12] Harini Pattabhiraman and Marjolein Dijkstra. The effect of temperature, interaction range, and pair potential on the formation of dodecagonal quasicrystals in core-corona systems. *Journal of Physics: Condensed Matter*, 29(9):094003, 2017.

[13] Walter R. C. Somerville, Adam D. Law, Marcel Rey, Nicolas Vogel, Andrew J. Archer, and D. Martin A. Buzza. Pattern formation in two-dimensional hard-core/soft-shell systems with variable soft shell profiles. *Soft Matter*, 16(14):3564–3573, 2020.

[14] Z. Valy Vardeny, Ajay Nahata, and Amit Agrawal. Optics of photonic quasicrystals. *Nature Photonics*, 7(3):177–187, 2013.

[15] Christopher R. Iacovella, Aaron S. Keys, and Sharon C. Glotzer. Self-assembly of soft-matter quasicrystals and their approximants. *Proceedings of the National Academy of Sciences*, 108(52):20935–20940, 2011.

[16] Pablo F. Damasceno, Michael Engel, and Sharon C. Glotzer. Predictive self-assembly of polyhedra into complex structures. *Science*, 337(6093):453–457, 2012.

[17] A. Rauh, M. Rey, L. Barbera, M. Zanini, M. Karg, and L. Isa. Compression of hard core-soft shell nanoparticles at liquid-liquid interfaces: influence of the shell thickness. *Soft Matter*, 13(1):158–169, 2016.

[18] Kirsten Volk, Florian Deißenbeck, Suvendu Mandal, Hartmut Löwen, and Matthias Karg. Moiré and honeycomb lattices through self-assembly of hard-core/soft-shell microgels: experiment and simulation. *Physical Chemistry Chemical Physics*, 21(35):19153–19162, 2019.

[19] Marian Florescu, Salvatore Torquato, and Paul J. Steinhardt. Complete band gaps in two-dimensional photonic quasicrystals. *Physical Review B*, 80(15), 2009.

[20] Tianyou Fan. *Generalized dynamics of soft-matter quasicrystals: Mathematical models and solutions*, volume 260 of *Springer series in materials science*. Springer, Singapore, 2017.

[21] J. D. Joannopoulos. *Photonic crystals: Molding the flow of light / John D. Joannopoulos ... [et al.]*. Princeton University Press, Princeton, N.J. and Woodstock, 2nd ed. edition, 2008.

[22] Tianyou Fan. *Mathematical theory of elasticity of quasicrystals and its applications*, volume 246 of *Springer series in materials science, 0933-033X*. Springer, Singapore, 2nd edition edition, 2016.

[23] Keumkyung Kuk, Lukas Gregel, Vahan Abgarjan, Caspar Croonenbrock, Sebastian Hänsch, and Matthias Karg. Micron-sized silica-pnipam core-shell microgels with tunable shell-to-core ratio. *Gels*, 8(8), 2022.

[24] Matthias Karg and Thomas Hellweg. Smart inorganic/organic hybrid microgels: Synthesis and characterisation. *Journal of Materials Chemistry*, 19(46):8714, 2009.

[25] Makoto Asai, Dan Zhao, and Sanat K. Kumar. Role of grafting mechanism on the polymer coverage and self-assembly of hairy nanoparticles. *ACS Nano*, 11(7):7028–7035, 2017.

[26] Ben A. Humphreys, Stuart W. Prescott, Timothy J. Murdoch, Andrew Nelson, Elliot P. Gilbert, Grant B. Webber, and Erica J. Wanless. Influence of molecular weight on pnipam brush modified colloidal silica particles. *Soft Matter*, 15(1):55–64, 2018.

[27] Jianzhong Wu, Gang Huang, and Zhibing Hu. Interparticle potential and the phase behavior of temperature-sensitive microgel dispersions. *Macromolecules*, 36(2):440–448, 2003.

[28] Frank Scheffold. Pathways and challenges towards a complete characterization of microgels. *Nature Communications*, 11(1):4315, 2020.

[29] Dmitry Lapkin, Nastasia Mukharamova, Dameli Assalauova, Svetlana Dubinina, Jens Stellhorn, Fabian Westermeier, Sergey Lazarev, Michael Sprung, Matthias Karg, Ivan A. Vartanyants, and Janne-Mieke Meijer. In situ characterization of crystallization and melting of soft, thermoresponsive microgels by small-angle x-ray scattering. *Soft Matter*, (18):1591–1602, 2022.

[30] Keumkyung Kuk, Vahan Abgarjan, Lukas Gregel, Yichu Zhou, Virginia Carrasco Fadanelli, Ivo Buttinoni, and Matthias Karg. Compression of colloidal monolayers at liquid interfaces: in situ vs. ex situ investigation. *Soft Matter*, 19(2):175–188, 2023.

[31] Werner Stöber, Arthur Fink, and Ernst Bohn. Controlled growth of monodisperse silica spheres in the micron size range. *Journal of Colloid and Interface Science*, 26(1):62–69, 1968.

[32] G. H. Bogush, M. A. Tracy, and C. F. Zukoski. Preparation of monodisperse silica particles: Control of size and mass fraction. *Journal of Non-Crystalline Solids*, 104(1):95–106, 1988.

[33] Gunter Büchel, Michael Grün, Klaus K. Unger, Akihiko Matsumoto, and Tsutsumi Kazuo. Tailored syntheses of nanostructured silicas: Control of particle morphology, particle size and pore size. *Supramolecular Science*, 5(3-4):253–259, 1998.

[34] Jong Suk Sonn, Ju Yeon Lee, Seon Hui Jo, In-Ho Yoon, Chong-Hun Jung, and Jong Choo Lim. Effect of surface modification of silica nanoparticles by silane coupling agent on decontamination foam stability. *Annals of Nuclear Energy*, 114:11–18, 2018.

[35] Avraham Halperin, Martin Kröger, and Françoise M. Winnik. Poly(n-isopropylacrylamide) phase diagrams: Fifty years of research. *Angewandte Chemie*, 54(51):15342–15367, 2015.

[36] Jianping Ge and Yadong Yin. Responsive photonic crystals. *Angewandte Chemie*, 50(7):1492–1522, 2011.

[37] Yanbing Liu and Andrew A. Houck. Quantum electrodynamics near a photonic bandgap. *Nature Physics*, 13(1):48–52, 2017.

[38] Xuchen Wang, Mohammad Sajjad Mirmoosa, Viktar S. Asadchy, Carsten Rockstuhl, Shanhui Fan, and Sergei A. Tretyakov. Metasurface-based realization of photonic time crystals. *Science Advances*, 9(14):eadg7541, 2023.

[39] Archana Kaliyaraj Selva Kumar, Yifei Zhang, Danlei Li, and Richard G. Compton. A mini-review: How reliable is the drop casting technique? *Electrochemistry Communications*, 121:106867, 2020.

[40] Yin Fang, Blayne M. Phillips, Khalid Askar, Baeck Choi, Peng Jiang, and Bin Jiang. Scalable bottom-up fabrication of colloidal photonic crystals and periodic plasmonic nanostructures. *Journal of Materials Chemistry C*, 1(38):6031, 2013.

[41] Tomas Kohoutek, Mikhail Parchine, Maria Bardosova, and Martyn E. Pemble. Controlled self-assembly of langmuir-blodgett colloidal crystal films of monodispersed silica particles on non-planar substrates. *Colloids and Surfaces A: Physicochemical and Engineering Aspects*, 593:124625, 2020.

[42] I-Te Chen, Elizabeth Schappell, Xiaolong Zhang, and Chih-Hao Chang. Continuous roll-to-roll patterning of three-dimensional periodic nanostructures. *Microsystems & Nanoengineering*, 6(1):22, 2020.

[43] Daniel M. Balazs, Tyler A. Dunbar, Detlef-M Smilgies, and Tobias Hanrath. Coupled dynamics of colloidal nanoparticle spreading and self-assembly at a fluid-fluid interface. *Langmuir*, 36(22):6106–6115, 2020.

[44] A. Scotti, S. Bochenek, M. Brugnoni, M. A. Fernandez-Rodriguez, M. F. Schulte, J. E. Houston, A. P. H. Gelissen, I. I. Potemkin, L. Isa, and W. Richtering. Exploring the colloid-to-polymer transition for ultra-low crosslinked microgels from three to two dimensions. *Nature Communications*, 10(1):1418, 2019.

[45] Z. Cheng, P. M. Chaikin, W. B. Russel, W. V. Meyer, J. Zhu, R. B. Rogers, and R. H. Ottewill. Phase diagram of hard spheres. *Materials & Design*, 22(7):529–534, 2001.

[46] L. Andrew Lyon, Justin D. Debord, Saet Byul Debord, Clinton D. Jones, Jonathan G. McGrath, and Michael J. Serpe. Microgel colloidal crystals. *The Journal of Physical Chemistry B*, 108(50):19099–19108, 2004.

[47] J. Brijitta, B. V. R. Tata, R. G. Joshi, and T. Kaliyappan. Random hcp and fcc structures in thermoresponsive microgel crystals. *The Journal of Chemical Physics*, 131(7):074904, 2009.

[48] Kohji Ohno, Takashi Morinaga, Satoshi Takeno, Yoshinobu Tsujii, and Takeshi Fukuda. Suspensions of silica particles grafted with concentrated polymer brush: A new family of colloidal crystals. *Macromolecules*, 39(3):1245–1249, 2006.

[49] Astrid Rauh, Nico Carl, Ralf Schweins, and Matthias Karg. Role of absorbing nanocrystal cores in soft photonic crystals: A spectroscopy and sans study. *Langmuir*, 34(3):854–867, 2018.

[50] N. Denkov, O. Velev, P. Kralchevski, I. Ivanov, H. Yoshimura, and K. Nagayama. Mechanism of formation of two-dimensional crystals from latex particles on substrates. *Langmuir*, 8(12):3183–3190, 1992.

[51] Eduardo Guzmán, Irene Abelenda-Núñez, Armando Maestro, Francisco Ortega, Andreas Santamaria, and Ramón G. Rubio. Particle-laden fluid/fluid interfaces: physico-chemical foundations. *Journal of Physics: Condensed Matter*, 33(33):333001, 2021.

[52] L. Isa, I. Buttinoni, M. A. Fernandez-Rodriguez, and S. A. Vasudevan. Two-dimensional assemblies of soft repulsive colloids confined at fluid interfaces. *EPL (Europhysics Letters)*, 119(2):26001, 2017.

[53] Déborah Feller and Matthias Karg. Fluid interface-assisted assembly of soft microgels: recent developments for structures beyond hexagonal packing. *Soft Matter*, 18(34):6301–6312, 2022.

[54] M. J. García-Salinas, M. S. Romero-Cano, and F. J. de las Nieves. Colloidal stability of a temperature-sensitive poly(n-isopropylacrylamide/2-acrylamido-2-methylpropanesulphonic acid) microgel. *Journal of Colloid and Interface Science*, 248(1):54–61, 2002.

[55] Zhi Zhou, Javoris V. Hollingsworth, Song Hong, Guangmin Wei, Yu Shi, Xi Lu, He Cheng, and Charles C. Han. Effects of particle softness on shear thickening of microgel suspensions. *Soft Matter*, 10(33):6286–6293, 2014.

[56] Steffen Bochenek, Andrea Scotti, and Walter Richtering. Temperature-sensitive soft microgels at interfaces: air-water versus oil-water. *Soft Matter*, 17(4):976–988, 2020.

[57] Robert Pelton. Poly(n-isopropylacrylamide) (pnipam) is never hydrophobic. *Journal of Colloid and Interface Science*, 348(2):673–674, 2010.

[58] R. Pelton. Temperature-sensitive aqueous microgels. *Advances in Colloid and Interface Science*, 85(1):1–33, 2000.

[59] Ekaterina Ponomareva, Ben Tadgell, Marco Hildebrandt, Marcel Krüsmann, Sylvain Prévost, Paul Mulvaney, and Matthias Karg. The fuzzy sphere morphology is responsible for the increase in light scattering during the shrinkage of thermoresponsive microgels. *Soft Matter*, 18(4):807–825, 2022.

[60] D. M. Heyes and A. C. Brańka. Interactions between microgel particles. *Soft Matter*, 5(14):2681, 2009.

[61] Andrij Pich and Walter Richtering. Microgels by precipitation polymerization: Synthesis, characterization, and functionalization. In Andrij Z. Pich, W. Richtering, and K. Albrecht, editors, *Chemical design of responsive microgels*, volume 234 of *Advances in polymer science, 0065-3195*, pages 1–37. Springer, Heidelberg, 2010.

[62] X. Wu, R. H. Pelton, A. E. Hamielec, D. R. Woods, and W. McPhee. The kinetics of poly(n-isopropylacrylamide) microgel latex formation. *Colloid & Polymer Science*, 272(4):467–477, 1994.

[63] Mirja Andersson and Sirkka Liisa Maunu. Structural studies of poly(n-isopropylacrylamide) microgels: Effect of sds surfactant concentration in the microgel synthesis. *Journal of Polymer Science Part B: Polymer Physics*, 44(23):3305–3314, 2006.

[64] Roberta Acciaro, Tibor Gilányi, and Imre Varga. Preparation of monodisperse poly(n-isopropylacrylamide) microgel particles with homogenous cross-link density distribution. *Langmuir*, 27(12):7917–7925, 2011.

[65] Zhiyong Meng, Michael H. Smith, and L. Andrew Lyon. Temperature-programmed synthesis of micron-sized multi-responsive microgels. *Colloid & Polymer Science*, 287(3):277–285, 2009.

[66] Tim Still, Ke Chen, Ahmed M. Alsayed, Kevin B. Aptowicz, and A. G. Yodh. Synthesis of micrometer-size poly(n-isopropylacrylamide) microgel particles with homogeneous crosslinker density and diameter control. *Journal of Colloid and Interface Science*, 405:96–102, 2013.

[67] Man-hin Kwok, Zifu Li, and To Ngai. Controlling the synthesis and characterization of micrometer-sized pnipam microgels with tailored morphologies. *Langmuir*, 29(30):9581–9591, 2013.

[68] Judith Witte, Tetyana Kyrey, Jana Lutzki, Anna Margarethe Dahl, Judith Houston, Aurel Radulescu, Vitaliy Pipich, Laura Stingaciu, Matthias Kühnhammer, Marcus U. Witt, Regine von Klitzing, Olaf Holderer, and Stefan Wellert. A comparison of the network structure and inner dynamics of homogeneously and heterogeneously crosslinked pnipam microgels with high crosslinker content. *Soft Matter*, 15(5):1053–1064, 2019.

[69] Agnieszka Natalia Ksiazkiewicz, Luise Bering, Falco Jung, Nadja Anna Wolter, Jörn Viell, Alexander Mitsos, and Andrij Pich. Closing the 1–5 µm size gap: Temperature-programmed, fed-batch synthesis of µm-sized microgels. *Chemical Engineering Journal*, 379:122293, 2020.

[70] Matthias Karg, Stefan Wellert, Sylvain Prevost, Ralf Schweins, Charles Dewhurst, Luis M. Liz-Marzán, and Thomas Hellweg. Well defined hybrid pnipam core-shell microgels: size variation of the silica nanoparticle core. *Colloid & Polymer Science*, 289(5-6):699–709, 2011.

[71] Siddarth A. Vasudevan, Astrid Rauh, Martin Kröger, Matthias Karg, and Lucio Isa. Dynamics and wetting behavior of core-shell soft particles at a fluid-fluid interface. *Langmuir*, 34(50):15370–15382, 2018.

[72] Jo Sing Julia Tang, Romina Sigrid Bader, Eric S. A. Goerlitzer, Jan Fedja Wendisch, Gilles Remi Bourret, Marcel Rey, and Nicolas Vogel. Surface patterning with sio2@pnipam core-shell particles. *ACS Omega*, 3(9):12089–12098, 2018.

[73] Yuichiro Nishizawa, Kenshiro Honda, Matthias Karg, and Daisuke Suzuki. Controlling the shell structure of hard core/hydrogel shell microspheres. *Colloid & Polymer Science*, pages 1–8, 2022.

[74] D. Julian McClements. Theoretical analysis of factors affecting the formation and stability of multilayered colloidal dispersions. *Langmuir*, 21(21):9777–9785, 2005.

[75] Benjamin Zeeb, Chutima Thongkaew, and Jochen Weiss. Theoretical and practical considerations in electrostatic depositioning of charged polymers. *Journal of Applied Polymer Science*, 131(7), 2014.

[76] Markus Stieger, Jan Skov Pedersen, Peter Lindner, and Walter Richtering. Are thermoresponsive microgels model systems for concentrated colloidal suspensions? a rheology and small-angle neutron scattering study. *Langmuir*, 20(17):7283–7292, 2004.

[77] Laura Hoppe Alvarez, Sabine Eisold, Rustam A. Gumerov, Martin Strauch, Andrey A. Rudov, Pia Lenssen, Dorit Merhof, Igor I. Potemkin, Ulrich Simon, and Dominik Wöll. Deformation of microgels at solid-liquid interfaces visualized in three-dimension. *Nano Letters*, 19(12):8862–8867, 2019.

[78] H. Senff, W. Richtering, Ch. Norhausen, A. Weiss, and M. Ballauff. Rheology of a temperature sensitive core−shell latex. *Langmuir*, 15(1):102–106, 1999.

[79] Fangfang Chu, Nils Heptner, Yan Lu, Miriam Siebenbürger, Peter Lindner, Joachim Dzubiella, and Matthias Ballauff. Colloidal plastic crystals in a shear field. *Langmuir*, 31(22):5992–6000, 2015.

[80] Robert W. Style, Lucio Isa, and Eric R. Dufresne. Adsorption of soft particles at fluid interfaces. *Soft Matter*, 11(37):7412–7419, 2015.

[81] Divya Ganapathi, Dibyashree Chakrabarti, A. K. Sood, and Rajesh Ganapathy. Structure determines where crystallization occurs in a soft colloidal glass. *Nature Physics*, pages 1–7, 2020.

[82] Paul C. Hiemenz and Raj Rajagopalan. *Principles of colloid and surface chemistry*. Marcel Dekker, New York, 3rd ed., rev. and expanded / paul c. hiemenz, raj rajagopalan edition, 1997.

[83] David J. Lockwood. Rayleigh and mie scattering. In M. Ronnier Luo, editor, *Encyclopedia of color science and technology*, pages 1097–1107. Springer Science+Business Media, New York, 2016.

[84] Christopher S. Buehler, James M. Caruthers, and Elias I. Franses. Light scattering theory from monodisperse spheroidal particles in the rayleigh–debye–gans regime. *The Journal of Chemical Physics*, 92(1):140–156, 1990.

[85] O. L. J. Virtanen, A. Mourran, P. T. Pinard, and W. Richtering. Persulfate initiated ultra-low cross-linked poly(n-isopropylacrylamide) microgels possess an unusual inverted cross-linking structure. *Soft Matter*, 12(17):3919–3928, 2016.

[86] M. Hildebrandt, D. Pham Thuy, J. Kippenberger, T. L. Wigger, J. E. Houston, A. Scotti, and M. Karg. Fluid-solid transitions in photonic crystals of soft, thermoresponsive microgels. *Soft Matter*, 19(37):7122–7135, 2023.

[87] John William Strutt. On the theory of long waves and bores. *Proceedings of the Royal Society of London A*, 90(619):324–328, 1914.

[88] Ingo Breßler, Joachim Kohlbrecher, and Andreas F. Thünemann. Sasfit: a tool for small-angle scattering data analysis using a library of analytical expressions. *Journal of Applied Crystallography*, 48(Pt 5):1587–1598, 2015.

[89] J. Kohlbrecher and A. Studer. Transformation cycle between the spherically symmetric correlation function, projected correlation function and differential cross section as implemented in sasfit. *Journal of Applied Crystallography*, 50(5):1395–1403, 2017.

[90] Joachim Kohlbrecher and Ingo Breßler. Updates in sasfit for fitting analytical expressions and numerical models to small-angle scattering patterns. *Journal of Applied Crystallography*, 55(Pt 6):1677–1688, 2022.

[91] B. J. Frisken. Revisiting the method of cumulants for the analysis of dynamic light-scattering data. *Applied Optics*, 40(24):4087–4091, 2001.

[92] A. Scotti, W. Liu, J. S. Hyatt, E. S. Herman, H. S. Choi, J. W. Kim, L. A. Lyon, U. Gasser, and A. Fernandez-Nieves. The contin algorithm and its application to determine the size distribution of microgel suspensions. *The Journal of Chemical Physics*, 142(23):234905, 2015.

[93] V. Ruseva, M. Lyons, J. Powell, J. Austin, A. Malm, and J. Corbett. Capillary dynamic light scattering: Continuous hydrodynamic particle size from the nano to the micro-scale. *Colloids and Surfaces A: Physicochemical and Engineering Aspects*, 558:504–511, 2018.

[94] Valentina Ruseva, Hanna Jankevics, and Jason Corbett. An optimized filling method for capillary dls. *MethodsX*, 6:606–614, 2019.

[95] U. Keiderling. The new 'bersans-pc' software for reduction and treatment of small angle neutron scattering data. *Applied Physics A*, 74(0):s1455–s1457, 2002.

[96] S. Förster, L. Apostol, and W. Bras. Scatter : software for the analysis of nano- and mesoscale small-angle scattering. *Journal of Applied Crystallography*, 43(3):639–646, 2010.

[97] T. H. Besseling, M. Hermes, A. Fortini, M. Dijkstra, A. Imhof, and A. van Blaaderen. Oscillatory shear-induced 3d crystalline order in colloidal hard-sphere fluids. *Soft Matter*, 8(26):6931, 2012.

[98] Junwei Wang, Chrameh Fru Mbah, Thomas Przybilla, Benjamin Apeleo Zubiri, Erdmann Spiecker, Michael Engel, and Nicolas Vogel. Magic number colloidal clusters as minimum free energy structures. *Nature Communications*, 9(1):5259, 2018.

[99] V. J. Anderson and H. N. W. Lekkerkerker. Insights into phase transition kinetics from colloid science. *Nature*, 416(6883):811–815, 2002.

[100] Mathieu Destribats, Véronique Lapeyre, Mélanie Wolfs, Elisabeth Sellier, Fernando Leal-Calderon, Valérie Ravaine, and Véronique Schmitt. Soft microgels as pickering emulsion stabilisers: role of particle deformability. *Soft Matter*, 7(17):7689, 2011.

[101] Jacopo Vialetto, Shivaprakash N. Ramakrishna, and Lucio Isa. In situ imaging of the three-dimensional shape of soft responsive particles at fluid interfaces by atomic force microscopy. *Science Advances*, 8(45):eabq2019, 2022.

[102] Man-hin Kwok and To Ngai. Comparing the relative interfacial affinity of soft colloids with different crosslinking densities in pickering emulsions. *Frontiers in chemistry*, 6:148, 2018.

[103] Adam Edward Stones, Roel P. A. Dullens, and Dirk G. A. L. Aarts. Model-free measurement of the pair potential in colloidal fluids using optical microscopy. *Physical Review Letters*, 123(9):098002, 2019.

[104] Ivo Buttinoni and Roel P. A. Dullens. Mechanical properties of colloidal crystals at fluid interfaces. *Journal of Physics: Materials*, 4(2):025001, 2021.

[105] Shilin Huang, Kornelia Gawlitza, Regine von Klitzing, Laurent Gilson, Johannes Nowak, Stefan Odenbach, Werner Steffen, and Günter K. Auernhammer. Microgels at the water/oil interface: In situ observation of structural aging and two-dimensional magnetic bead microrheology. *Langmuir*, 32(3):712–722, 2016.

[106] Iain Muntz, James A. Richards, Sam Brown, Andrew B. Schofield, Marcel Rey, and Job H. J. Thijssen. Contactless interfacial rheology: Probing shear at liquid–liquid interfaces without an interfacial geometry via fluorescence microscopy. *Journal of Rheology*, 67(1):67–80, 2023.

[107] Q. Zhong, D. Inniss, K. Kjoller, and V. B. Elings. Fractured polymer/silica fiber surface studied by tapping mode atomic force microscopy. *Surface Science Letters*, 290(1-2):L688–L692, 1993.

[108] Franz J. Giessibl. Advances in atomic force microscopy. *Reviews of Modern Physics*, 75(3):949–983, 2003.

[109] Nicholas A. Geisse. Afm and combined optical techniques. *Materials Today*, 12(7-8):40–45, 2009.

[110] Sarah Höfl, Lothar Zitzler, Thomas Hellweg, Stephan Herminghaus, and Frieder Mugele. Volume phase transition of “smart” microgels in bulk solution and adsorbed at an interface: A combined afm, dynamic light, and small angle neutron scattering study. *Polymer*, 48(1):245–254, 2007.

[111] M. Friederike Schulte, Andrea Scotti, Monia Brugnoni, Steffen Bochenek, Ahmed Mourran, and Walter Richtering. Tuning the structure and properties of ultra-low cross-linked temperature-sensitive microgels at interfaces via the adsorption pathway. *Langmuir*, 35(46):14769–14781, 2019.

[112] S. W. Paddock. Principles and practices of laser scanning confocal microscopy. *Molecular Biotechnology*, 16(2):127–149, 2000.

[113] A. D. Dinsmore, E. R. Weeks, V. Prasad, A. C. Levitt, and D. A. Weitz. Three-dimensional confocal microscopy of colloids. *Applied Optics*, 40(24):4152–4159, 2001.

[114] José-Angel Conchello and Jeff W. Lichtman. Optical sectioning microscopy. *Nature Methods*, 2(12):920–931, 2005.

[115] V. Prasad, D. Semwogerere, and Eric R. Weeks. Confocal microscopy of colloids. *Journal of Physics: Condensed Matter*, 19(11):113102, 2007.

[116] Junjie Li and Francis Leonard Deepak. In situ kinetic observations on crystal nucleation and growth. *Chemical Reviews*, 122(23):16911–16982, 2022.

[117] Daan Frenkel. Entropy-driven phase transitions. *Physica A: Statistical Mechanics and its Applications*, 263(1-4):26–38, 1999.

[118] P. N. Pusey and W. van Megen. Phase behaviour of concentrated suspensions of nearly hard colloidal spheres. *Nature*, 320(6060):340–342, 1986.

[119] B. Derjaguin and L. Landau. Theory of the stability of strongly charged lyophobic sols and of the adhesion of strongly charged particles in solutions of electrolytes. *Progress in Surface Science*, 43(1-4):30–59, 1993.

[120] E. J. W. Verwey. Theory of the stability of lyophobic colloids. *The Journal of Physical and Colloid Chemistry*, 51(3):631–636, 1947.

[121] B. W. Ninham. On progress in forces since the dlvo theory. *Advances in Colloid and Interface Science*, 83(1-3):1–17, 1999.

[122] Víctor Agmo Hernández. An overview of surface forces and the dlvo theory. *ChemTexts*, 9(4):1–16, 2023.

[123] Subir Bhattacharjee, Chun-Han Ko, and Menachem Elimelech. Dlvo interaction between rough surfaces. *Langmuir*, 14(12):3365–3375, 1998.

[124] H. C. Hamaker. The london—van der waals attraction between spherical particles. *Physica*, 4(10):1058–1072, 1937.

[125] D. Leckband and J. Israelachvili. Intermolecular forces in biology. *Quarterly Reviews of Biophysics*, 34(2):105–267, 2001.

[126] Spencer Umfreville Pickering. Cxcvi.—emulsions. *Journal of the Chemical Society, Transactions*, 91(0):2001–2021, 1907.

[127] Bernard P. Binks. Particles as surfactants—similarities and differences. *Current Opinion in Colloid & Interface Science*, 7(1-2):21–41, 2002.

[128] Emanuele Vignati, Roberto Piazza, and Thomas P. Lockhart. Pickering emulsions: Interfacial tension, colloidal layer morphology, and trapped-particle motion. *Langmuir*, 19(17):6650–6656, 2003.

[129] F. Bresme and M. Oettel. Nanoparticles at fluid interfaces. *Journal of Physics: Condensed Matter*, 19(41):413101, 2007.

[130] Yves Chevalier and Marie-Alexandrine Bolzinger. Emulsions stabilized with solid nanoparticles: Pickering emulsions. *Colloids and Surfaces A: Physicochemical and Engineering Aspects*, 439:23–34, 2013.

[131] Peter A. Kralchevsky and Krassimir D. Danov. Interactions between particles at a fluid interface. In *Nanoscience*, pages 397–435. CRC Press, 2010.

[132] Kan Du, Elizabeth Glogowski, Todd Emrick, Thomas P. Russell, and Anthony D. Dinsmore. Adsorption energy of nano- and microparticles at liquid-liquid interfaces. *Langmuir*, 26(15):12518–12522, 2010.

[133] Anna Zigelman and Ofer Manor. The electrical double layer force between spherical particles which are partially submerged in water. *Langmuir*, 36(18):4942–4954, 2020.

[134] Peter A. Kralchevsky and Kuniaki Nagayama. Capillary interactions between particles bound to interfaces, liquid films and biomembranes. *Advances in Colloid and Interface Science*, 85(2-3):145–192, 2000.

[135] Mariana P. Boneva, Krassimir D. Danov, Nikolay C. Christov, and Peter A. Kralchevsky. Attraction between particles at a liquid interface due to the interplay of gravity- and electric-field-induced interfacial deformations. *Langmuir*, 25(16):9129–9139, 2009.

[136] Elka S. Basheva, Peter A. Kralchevsky, Krassimir D. Danov, Rumyana D. Stanimirova, Neil Shaw, and Jordan T. Petkov. Vortex in liquid films from concentrated surfactant solutions containing micelles and colloidal particles. *Journal of Colloid and Interface Science*, 576:345–355, 2020.

[137] Jacopo Vialetto, Michele Zanini, and Lucio Isa. Attachment and detachment of particles to and from fluid interfaces. *Current Opinion in Colloid & Interface Science*, 58:101560, 2022.

[138] Zilong Qiu, Annelies Malfliet, Bart Blanpain, and Muxing Guo. Capillary interaction between micron-sized ce2o3 inclusions at the ar gas/liquid steel interface. *Metallurgical and Materials Transactions B*, 53(3):1775–1791, 2022.

[139] Samuel Trevenen, Md Anisur Rahman, Heather S. C. Hamilton, Alexander E. Ribbe, Laura C. Bradley, and Peter J. Beltramo. Nanoscale porosity in microellipsoids cloaks interparticle capillary attraction at fluid interfaces. *ACS Nano*, 17(12):11892–11904, 2023.

[140] Wei He, Nesrin Şenbil, and A. D. Dinsmore. Measured capillary forces on spheres at particle-laden interfaces. *Soft Matter*, 11(25):5087–5094, 2015.

[141] Jacopo Vialetto, Natalie Nussbaum, Jotam Bergfreund, Peter Fischer, and Lucio Isa. Influence of the interfacial tension on the microstructural and mechanical properties of microgels at fluid interfaces. *Journal of Colloid and Interface Science*, 608(Pt 3):2584–2592, 2022.

[142] Boyang Zhou, Urs Gasser, and Alberto Fernandez-Nieves. Measuring the counterion cloud of soft microgels using sans with contrast variation. *Nature Communications*, 14(1):3827, 2023.

[143] Robert W. Style, Anand Jagota, Chung-Yuen Hui, and Eric R. Dufresne. Elastocapillarity: Surface tension and the mechanics of soft solids. *Annual Review of Condensed Matter Physics*, 8(1):99–118, 2017.

[144] Johannes Harrer, Marcel Rey, Simone Ciarella, Hartmut Löwen, Liesbeth M. C. Janssen, and Nicolas Vogel. Stimuli-responsive behavior of pnipam microgels under interfacial confinement. *Langmuir*, 35(32):10512–10521, 2019.

[145] Marcel Rey, Miguel Angel Fernandez-Rodriguez, Matthias Karg, Lucio Isa, and Nicolas Vogel. Poly-n-isopropylacrylamide nanogels and microgels at fluid interfaces. *Accounts of Chemical Research*, 53(2):414–424, 2020.

[146] Steffen Bochenek, Fabrizio Camerin, Emanuela Zaccarelli, Armando Maestro, Maximilian M. Schmidt, Walter Richtering, and Andrea Scotti. In-situ study of the impact of temperature and architecture on the interfacial structure of microgels. *Nature Communications*, 13(1):3744, 2022.

[147] Lucio Isa, Falk Lucas, Roger Wepf, and Erik Reimhult. Measuring single-nanoparticle wetting properties by freeze-fracture shadow-casting cryo-scanning electron microscopy. *Nature Communications*, 2(1):438, 2011.

[148] Florent Pinaud, Karen Geisel, Pascal Massé, Bogdan Catargi, Lucio Isa, Walter Richtering, Valérie Ravaine, and Véronique Schmitt. Adsorption of microgels at an oil-water interface: correlation between packing and 2d elasticity. *Soft Matter*, 10(36):6963–6974, 2014.

[149] Laura Scheidegger, Miguel Ángel Fernández-Rodríguez, Karen Geisel, Michele Zanini, Roey Elnathan, Walter Richtering, and Lucio Isa. Compression and deposition of microgel monolayers from fluid interfaces: particle size effects on interface microstructure and nanolithography. *Physical Chemistry Chemical Physics*, 19(13):8671–8680, 2017.

[150] Marcel Rey, Miguel Ángel Fernández-Rodríguez, Mathias Steinacher, Laura Scheidegger, Karen Geisel, Walter Richtering, Todd M. Squires, and Lucio Isa. Isostructural solid-solid phase transition in monolayers of soft core-shell particles at fluid interfaces: structure and mechanics. *Soft Matter*, 12(15):3545–3557, 2016.

[151] Christine Picard, Patrick Garrigue, Marie-Charlotte Tatry, Véronique Lapeyre, Serge Ravaine, Véronique Schmitt, and Valérie Ravaine. Organization of microgels at the air-water interface under compression: Role of electrostatics and cross-linking density. *Langmuir*, 33(32):7968–7981, 2017.

[152] Steffen Bochenek, Andrea Scotti, Wojciech Ogieglo, Miguel Ángel Fernández-Rodríguez, M. Friederike Schulte, Rustam A. Gumerov, Nikita V. Bushuev, Igor I. Potemkin, Matthias Wessling, Lucio Isa, and Walter Richtering. Effect of the 3d swelling of microgels on their 2d phase behavior at the liquid-liquid interface. *Langmuir*, 35(51):16780–16792, 2019.

[153] Maximilian M. Schmidt, Steffen Bochenek, Alexey A. Gavrilov, Igor I. Potemkin, and Walter Richtering. Influence of charges on the behavior of polyelectrolyte microgels confined to oil-water interfaces. *Langmuir*, 36(37):11079–11093, 2020.

[154] Johannes Harrer, Simone Ciarella, Marcel Rey, Hartmut Löwen, Liesbeth M. C. Janssen, and Nicolas Vogel. Collapse-induced phase transitions in binary interfacial microgel monolayers. *Soft Matter*, 17(17):4504–4516, 2021.

[155] Sabrina Schmidt, Tingting Liu, Stephan Rütten, Kim-Ho Phan, Martin Möller, and Walter Richtering. Influence of microgel architecture and oil polarity on stabilization of emulsions by stimuli-sensitive core-shell poly(n-isopropylacrylamide-co-methacrylic

acid) microgels: Mickering versus pickering behavior? *Langmuir*, 27(16):9801–9806, 2011.

[156] Harini Pattabhiraman and Marjolein Dijkstra. On the formation of stripe, sigma, and honeycomb phases in a core-corona system. *Soft Matter*, 13(25):4418–4432, 2017.

[157] Heiko G. Schoberth, Heike Emmerich, Markus Holzinger, Martin Dulle, Stephan Förster, and Thomas Gruhn. Molecular dynamics study of colloidal quasicrystals. *Soft Matter*, 12(36):7644–7654, 2016.

[158] Fabio Grillo, Miguel Angel Fernandez-Rodriguez, Maria-Nefeli Antonopoulou, Dominic Gerber, and Lucio Isa. Self-templating assembly of soft microparticles into complex tessellations. *Nature*, 582(7811):219–224, 2020.

[159] Miguel Angel Fernandez-Rodriguez, Maria-Nefeli Antonopoulou, and Lucio Isa. Near-zero surface pressure assembly of rectangular lattices of microgels at fluid interfaces for colloidal lithography. *Soft Matter*, 17(2):335–340, 2021.

[160] Johannes Menath, Jack Eatson, Robert Brilmayer, Annette Andrieu-Brunsen, D. Martin A. Buzza, and Nicolas Vogel. Defined core-shell particles as the key to complex interfacial self-assembly. *Proceedings of the National Academy of Sciences*, 118(52), 2021.

[161] Maret Ickler, Johannes Menath, Laura Holstein, Marcel Rey, D. Martin A. Buzza, and Nicolas Vogel. Interfacial self-assembly of sio2-pnipam core-shell particles with varied crosslinking density. *Soft Matter*, 18(30):5585–5597, 2022.

[162] Marcel Rey, Xunan Hou, Jo Sing Julia Tang, and Nicolas Vogel. Interfacial arrangement and phase transitions of pnipam microgels with different crosslinking densities. *Soft Matter*, 13(46):8717–8727, 2017.

[163] Steffen Bochenek, Cathy E. McNamee, Michael Kappl, Hans-Juergen Butt, and Walter Richtering. Interactions between a responsive microgel monolayer and a rigid colloid: from soft to hard interfaces. *Physical Chemistry Chemical Physics*, 23(31):16754–16766, 2021.

[164] Simone Ciarella, Marcel Rey, Johannes Harrer, Nicolas Holstein, Maret Ickler, Hartmut Löwen, Nicolas Vogel, and Liesbeth M. C. Janssen. Soft particles at liquid interfaces: From molecular particle architecture to collective phase behavior. *Langmuir*, 37(17):5364–5375, 2021.

[165] Jacopo Vialetto, Fabrizio Camerin, Shivaprakash N. Ramakrishna, Emanuela Zaccarelli, and Lucio Isa. Exploring the 3d conformation of hard-core soft-shell particles adsorbed at a fluid interface. *Advanced Science*, page e2303404, 2023.

[166] Siddarth A. Vasudevan, Astrid Rauh, Lorenzo Barbera, Matthias Karg, and Lucio Isa. Stable in bulk and aggregating at the interface: Comparing core-shell nanoparticles in suspension and at fluid interfaces. *Langmuir*, 34(3):886–895, 2018.

[167] Paul Jenkins and Martin Snowden. Depletion flocculation in colloidal dispersions. *Advances in Colloid and Interface Science*, 68:57–96, 1996.

[168] Matthias Karg, Andrij Pich, Thomas Hellweg, Todd Hoare, L. Andrew Lyon, J. J. Crassous, Daisuke Suzuki, Rustam A. Gumerov, Stefanie Schneider, Igor I. Potemkin, and Walter Richtering. Nanogels and microgels: From model colloids to applications, recent developments, and future trends. *Langmuir*, 35(19):6231–6255, 2019.

[169] Felix A. Plamper and Walter Richtering. Functional microgels and microgel systems. *Accounts of Chemical Research*, 50(2):131–140, 2017.

[170] Janine Dubbert, Katja Nothdurft, Matthias Karg, and Walter Richtering. Core-shell-shell and hollow double-shell microgels with advanced temperature responsiveness. *Macromolecular Rapid Communications*, 36(2):159–164, 2015.

[171] Matthias Karg, Isabel Pastoriza-Santos, Benito Rodriguez-González, Regine von Klitzing, Stefan Wellert, and T. Hellweg. Temperature, ph, and ionic strength induced changes of the swelling behavior of pnipam-poly(allylacetic acid) copolymer microgels. *Langmuir*, 24(12):6300–6306, 2008.

[172] Andrea Scotti, M. Friederike Schulte, Carlos G. Lopez, Jérôme J. Crassous, Steffen Bochenek, and Walter Richtering. How softness matters in soft nanogels and nanogel assemblies. *Chemical Reviews*, 122(13):11675–11700, 2022.

[173] Matthias Karg. Functional materials design through hydrogel encapsulation of inorganic nanoparticles: Recent developments and challenges. *Macromolecular Chemistry and Physics*, 217(2):242–255, 2016.

[174] Matthias Karg. Multifunctional inorganic/organic hybrid microgels. *Colloid & Polymer Science*, 290(8):673–688, 2012.

[175] Matthias Karg, Thomas Hellweg, and Paul Mulvaney. Self-assembly of tunable nanocrystal superlattices using poly-(nipam) spacers. *Advanced Functional Materials*, 21(24):4668–4676, 2011.

[176] Marian Cors, Oliver Wrede, Anne-Caroline Genix, Dario Anselmetti, Julian Oberdisse, and Thomas Hellweg. Core-shell microgel-based surface coatings with linear thermoresponse. *Langmuir*, 33(27):6804–6811, 2017.

[177] Andreas J. Schmid, Janine Dubbert, Andrey A. Rudov, Jan Skov Pedersen, Peter Lindner, Matthias Karg, Igor I. Potemkin, and Walter Richtering. Multi-shell hollow nanogels with responsive shell permeability. *Scientific Reports*, 6(1):22736, 2016.

[178] Dustin Werner Kurka, Maximilian Niehues, Sergej Kudruk, Volker Gerke, and Bart Jan Ravoo. Polythiolactone-decorated silica particles: A versatile approach for surface functionalization, catalysis and encapsulation. *Chemistry*, 27(28):7667–7676, 2021.

[179] KERN W. Cleaning solution based on hydrogen peroxide for use in silicon semiconductor technology. *RCA Review*, 31:187–205, 1970.

[180] Yannic Brasse, Mareen B. Müller, Matthias Karg, Christian Kuttner, Tobias A. F. König, and Andreas Fery. Magnetic and electric resonances in particle-to-film-coupled functional nanostructures. *ACS Applied Materials & Interfaces*, 10(3):3133–3141, 2018.

[181] Mirja Andersson and Sirkka Liisa Maunu. Volume phase transition and structure of poly(n-isopropylacrylamide) microgels studied with 1h-NMR spectroscopy in D_2O. *Colloid & Polymer Science*, 285(3):293–303, 2006.

[182] Rajib Ghosh Chaudhuri and Santanu Paria. Core/shell nanoparticles: classes, properties, synthesis mechanisms, characterization, and applications. *Chemical Reviews*, 112(4):2373–2433, 2012.

[183] Zhe Gong, Theodore Hueckel, Gi-Ra Yi, and Stefano Sacanna. Patchy particles made by colloidal fusion. *Nature*, 550(7675):234–238, 2017.

[184] Mingxin He, Johnathon P. Gales, Étienne Ducrot, Zhe Gong, Gi-Ra Yi, Stefano Sacanna, and David J. Pine. Colloidal diamond. *Nature*, 585(7826):524–529, 2020.

[185] Jie Zhang, Bartosz A. Grzybowski, and Steve Granick. Janus particle synthesis, assembly, and application. *Langmuir*, 33(28):6964–6977, 2017.

[186] Hanumantha Rao Vutukuri, Arnout Imhof, and Alfons van Blaaderen. Fabrication of polyhedral particles from spherical colloids and their self-assembly into rotator phases. *Angewandte Chemie*, 53(50):13830–13834, 2014.

[187] Songbo Ni, Jessica Leemann, Ivo Buttinoni, Lucio Isa, and Heiko Wolf. Programmable colloidal molecules from sequential capillarity-assisted particle assembly. *Science Advances*, 2(4):e1501779, 2016.

[188] Bernard P. Binks and Tommy S. Horozov. *Colloidal Particles at Liquid Interfaces*. Cambridge University Press, 2006.

[189] Mikhail Parchine, Joe McGrath, Maria Bardosova, and Martyn E. Pemble. Large area 2d and 3d colloidal photonic crystals fabricated by a roll-to-roll langmuir-blodgett method. *Langmuir*, 32(23):5862–5869, 2016.

[190] Steven G. Johnson and J. D. Joannopoulos. *Photonic crystals: The road from theory to practice / Steven G. Johnson, John D. Joannopoulos*. Kluwer Academic Publishers, Boston, Mass. and London, 2002.

[191] Maria Bardosova, Martyn E. Pemble, Ian M. Povey, and Richard H. Tredgold. The langmuir-blodgett approach to making colloidal photonic crystals from silica spheres. *Advanced Materials*, 22(29):3104–3124, 2010.

[192] Shan Jiang, Antony van Dyk, Alvin Maurice, James Bohling, David Fasano, and Stan Brownell. Design colloidal particle morphology and self-assembly for coating applications. *Chemical Society Reviews*, 46(12):3792–3807, 2017.

[193] G. G. Roberts. An applied science perspective of langmuir-blodgett films. *Advances in Physics*, 34(4):475–512, 1985.

[194] Ivo Buttinoni, Mathias Steinacher, Hendrik Th Spanke, Juho Pokki, Severin Bahmann, Bradley Nelson, Giuseppe Foffi, and Lucio Isa. Colloidal polycrystalline monolayers under oscillatory shear. *Physical Review. E*, 95(1-1):012610, 2017.

[195] Kilian Dietrich, Giovanni Volpe, Muhammad Nasruddin Sulaiman, Damian Renggli, Ivo Buttinoni, and Lucio Isa. Active atoms and interstitials in two-dimensional colloidal crystals. *Physical Review Letters*, 120(26):268004, 2018.

[196] Adam D. Law, D. Martin A. Buzza, and Tommy S. Horozov. Two-dimensional colloidal alloys. *Physical Review Letters*, 106(12):128302, 2011.

[197] Anand Yethiraj and Alfons van Blaaderen. A colloidal model system with an interaction tunable from hard sphere to soft and dipolar. *Nature*, 421(6922):513–517, 2003.

[198] T. Honold, K. Volk, A. Rauh, J. P. S. Fitzgerald, and M. Karg. Tunable plasmonic surfaces via colloid assembly. *Journal of Materials Chemistry C*, 3(43):11449–11457, 2015.

[199] Kirsten Volk, Joseph P. S. Fitzgerald, Markus Retsch, and Matthias Karg. Time-controlled colloidal superstructures: Long-range plasmon resonance coupling in particle monolayers. *Advanced Materials*, 27(45):7332–7337, 2015.

[200] N. L. Smith, A. Coukouma, S. Dubnik, and S. A. Asher. Debye ring diffraction elucidation of 2d photonic crystal self-assembly and ordering at the air-water interface. *Physical Chemistry Chemical Physics*, 19(47):31813–31822, 2017.

[201] Xiatong Qin, Weihao Liu, Genqi Liu, Chenrui Ren, Chenhui Liu, Huanhuan Li, and Yunlei Cao. 2, 4–dichlorophenol molecularly imprinted two–dimensional photonic crystal hydrogels. *Journal of Applied Polymer Science*, 137(42):49299, 2020.

[202] Yunlei Cao, Genqi Liu, Bingqing Zheng, Xinlong Wang, Huanhuan Li, Gang Wang, Lingli Zhao, and Yue Wang. A sulfamethoxazole molecularly imprinted two-dimensional photonic crystal hydrogel sensor. *Soft Matter*, 17(19):4969–4978, 2021.

[203] Nicolas Vogel, Cristina Fernández-López, Jorge Pérez-Juste, Luis M. Liz-Marzán, Katharina Landfester, and Clemens K. Weiss. Ordered arrays of gold nanostructures from interfacially assembled Au@PNIPAM hybrid nanoparticles. *Langmuir*, 28(24):8985–8993, 2012.

[204] Laura Hoppe Alvarez, Andrey A. Rudov, Rustam A. Gumerov, Pia Lenssen, Ulrich Simon, Igor I. Potemkin, and Dominik Wöll. Controlling microgel deformation via deposition method and surface functionalization of solid supports. *Physical Chemistry Chemical Physics*, 23(8):4927–4934, 2021.

[205] Dominique Langevin. Emulsions and foams. *Emulsions, Microemulsions and Foams*, pages 195–279, 2020.

[206] Riande I. Dekker, Santiago F. Velandia, Heleen V. M. Kibbelaar, Azeza Morcy, Véronique Sadtler, Thibault Roques-Carmes, Jan Groenewold, Willem K. Kegel, Krassimir P. Velikov, and Daniel Bonn. Is there a difference between surfactant-stabilised and pickering emulsions? *Soft Matter*, 19(10):1941–1951, 2023.

[207] Cheng Zeng, Maya Winters Faaborg, Ahmed Sherif, Martin J. Falk, Rozhin Hajian, Ming Xiao, Kara Hartig, Yohai Bar-Sinai, Michael P. Brenner, and Vinothan N. Manoharan. 3d-printed machines that manipulate microscopic objects using capillary forces. *Nature*, 611(7934):68–73, 2022.

[208] Yasutaka Iwashita. Pickering–ramsden emulsions stabilized with chemically and morphologically anisotropic particles. *Current Opinion in Colloid & Interface Science*, 49:94–106, 2020.

[209] J. C. Loudet, A. M. Alsayed, J. Zhang, and A. G. Yodh. Capillary interactions between anisotropic colloidal particles. *Physical Review Letters*, 94(1):018301, 2005.

[210] Peter A. Kralchevsky and Nikolai D. Denkov. Capillary forces and structuring in layers of colloid particles. *Current Opinion in Colloid & Interface Science*, 6(4):383–401, 2001.

[211] Qi Feng, Huichang Gao, Hongji Wen, Hanhao Huang, Qingtao Li, Minhua Liang, Yang Liu, Hua Dong, and Xiaodong Cao. Engineering the cellular mechanical microenvironment to regulate stem cell chondrogenesis: Insights from a microgel model. *Acta Biomaterialia*, 113:393–406, 2020.

[212] Nicolas Thewes, Peter Loskill, Philipp Jung, Henrik Peisker, Markus Bischoff, Mathias Herrmann, and Karin Jacobs. Hydrophobic interaction governs unspecific adhesion of staphylococci: a single cell force spectroscopy study. *Beilstein Journal of Nanotechnology*, 5:1501–1512, 2014.

[213] Lillian C. Hsu, Jean Fang, Diana A. Borca-Tasciuc, Randy W. Worobo, and Carmen I. Moraru. Effect of micro- and nanoscale topography on the adhesion of bacterial cells to solid surfaces. *Applied and Environmental Microbiology*, 79(8):2703–2712, 2013.

[214] Takahisa Kawamoto, Kohei Yanagi, Yuichiro Nishizawa, Haruka Minato, and Daisuke Suzuki. The compression of deformed microgels at an air/water interface. *Chemical Communications*, 2023.

[215] Hans Riegler and Karl Spratte. Structural changes in lipid monolayers during the langmuir-blodgett transfer due to substrate/monolayer interactions. *Thin Solid Films*, 210-211:9–12, 1992.

[216] Matthias Kühnhammer, Kevin Gräff, Edwin Loran, Olaf Soltwedel, Oliver Löhmann, Henrich Frielinghaus, and Regine von Klitzing. Structure formation of pnipam microgels in foams and foam films. *Soft Matter*, 18(48):9249–9262, 2022.

[217] Xhorxhina Shaulli, Rodrigo Rivas-Barbosa, Maxime J. Bergman, Chi Zhang, Nicoletta Gnan, Frank Scheffold, and Emanuela Zaccarelli. Probing temperature responsivity of microgels and its interplay with a solid surface by super-resolution microscopy and numerical simulations. *ACS Nano*, 17(3):2067–2078, 2023.

[218] Merin Jose, Rajesh Singh, and Dillip K. Satapathy. Triple-line dynamics of a soft colloid-laden drop on a hydrophobic surface. *Soft Matter*, 19(9):1803–1812, 2023.

[219] Marcel Rey, Jannis Kolker, James A. Richards, Isha Malhotra, Thomas S. Glen, N. Y. Denise Li, Fraser H. J. Laidlaw, Damian Renggli, Jan Vermant, Andrew B. Schofield, Syuji Fujii, Hartmut Löwen, and Paul S. Clegg. Interactions between interfaces dictate stimuli-responsive emulsion behaviour. *Nature Communications*, 14(1):6723, 2023.

[220] R. Di Leonardo, F. Saglimbeni, and G. Ruocco. Very-long-range nature of capillary interactions in liquid films. *Physical Review Letters*, 100(10):106103, 2008.

[221] Karol J. Mysels and Malcolm N. Jones. Direct measurement of the variation of double-layer repulsion with distance. *Discussions of the Faraday Society*, 42:42, 1966.

[222] A. Scheludko and D. Exerowa. Über den elektrostatischen und van der waalsschen zusätzlichen druck in wässerigen schaumfilmen. *Colloid & Polymer Science*, 168(1):24–28, 1960.

[223] Katarzyna Ciunel, Marc Armélin, Gerhard H. Findenegg, and Regine von Klitzing. Evidence of surface charge at the air/water interface from thin-film studies on polyelectrolyte-coated substrates. *Langmuir*, 21(11):4790–4793, 2005.

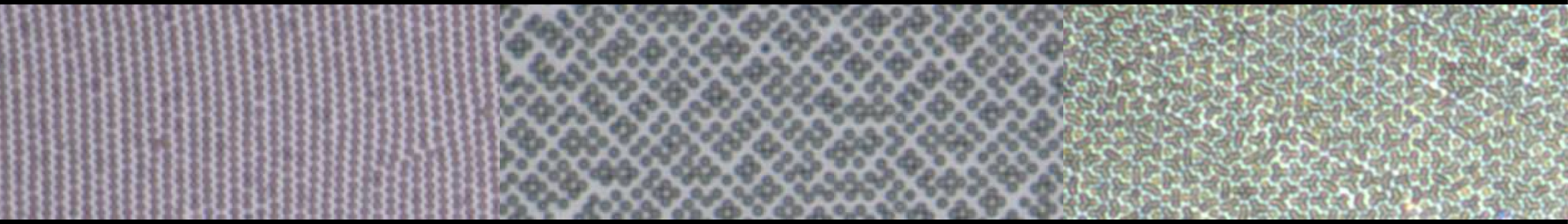

Hard Core-Soft Shell Microgels at Interfaces

Institut für Physikalische Chemie I, Heinrich-Heine-Universität Düsseldorf
Keumkyung Kuk

2023 December